Feasibility study on laser microwelding and laser shock peening using femtosecond laser pulses

by

Dongkyun Lee

A dissertation submitted in partial fulfillment
of the requirements for the degree of
Doctor of Philosophy
(Mechanical Engineering)
in The University of Michigan
2008

Doctoral Committee:

Professor Elijah Kannatey-Asibu Jr., Chair
Professor Amit Ghosh
Professor Jyotirmoy Mazumder
Professor Jwo Pan

To my parents

Acknowledgements

I express my sincere gratitude and respect to my supervisor, professor Elijah Kannatey-Asibu Jr. for his great inspiration and gentle guidance during my doctoral study in the University of Michigan, Ann Arbor.

I also express my special appreciation to professor Amit Ghosh, Jyotirmoy Mazumder and Jwo Pan for their generous suggestions on my research.

I appreciate Department of Mechanical Engineering for appointing me as a graduate student instructor. It was wonderful experience to meet undergraduate students in classes for several terms, together with professor Huei Peng, Steve Ceccio, Ann Marie Sastry, Kevin Pipe and Katsuo Kurabayashi.

I also appreciate John Nees, research scientist in CUOS, the University of Michigan, for his valuable instructions on femtosecond laser system, and professor Jinho Lee, Kwang-Min Chun, and Hyung-Hee Cho at Yonsei University, Korea, for their encouragement of starting my doctoral research.

I am indebted to my friends, seniors, juniors and research group members of professor Kannatey-Asibu for achieving this work, and I thank all of them.

Finally, my special thanks go to my parents in Korea for their full understanding and support during my doctoral study, and my brother and his wife, my sister and her husband.

Table of Contents

List of Figures

Figure

List of Tables

Table

List of Appendices

Appendix

List of Symbols

c, C = specific and volumetric bulk heat capacity, respectively. C in [J m^{-3} K^{-1}]

c_e, C_e = specific and volumetric electron heat capacity, respectively; $C_e(= \rho c_e)$ in [J m^{-3} K^{-1}]

c_l, C_l = specific and volumetric lattice heat capacity, respectively; $C_l(= \rho c_l)$ in [J m^{-3} K^{-1}]

$D(\epsilon)$ = density of state (DOS) of free electrons [eV^{-1}]

d_{ab}, d_m = the maximum depth of ablation and melting, respectively [nm]

E = coupling energy between the electrons and the lattice [J m^{-3}]

$f_e(\epsilon, T_e)$ = Fermi-Dirac distribution

G = the electron-phonon coupling factor [W m^{-3} K^{-1}]

H_m = specific latent heat [J kg^{-1}]

H_v = heat of evaporation [J kg^{-1}]

$\hbar$ = 1.05459×10^{-34} [J $\cdot$ s], Planck's constant

J = laser input fluence [J cm^{-2}]

J_{ab}, J_m = ablation and melting threshold fluence, respectively [J cm^{-2}]

k = thermal conductivity [W m^{-1} K^{-1}]

k_B = 1.3807×10^{-23} [J K^{-1}], Boltzmann's constant

k_e, k_l = electron and lattice thermal conductivity, respectively [W m^{-1} K^{-1}]

k_{eq} = thermal conductivity at equilibrium state ($T_e = T_l$) [W m^{-1} K^{-1}]

L, L_x = length scales and a domain size, respectively [nm]

l, m, n = index numbers $(0, 1, 2, 3 \dots)$ for analytical series solutions

m_e = electron mass [kg]

N = number density of electrons [m^{-3}]

P_b = boiling pressure [kPa]

q, $\vec{q}$ = heat flux [W m^{-2}]

$\mathscr{R}$ = reflectivity of the material

$\vec{r}_{BC}$ = a location vector of a domain boundary

r_f = focal radius [nm]

$\dot{S}$, $\dot{S}(\vec{r},t)$ = a heat source term [W m^{-3}]

$\mathscr{S}(\vec{\xi},\tau)$ = heat source term in dimensionless coordinates

$\mathscr{T}(\vec{\xi},\tau)$ = temperature in dimensionless coordinates

T, T_l = (lattice) temperature [K]

$T_b(P_b)$ = boiling point of a material at given pressure, P_b [K]

T_e = electron temperature [K]

T_F = Fermi temperature [K]

T_{lq} = $T_m + \Delta T_m$, liquidus [K]

T_m = melting point [K]

ΔT_m = solidification temperature [K]

T_{norm} = normalization temperature for analytical solutions [K]

T_{so} = $T_m - \Delta T_m$, solidus [K]

T_{top} = temperature at the top surface of a material [K]

T_∞, T_0 = ambient and initial temperature, respectively (constant) [K]

t_p = pulse duration in FWHM [ps]

u, U = specific and volumetric internal energy, respectively; $U(=\rho u)$ in [J m^{-3}]

$u(t)$ = unit step function

V_s = speed of sound [m s^{-1}]

x = coordinate in depth direction in 1D [nm]

α_s = coefficient for the subsurface boiling ablation model

γ_e = c_e/c, dimensionless electron heat capacity

γ_l = c_l/c, dimensionless lattice heat capacity

$\delta(t)$ = Dirac delta function

δ_s = skin depth [nm]

ϵ_F $= k_B \cdot T_F$, Fermi energy [eV]

ε $= k/(GL^2)$, dimensionless electron-phonon coupling factor

θ_m $= d_m - d_{ab}$, the maximum molten pool thickness [nm]

ϑ $= (\mathscr{T}(\vec{\xi}, \tau) - T_\infty)/(T_{norm} - T_\infty)$,normalized dimensionless temperature

κ $= k/\rho c$, thermal diffusivity [m^2 s^{-1}]

λ = wavelength [nm]

λ_e = electron-phonon coupling constant (dimensionless)

$\Xi_{x,y,z}$ $= L_{x,y,z}/L$, dimensionless length scale

$\vec{\xi}$ $= \vec{r}/L$, dimensionless location vector

ρ = mass density [kg m^{-3}]

ς $= \mathscr{S}(\vec{\xi}, \tau)/(k \cdot (T_{norm} - T_\infty)/L^2)$, dimensionless heat source

τ $= t \cdot (k/\rho c)/L^2$, dimensionless time

τ_e = electron relaxation time [ps]

Ω_e^n, Ω_l^m = n-th element in electron domain, and m-th element in lattice domain

$\langle \omega^2 \rangle$ = second moment of the phonon spectrum [meV^2]

Abstract

Ultrafast lasers of sub-picosecond pulse duration have thus far been investigated for ablation, drilling and cutting processes. Ultrafast lasers also have the potential for laser welding of small components of the order of microns, and for laser shock peening to enhance the peening depth.

First, the two-temperature model is implemented in a general-purpose commercial FEM package, ABAQUS, to enable broad based application of the two-temperature model in practical engineering problems. The implementation is validated by comparison with linear solutions obtained using separation of variables. It is then used to investigate the potential for microwelding using an ultrafast laser pulse.

Next, the two-temperature model is analyzed using ABAQUS to study the feasibility of laser microwelding with ultrafast lasers. A material model is constructed using material properties and the subsurface boiling model for ablation. Laser processing parameters of repetition rate, pulse duration, and focal radius are then investigated, in terms of molten pool generated in the material, and requirements for those parameters are discussed to obtain feasible parameter ranges for laser microwelding using ultrafast lasers.

Then, the feasibility of laser shock peening using ultrafast laser pulses was experimentally investigated. A zinc coating was used for the thermo-protective effect, and a water confining layer was considered in the investigation. A high numerical aperture focusing lens was used to avoid optical breakdown of the water layer. Laser fluence and feed rate were selected as experimental parameters. Microhardness measurements were made on the top surface of the shock peened specimen and compared with the original material hardness. Improvement in microhardness obtained after laser shock peening with ultrafast laser pulses was slight, compared to results in the

literature.

Finally, conditions to achieve feasible laser microwelding and laser shock peening using femtosecond laser pulses are discussed from the numerical and experimental observations.

Chapter I

Introduction

Lasers have been used as a tool for precise materials processing in micro and nano manufacturing operations due to its non-contact nature and the high intensity resulting from the ability to focus it to a small diameter. Developments in laser technology have enabled smaller wavelengths, shorter pulse durations, and higher powers to be achieved, and made it possible for engineers and scientists to perform an almost unlimited variety of new functions or tasks using lasers (Siegman, 1986).

They have proven to have superior ability in fusion welding of various metals (Fabbro et al., 2005; Cao et al., 2006; Richter et al., 2007); dissimilar metals (Triantafyllidis et al., 2003; Mys and Schmidt, 2006; Sierra et al., 2007); even dissimilar non-metallic materials, for example, glass and silicon (Wild et al., 2001). CO_2 or Nd:YAG lasers in continuous wave (CW) mode or with pulse duration of the order of milliseconds are dominant in the laser welding industry (Kalpakjian and Schmid, 2001). Lasers are considered to be the best choice among a variety of micro-scale material joining methods (Brockmann et al., 2002). Laser welding of thin foils of micrometer thickness has been successfully performed (Du et al., 2002; Abe et al., 2003; Park et al., 2003; Isamu et al., 2004). However, for very small components with overall dimensions of the order of microns, CW or pulsed lasers currently used for welding may affect the entire part, and that may not be acceptable. Semak et al. (2003) indicated that pulse durations shorter than 1 ms may enable microwelding of fusion zones of the order of or smaller than 100 μm. Duley (2004) mentions the possibility of extending laser welding technology to nanoscale structures, based on the notion that it is the geometry of the part itself, and not the wavelength, that

determines processing efficiency.

Laser shock peening (LSP) has been extensively investigated since the works of Gregg and Thomas (1966) and Anderholm (1970) were reported. It has been investigated for various materials, including steel (Peyre et al., 2000; Yilbas et al., 2003; Yakimets et al., 2004; Aldajah et al., 2005; Farrahi and Ghadbeigi, 2006), aluminum (Fairand et al., 1972; Peyre et al., 1996; Hong and Chengye, 1998; Rubio-González et al., 2004; Tan et al., 2004) and nickel alloy, molybdenum and copper (Forget et al., 1990; Hammersley et al., 2000; Kaspar et al., 2000; Zhang et al., 2004). It has also been successfully applied to improve fatigue life of automotive ring and pinion gears and aircraft engine turbine blades (See et al., 2002). Laser shock peening is known to be superior to conventional shot peening for such surface treatment since it results in deeper compressive residual stresses and smoother processed surface, together with the capability of localized processing (Montross et al., 2002). Despite significant improvements over the years, Fabbro et al. (1998) indicated the potential to improve the process by adopting extremely short laser pulses to achieve higher pressure, and thus deeper processed layers. This can be inferred from an experimental demonstration on acoustic signal generation using short laser pulse durations between 100 fs and 150 ps (Dehoux et al., 2006).

Ultrafast lasers (UFL) of sub-picosecond pulse duration have the potential for overcoming current limitations of laser welding and shock peening. During laser-matter interaction for an extremely short pulse energy input to a metal, equilibrium may not be established between the electrons and lattice because the time required to establish equilibrium in the electron gas is much less than the time for achieving equilibrium between the electrons and the lattice (Kaganov et al., 1957). Unfortunately, conventional thermal diffusion models are not adequate for such non-equilibrium conditions. Even though there have been several models to describe such thermal behavior of a material (Tzou, 1997), the two-temperature model (TTM) proposed by Anisimov et al. (1974) has been widely adopted to understand the laser-matter interaction of ultrashort laser pulses for metals. It describes the interaction in terms of electron and lattice temperatures, and an electron-phonon coupling factor. The TTM has been

used for investigations on laser-mater interaction in the sub-picosecond pulse regime (Elsayedali et al., 1987; Sherman et al., 1989; Fann et al., 1992; Wellershoff et al., 1999; Schmidt et al., 2002).

Ultrafast laser technology, for example chirped pulse amplification (Strickland and Mourou, 1985) has been used to investigate processing applications such as material ablation, drilling and cutting (Preuss et al., 1995; Momma et al., 1997; Banks et al., 2000; Griffith et al., 2003). Liu et al. (1997) provided extensive discussion on chirped pulse amplification (CPA) laser generation technology and its application to laser material processing. The uniqueness of UFL for material removal over longer pulse durations has been demonstrated experimentally (Pronko et al., 1995; Chichkov et al., 1996; Zhu et al., 1999). In recent years, successful microwelding of glasses with measurable joint strength has been achieved using UFL (Tamaki et al., 2006).

Numerical analysis of laser materials processing has been extensively undertaken. The finite element method (FEM), including general-purpose commercial FEM packages such as ABAQUS, is frequently employed for numerical analysis of LSP (Braisted and Brockman, 1999; Peyre et al., 2003); of welding (Deshayes et al., 2003; Borrisutthekul et al., 2005; Lin et al., 2005); and of laser bending (Zhang and Xu, 2003). However, special purpose codes are usually constructed for numerical analysis involving the TTM (Qiu and Tien, 1993; Hüttner and Rohr, 1996; Chen and Beraun, 2001; Schmidt et al., 2002).

The goal of this study is to investigate the feasibility of laser microwelding and laser shock peening using UFL, and the outcomes are described in Chapter 2, 3 and 4.

Chapter 2 covers the TTM implementation in a general-purpose commercial FEM package, ABAQUS, to enable broad based application of the TTM in practical engineering problems. This chapter has been accepted for publication in the ASME Journal of Manufacturing Science and Engineering.

Chapter 3 deals with a feasibility study of laser microwelding of metals using UFL. Select laser parameters of pulse repetition rate, pulse duration and focal radius, are examined numerically with the TTM implementation of Chapter 2, and requirements

on those laser parameters for feasible microwelding of metals with UFL are proposed. This chapter has been accepted for publication in the ASME Journal of Manufacturing Science and Engineering.

Chapter 4 describes experimental investigation on the feasibility of laser shock peening of top coated steel in water confined configuration using ultrafast laser pulses. This chapter is under preparation for submission to the 27th International Congress on Applications of Lasers & Electro-Optics (ICALEO) and the Journal of Laser Application.

In Chapter 5, conclusions on the feasibility of laser microwelding and laser shock peening using UFL are drawn from the numerical and experimental studies.

Chapter II

Implementation of the two temperature model in ABAQUS

2.1 Introduction

As a result of their ability to produce high-energy concentrations and be focused to very small size, lasers have demonstrated their capability as a tool of choice in micro and nano manufacturing operations. Developments in laser technology have enabled smaller wavelengths, shorter pulse durations, and higher powers and frequencies to be achieved, and make it possible for engineers and scientists to perform an almost unlimited variety of new functions or tasks using lasers (Siegman, 1986). Lasers have been successfully applied in microfabrication, for example recrystallization, drilling, trimming, cleaning, welding and surface modification. The most successful of these applications are microhole drilling, trimming, and recrystallization (Dickinson, 2002).

Thin metal sheets of few tens of microns have been successfully welded using lasers from CW to milliseconds pulses (Du et al., 2002; Park et al., 2003). Moreover, Semak et al. (2003) suggest that short pulses should be used to perform microwelding at small beam diameters of few tens of micrometers. Duley (2004) mentions the possibility of extending laser welding technology to nanoscale structures, based on the notion that it is the geometry of the part itself, and not the wavelength, that determines processing efficiency. However, for very small components with overall dimensions of the order of microns, CW or pulsed lasers currently used for welding may affect the entire part, and that may not be acceptable.

Laser shock peening (LSP) has also been extensively investigated since the works of Gregg and Thomas (1966) and Anderholm (1970) were reported, as summarized by Fabbro et al. (1998) and Montross et al. (2002). Fabbro et al. (1998) indicated that

shorter laser pulses can produce higher pressures, resulting in greater shock peening depth.

Ultrafast lasers (UFL) of sub-picosecond pulse duration have the potential for overcoming such current limitations of laser welding and shock peening. In laser-matter interaction for an extremely short pulse energy input to a metal, equilibrium may not be established between the electrons and lattice because the time required to establish equilibrium in the electron gas is much less than the time for achieving equilibrium between the electrons and the lattice (Kaganov et al., 1957). Unfortunately, conventional thermal diffusion models are not adequate for such non-equilibrium conditions. Thus, Anisimov et al. (1974) proposed the two-temperature model (TTM) to account for this phenomenon.

Ultrafast laser technology, for example chirped pulse amplification (Strickland and Mourou, 1985) has been used to investigate processing applications such as material ablation, drilling and cutting (Preuss et al., 1995; Momma et al., 1997; Banks et al., 2000; Griffith et al., 2003). Liu et al. (1997) provided extensive discussion on CPA laser generation technology and its application to laser material processing. The TTM has also been used for investigations on laser-mater interaction in the sub-picosecond pulse regime (Elsayedali et al., 1987; Sherman et al., 1989; Fann et al., 1992; Wellershoff et al., 1999; Schmidt et al., 2002).

Numerical analyses on laser materials processing have also been extensively undertaken. The finite element method (FEM), including general-purpose commercial FEM packages such as ABAQUS, is frequently employed for numerical analysis of LSP (Braisted and Brockman, 1999; Peyre et al., 2003); of welding (Deshayes et al., 2003; Borrisutthekul et al., 2005; Lin et al., 2005); and of laser bending (Zhang and Xu, 2003). For numerical analysis involving the TTM, special purpose codes have usually been constructed (Schmidt et al., 2002; Qiu and Tien, 1993; Hüttner and Rohr, 1996; Chen and Beraun, 2001).

The goal of this study is to implement the TTM in a general-purpose commercial FEM package, ABAQUS, to enable broad based application of the TTM in practical engineering problems.

2.2 Background

Anisimov et al. (1974) proposed the two-temperature model (TTM) as follows:

$$C_e \frac{\partial T_e}{\partial t} = -\vec{\nabla} \bullet \vec{q_e} - \dot{E}(T_e, T_l) + \dot{S}(\vec{s}, t) \tag{2.1a}$$

$$C_l \frac{\partial T_l}{\partial t} = \dot{E}(T_e, T_l) \tag{2.1b}$$

where $\dot{E}(T_e, T_l)$ is given by the following equation, when T_e and T_l are much higher than the Debye temperature:

$$\dot{E}(T_e, T_l) = \frac{\pi^2 m_e N V_s^2}{6} \cdot (T_e - T_l) \equiv G \cdot (T_e - T_l) \tag{2.2}$$

In this model, C_e and C_l are temperature dependent, and Fouriers law is used as a heat flux model. It is evident from Eq. (3.2) that G is neither a function of electron nor lattice temperature. Qiu and Tien (1993) incorporated a different heat flux model based on the Boltzmann transport equation as follows:

$$\tau_e \frac{\partial q_e}{\partial t} + q_e = -k_e \frac{\partial T_e}{\partial x} \tag{2.3}$$

where τ_e is a constant, and the electron thermal conductivity is considered as a function of the electron and lattice temperatures as follows:

$$k_e = k_{eq} \cdot \frac{T_e}{T_l} \tag{2.4}$$

Anisimov and Rethfeld (1997) further modified the TTM with an additional lattice thermal conduction term and an electron thermal conductivity that was described as follows:

$$k_e = \chi \cdot \frac{(\phi_e^2 + 0.16)^{5/4} \cdot (\phi_e^2 + 0.44) \cdot \phi_e}{(\phi_e^2 + 0.092)^{1/2} \cdot (\phi_e^2 + \eta \cdot \phi_l)} \tag{2.5}$$

where $\phi_e = k_B T_e / \epsilon_F$ and $\phi_l = k_B T_l / \epsilon_F$ for the Fermi energy ϵ_F $(= k_B \cdot T_F)$. χ and η are material constants, with χ= 353 $W/K \cdot m$ and $\eta = 0.16$ for gold. Schmidt et al. (2002) considered several thermal conductivity models for the TTM with ballistic electrons and they compared their results with experimental data. Chen et al. (2005) subsequently introduced a T_e and T_l dependent and τ_e for the heat flux model of

Eq. (3.3) as follows:

$$\dot{E} = \left\{ G_{RT} \left[\frac{A_e}{B_l}(T_e + T_l) + 1 \right] \right\} \cdot (T_e - T_l) \tag{2.6}$$

$$\tau_e = \frac{1}{A_e \cdot T_e^2 + B_l \cdot T_l} \tag{2.7}$$

where G_{RT}, A_e and B_l are material constants. A_e and B_l are known as 1.2×10^7 $K^{-2}s^{-1}$ and 1.23×10^{11} $K^{-1}s^{-1}$, respectively, for gold (Chen et al., 2005).

In this study, a general-purpose commercial FEM package, ABAQUS, is used to simulate the TTM. Specific issues required for ABAQUS, including user subroutines, are investigated. The analysis is validated by comparison with linear TTM solutions. For this, the linear TTM is solved analytically using separation of variables, and series form solutions are obtained. The TTM implementation is used for numerical analysis of low and high fluence laser input, and the results are examined. Finally, the TTM implementation is used to investigate the potential for microwelding using UFL.

2.3 Analysis

2.3.1 The TTM implementation in ABAQUS

Currently, it is clear that there is no direct support for the TTM in ABAQUS. However, ABAQUS incorporates the conventional heat conduction model which can be customized via user subroutines, which is described in terms of the specific internal energy as follows:

$$\rho \frac{\partial u}{\partial t} = -\vec{\nabla} \bullet \vec{q} + \dot{S} \tag{2.8}$$

For solid and liquid, the specific heat capacity, c, can be related to the specific internal energy, u, and temperature as (Sonntag et al., 2003):

$$c = \frac{\partial u}{\partial T} \tag{2.9}$$

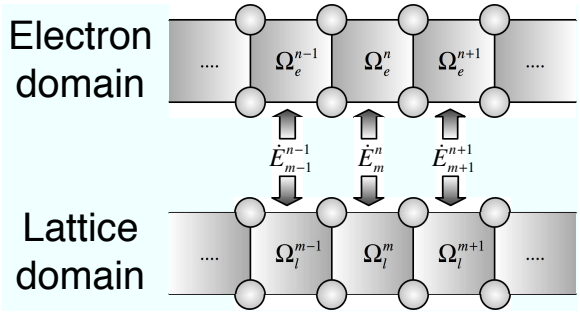

Fig. 2.1. The concept of dual domain configuration for the TTM in ABAQUS

By applying Eq. (2.9) to Eqs. (3.1a) and (3.1b) with relations of $C_e = \rho c_e$ and $C_l = \rho c_l$, the TTM can be rewritten as:

$$\rho \frac{\partial u_e}{\partial t} = -\vec{\nabla} \bullet \vec{q_e} - \dot{E} + \dot{S} \tag{2.10a}$$

$$\rho \frac{\partial u_l}{\partial t} = \dot{E} \tag{2.10b}$$

There is an obvious similarity when Eqs. (2.10a) and (2.10b) are compared with Eq. (2.8); Equation (2.8) is generally solved within a set of elements, or a domain with boundary and initial conditions. Thus, the TTM can be modeled for ABAQUS, if two geometrically independent domains can be established, which are correlated with each other in terms of thermal behavior of a material, especially for $\dot{E}$, as illustrated in Fig. 2.1, and can be named as a dual domain configuration. The required correlations can be modeled using user subroutines provided by ABAQUS.

ABAQUS provides a user subroutine UMATHT for modeling customized thermal behavior of materials (ABAQUS Inc., 2006). In the subroutine, there are six thermal behavior related variables that should be updated for the next time step $t+\Delta t$, based on the values provided for the current time t. Three of them are closely related to the internal energy and the other three to heat flux.

First, the three internal energy-related terms, u, $\partial u/\partial T$ and $\partial u/\partial(\vec{\nabla}T)$, are discussed. For the internal energy, u, the heat source term and the electron-phonon coupling term of the TTM should be considered at the same time when the u term is updated for the next time step $t + \delta t$. With the assumption that the density, ρ, is not time dependent, Eqs. (2.10a) and (2.10b) can be rearranged in terms of the

volumetric internal energy, U, as follows:

$$\dot{U}_e + \dot{E} - \dot{S} = -\vec{\nabla} \bullet \vec{q}_e \tag{2.11a}$$

$$\dot{U}_l - \dot{E} = 0 \tag{2.11b}$$

where the upper dots represent partial differentiation with respect to time. From the left side of Eqs. (2.11a) and (2.11b), effective energy terms for the electron and lattice system, $U_{e,eff}$ and $U_{l,eff}$, can be defined as $U_{e,eff} \equiv U_e + E - S$ and $U_{l,eff} \equiv U_l - E$. Then, the effective internal energy terms to be updated for the next time $t + \Delta t$, $U_{e,eff}^{t+\Delta t}$ and $U_{e,eff}^{t+\Delta t}$, can be written in terms of the current values, $U_{e,eff}^{t}$ and $U_{l,eff}^{t}$, as $U_{e,eff}^{t+\Delta t} = U_{e,eff}^{t} + dU_{e,eff}$ and $U_{l,eff}^{t+\Delta t} = U_{l,eff}^{t} + dU_{l,eff}$. The $dU_{e,eff}$ and $dU_{l,eff}$ terms can be evaluated mathematically (see Appendix A), which results in the following:

$$U_{e,eff}^{t+\Delta t} = U_{e,eff}^{t} + \left[\left(\frac{\partial U_e}{\partial T_e} \right) \cdot \Delta T_e + (\dot{E} - \dot{S}) \cdot \Delta t \right] \tag{2.12a}$$

$$U_{l,eff}^{t+\Delta t} = U_{l,eff}^{t} + \left[\left(\frac{\partial U_l}{\partial T_l} \right) \cdot \Delta T_l - \dot{E} \cdot \Delta t \right] \tag{2.12b}$$

With the exception of the partial derivative terms, the values of $\dot{E}$, $\dot{S}$, $U_{e,eff}^{t}$ and $U_{l,eff}^{t}$ are all known to the user subroutine. In addition, the equations are written in discretized form by replacing d with Δ to indicate that those terms are evaluated from the finite differences between time t and $t + \Delta t$. The term $\partial U / \partial T$ can be easily found from Eq. (2.9) and the relation $U = \rho u$ as follows:

$$\frac{\partial U_e}{\partial T_e} = u_e \cdot \frac{\partial \rho}{\partial T_e} + C_e \tag{2.13a}$$

$$\frac{\partial U_l}{\partial T_l} = u_l \cdot \frac{\partial \rho}{\partial T_l} + C_e \tag{2.13b}$$

At this point, the density, ρ, is assumed as a constant with respect to T_e and T_l for simplicity. Then the $\partial \rho / \partial T_e$ and $\partial \rho / \partial T_l$ terms vanish from the equations. At the same time, Eqs. (2.13a) and (2.13b) can be substituted into Eqs. (2.12a) and (2.12b) to complete their evaluation. In addition, it is assumed that $U_{e,eff}$ and $U_{l,eff}$ are independent of the temperature gradients. Hence, for both electron and lattice

internal energy terms, we have

$$\frac{\partial U_e}{\partial \vec{\nabla} T_e} = \vec{0} \tag{2.14a}$$

$$\frac{\partial U_l}{\partial \vec{\nabla} T_l} = \vec{0} \tag{2.14b}$$

It must be noted that C_e, C_l, $\dot{E}$ and $\dot{S}$ in Eqs. (2.12) and (2.13) can be either constant or functions of variables, including time, location and temperature.

The heat flux related terms, $\vec{q}$, $\partial \vec{q}/\partial T$ and $\partial \vec{q}/\partial(\vec{\nabla} T)$, can be obtained from the heat flux model, for example, Fouriers law or Eq. (3.3). Equation (3.3) is considered in the following discussion, with a temperature dependent τ_e, Eq. (3.6). If the first term on the left side of Eq. 3.3 is discretized over a finite time step Δt, and the second term is replaced with a value at the next time step $t+\Delta t$, the equation can be written as follows:

$$\tau_e \frac{q_{e,x}^{t+\Delta t} - q_{e,x}^{t}}{\Delta t} + q_{e,x}^{t+\Delta t} = -k_e \cdot \frac{\partial T_e}{\partial x}$$

The temperature gradient term is not discretized because ABAQUS provides the information to the user subroutine. Then, rearrangement of the equation gives

$$q_{e,x}^{t+\Delta t} = \frac{1}{\tau_e + \Delta t} \cdot \left(\tau_e \cdot q_{e,x}^{t} - \Delta t \cdot k_e \cdot \frac{\partial T_e}{\partial x} \right) \tag{2.15}$$

It should be noted that all the terms on the right side of the equation are known to the user subroutine, either provided by ABAQUS or the user. The $\partial \vec{q}/\partial T$ and $\partial \vec{q}/\partial(\vec{\nabla} T)$ terms can also be obtained in a manner similar to Eq. (2.15) (see Appendix B), and the results are:

$$\left(\frac{\partial q}{\partial T} \right)_{e,x}^{t+\Delta t} = \frac{1}{\tau_e + \Delta t} \cdot \left[\tau_e \cdot \left(\frac{\partial q}{\partial T} \right)_{e,x}^{t} + \frac{\partial \tau_e}{\partial T_e} \cdot \frac{\Delta t}{\tau_e + \Delta t} \cdot \left(k_e \frac{\partial T_e}{\partial x} + q_{e,x}^{t} \right) - \Delta t \cdot \frac{\partial k_e}{\partial T_e} \cdot \frac{\partial T_e}{\partial x} \right] \tag{2.16}$$

$$\left(\frac{\partial q}{\partial (\nabla T)} \right)_{e,x}^{t+\Delta t} = \frac{1}{\tau_e + \Delta t} \cdot \left[\tau_e \cdot \left(\frac{\partial q}{\partial (\nabla T)} \right)_{e,x}^{t} - \Delta t \cdot k_e \right] \tag{2.17}$$

Equations (2.15), (2.16) and (2.17) can be modified for Fouriers law, $\vec{q} = -k \cdot \vec{\nabla} T$, by setting τ_e in those equations as zero, as can be seen from Eq. (3.3). In addition,

the derivative terms in Eq. (2.16) can be evaluated explicitly from Eq. (2.4) or (2.5) for $\partial k_e/\partial T_e$, and (3.6) for $\partial \tau_e/\partial T_e$.

2.3.2 Temperature dependent terms & material ablation in ABAQUS

Equations (2.12) to (2.17) should be coded in a user subroutine UMATHT. It is known that the subroutine is called at integration points of an element. That presents a technical problem in implementing the TTM in ABAQUS: it is very limited in its ability to obtain information, for example temperature, of other elements when the subroutine is called. As shown in Fig. 2.1, the TTM should be modeled as a dual domain system in ABAQUS, i.e. one domain representing the electron system and the other the lattice system. Information of each domain is necessary to calculate terms that have a relation with both the electron and lattice temperatures, for example $\dot{E}$ of Eqs. (3.2) or (2.6). Therefore, an inter-element information sharing method needs to be constructed, either within the subroutine UMATHT or another subroutine that can refer information of the element that calls the subroutine, and that can also pass information easily to the subroutine UMATHT. In this study, another user subroutine USDFLD is used for this purpose, and for succinctness of UMATHT.

The user subroutine USDFLD can make a request for temperature information to ABAQUS when the subroutine is called at the integration points of an element (ABAQUS Inc., 2006). That means one of two temperatures is known by default in the subroutine. For the other temperature, an external common memory block can be reserved for inter-element referencing. The known temperature is stored in the memory block, and retrieved by the other element when necessary, as illustrated in Fig. 2.2 (a). Since the electron thermal conductivity, k_e in Eq. (2.4) or (2.5) is closely related to both temperatures, it needs to be coded in the subroutine USDFLD. Likewise, the heat capacity terms, C_e and C_l. It should be noted that the subroutine USDFLD is called at an element before the subroutine UMATHT is called. Hence, the calculated results of $\dot{E}$, k_e, C_e and C_l in USDFLD can be passed onto the user subroutine UMATHT. ABAQUS recommends using the temperature dependent heat capacities to model the latent heat of phase change, in terms of an effective heat

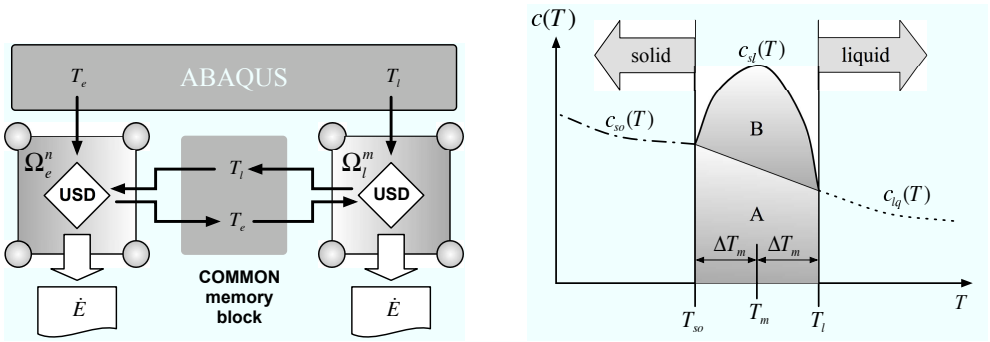

Fig. 2.2. (a) Temperature information sharing via common memory block in the user subroutine, USDFLD, shown as USD in the figure: The ◊ marks indicate that the subroutine is called at the integration points of 4-node planar elements, Ω_e^n and Ω_l^m (b) Effective heat capacity with the latent heat (Area B) for phase change in USDFLD

capacity, c_{sl}, Fig. 2.2 (b). For a pure material, imaginary solidus and liquidus are required. In the figure, the latent heat H_m corresponds to the shaded area B. If c_{sl} is assumed to be constant for $T_{so} < T < T_{lq}$, it can be simplified as follows (ABAQUS Inc., 2006):

$$c_{sl} = \frac{H_m}{2 \cdot \Delta T_m} + \frac{c_{so}(T_{so}) + c_{lq}(T_{lq})}{2}, \quad T_{so} < T < T_{lq} \tag{2.18}$$

where ΔT_m is the temperature difference between the melting point and either the solidus or liquidus, and is half the solidification temperature range in this study. The latent heat is considered only for the lattice heat capacity term.

For modeling material ablation, ABAQUS provides an Arbitrary Lagrangian-Eulerian (ALE) analysis, which allows node motions and element deformations customized with a user subroutine UMESHMOTION (ABAQUS Inc., 2006). In this study, customization is necessary to relate temperature with material ablation, and a 4-node planar element is considered, as shown in Fig. 2.3. Ablation is assumed to occur when a portion of a domain exceeds a designated temperature, T_{crit}. It is also assumed that the energy input is in the ξ direction, Fig. 2.3 (b). Then the analysis involves evaluating the location of ablation within the element, if the element nodal temperatures satisfy the condition $T^{N1} > T_{crit}$ and $T^{N2} < T_{crit}$. T^{N1} and T^{N2} are nodal temperatures at nodes $N1$ and $N2$ respectively, Fig. 2.3 (b). It should also be noted that the time step should be small enough to avoid the situation where

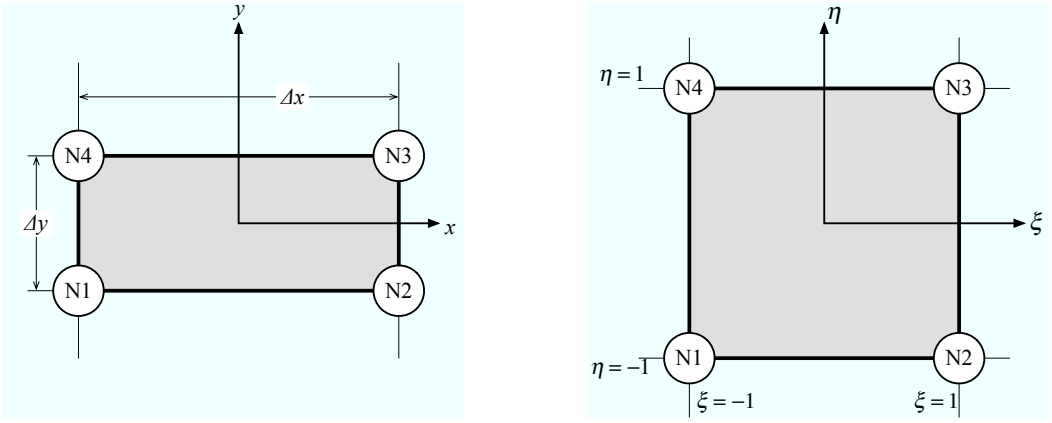

(a) (b)

Fig. 2.3. 4-node linear planar finite element: (a) actual coordinates, and (b) normalized coordinates

$T^{N1} > T_{crit}$ and $T^{N2} > T_{crit}$. It is known that a temperature inside a finite element can be expressed in terms of nodal temperatures with shape functions of the element. Thus, the location at $T_l = T_{crit}$ on the $\eta = -1$ edge of the element, ξ_{crit}, can be obtained as:

$$\xi_{crit} = \frac{T_l^{N1} + T_l^{N2} - 2T_{crit}}{T_l^{N1} - T_l^{N2}} \tag{2.19}$$

Once ξ_{crit} is found, the value is converted into the actual coordinate system shown in Fig. 2.3 (a). It should be noted that Eq. (2.19) can be written for the $\eta = 1$ edge by replacing $N1$ and $N2$ with $N4$ and $N3$, and that evaluations for both $\eta = 1$ and $\eta = -1$ edges are identical if a heat source is given in 1D since $T_l^{N1} = T_l^{N4}$ and $T_l^{N2} = T_l^{N3}$ in such cases.

2.3.3 Analytical solutions for the linear TTM

Having constructed the TTM implementation in ABAQUS, its validation is essential since the TTM is not a default model supported by ABAQUS. As usual, an analytical solution is a good reference for validating a numerical analysis code or commercial package. To obtain analytical solutions, the TTM of Eqs. (3.1a) and (3.1b) should be linearized, with the assumption of constant material properties, especially C_e, C_l, k, and G. Then, analytical solutions can be obtained using separation of variables.

With the linearization assumption, if the electron temperature is eliminated from Eqs. (3.1a) and (3.1b) and dimensionless parameters are defined, in a manner similar to the works of Hays-Stang and Haji-Sheikh (1994), and Smith et al. (1999), the TTM can be reduced to a single equation in dimensionless form as follows:

$$\varepsilon\gamma_l \cdot \frac{\partial}{\partial\tau}\left(\gamma_e \cdot \frac{\partial\vartheta}{\partial\tau} - \nabla^2_{\vec{\xi}}\vartheta\right) + \left(\frac{\partial\vartheta}{\partial\tau} - \nabla^2_{\vec{\xi}}\vartheta\right) = \varsigma \tag{2.20}$$

with corresponding boundary (BC) and initial (IC) conditions:

$$\text{BC: } \vartheta(\vec{\xi}_{BC},\tau) = 0 \qquad \text{IC: } \vartheta(\vec{\xi},0) = 0, \quad \dot{\vartheta}(\vec{\xi},0) = 0$$

It is clear that Eq. (2.20) with its BC and ICs can be solved using separation of variables. A temperature solution and a heat source can be written in infinite series form, considering separation of variables as follows:

$$\vartheta(\vec{\xi},\tau) = \sum_{l=0}^{\infty}\sum_{m=0}^{\infty}\sum_{n=0}^{\infty}(A_{lmn}\cdot\vartheta_{\vec{\xi},lmn}\cdot\vartheta_{\tau,lmn}) \tag{2.21}$$

$$\varsigma = \varsigma_\tau \cdot \varsigma_{\vec{\xi}} = \varsigma_\tau \cdot \sum_{l=0}^{\infty}\sum_{m=0}^{\infty}\sum_{n=0}^{\infty}\varsigma_{\vec{\xi},lmn} \tag{2.22}$$

where A_{lmn} is an unknown coefficient. Eq. (2.20) can then be separated into temporal and spatial terms of the dimensionless temperature, ϑ_τ and $\vartheta_{\vec{\xi}}$ respectively, as follows:

$$\nabla^2_{\vec{\xi}}\vartheta_{\vec{\xi},lmn} + \kappa^2_{lmn}\cdot\vartheta_{\vec{\xi},lmn} = 0 \tag{2.23}$$

$$\ddot{\vartheta}_{\tau,lmn} + 2\zeta_{lmn}\cdot\dot{\vartheta}_{\tau,lmn} + \omega^2_{lmn}\cdot\vartheta_{\tau,lmn} = \frac{\varsigma_c w_{lmn}}{A_{lmn}}\cdot\varsigma_\tau \tag{2.24}$$

where $\omega^2_{lmn} \equiv \varsigma_{\vec{\xi},lmn}/\vartheta_{\vec{\xi},lmn}$, $\zeta_{lmn} \equiv 1/2\cdot(1/(\varepsilon\gamma_l\gamma_e) + \kappa^2_{lmn}/\gamma_e)$, $\varsigma_c \equiv 1/(\varepsilon\gamma_l\gamma_e)$ and $w_{lmn} \equiv \varsigma_{\vec{\xi},lmn}/\vartheta_{\vec{\xi},lmn}$. It must be emphasized that w_{lmn} and κ^2_{lmn} should be constants because Eqs. (2.23) and (2.24) are ordinary differential equations which are only functions of location and time, respectively. However, w_{lmn} and κ^2_{lmn} are strongly related to the spatial parts of the variable-separated temperature and heat source, which implies that there will be a restriction for the heat source term, which is usually given.

The solution of Eq. (2.23) for Cartesian coordinates is obtained, using separation

of variables and BCs as follows:

$$\begin{aligned}\vartheta_{\vec{\xi},lmn} &= \Theta_{lmn}\cdot\cos\left(\frac{(2l+\pi)}{2\Xi_x}\cdot\xi_x\right)\cdot\cos\left(\frac{(2m+\pi)}{2\Xi_y}\cdot\xi_y\right)\cdot\cos\left(\frac{(2n+\pi)}{2\Xi_z}\cdot\xi_z\right)\\ &\equiv \Theta_{lmn}\cdot c^3_{lmn}(\vec{\xi})\end{aligned}$$

where $\kappa^2_{lmn}=\pi^2[(\frac{2l+1}{\Xi_x})^2+(\frac{2m+1}{\Xi_y})^2+(\frac{2n+1}{\Xi_z})^2]/4$, and Θ_{lmn} is an unknown coefficient that is related to other variables. Noting that w_{lmn} should be a constant, it can be concluded that the spatial part of the source term could also be expanded in terms of cosines, i.e. Fourier cosine series, as follows:

$$\varsigma_{\vec{\xi},lmn}=S_{lmn}\cdot c^3_{lmn}(\vec{\xi})$$

where S_{lmn} is a Fourier cosine series coefficient, which is known for a given heat source. At the same time, the nature of the equation implies that the spatial heat source term $\varsigma_{\vec{\xi}}$ of Eq. (2.22) should be an even function in spatial coordinates. The restriction can be handled if an imaginary mirror-imaged domain is introduced to make any arbitrary heat source an even function. Then, the solution of Eq. (2.23) can be obtained as follows:

$$\vartheta_{\vec{\xi},lmn}=\frac{S_{lmn}}{w_{lmn}}\cdot c^3_{lmn}(\vec{\xi}) \tag{2.25}$$

The solution of Eq. (2.24) can be obtained in two forms, depending on whether or not the temporal portion of the heat source of interest, ς_τ in Eq. (2.22), is simple enough for the inverse Laplace transform to be obtained. If the temporal heat source term is in such a form, the solution can be found as follows:

$$\vartheta_{\tau,lmn}=\varsigma_c\cdot\frac{w_{lmn}}{A_{lmn}}\cdot\mathscr{L}^{-1}\left[\frac{\bar{\varsigma_\tau}}{s^2+2\cdot\zeta_{lmn}\cdot s+w^2_{lmn}}\right] \tag{2.26}$$

where $\bar{\varsigma_\tau}$ is the Laplace transform of ς_τ. If the temporal heat source term is not of simple form, it can be defined using convolution integral form as follows:

$$\varsigma_\tau\equiv\int_0^\tau\varsigma_\tau(\tau^\circ)\cdot\delta(\tau-\tau^\circ)\cdot d\tau^\circ$$

In this case, the solution $\vartheta_{\tau,lmn}$ for the heat source requires an impulse response of

temperature, g_{lmn}, which can be obtained from Eq. (2.26) with $\bar{\varsigma_\tau}$ for impulse input as follows:

$$g_{lmn}(\tau-\tau_0) = \frac{1}{A_{lmn}} \cdot \frac{u(\tau-\tau_0)\cdot\varsigma_c \cdot w_{lmn}\cdot L^2}{k\cdot(T_{norm}-T_\infty)} \cdot \frac{\sinh(\sqrt{\zeta_{lmn}^2 - w_{lmn}^2}\cdot(\tau-\tau_0))}{e^{\zeta_{lmn}\cdot(\tau-\tau_0)}\cdot\sqrt{\zeta_{lmn}^2-w_{lmn}^2}} \quad (2.27)$$

Hence, the solution of Eq. (2.20) can be explicitly written with Eqs. (2.21), and (2.25) to (2.27) as follows:

$$\vartheta_L = \sum_{l=0}^{\infty}\sum_{m=0}^{\infty}\sum_{n=0}^{\infty}\left[S_{lmn}\varsigma_c \cdot \mathscr{L}^{-1}\left(\frac{\bar{\varsigma_\tau}}{s^2+2\cdot\zeta_{lmn}\cdot s + w_{lmn}^2}\right)\cdot c_{lmn}^3(\vec{\xi})\right] \quad (2.28)$$

$$\vartheta_C = \sum_{l=0}^{\infty}\sum_{m=0}^{\infty}\sum_{n=0}^{\infty}\left[\frac{A_{lmn}\cdot S_{lmn}}{w_{lmn}}\cdot c_{lmn}^3(\vec{\xi})\left(\int_0^\tau \varsigma_\tau(\tau^\circ)\cdot g_{lmn}(\tau-\tau^\circ)d\tau^\circ\right)\right] \quad (2.29)$$

where the subscripts L and C indicate that the solutions are described in terms of the Laplace transform and the convolution integral, respectively.

2.4 Results and discussion

2.4.1 Concept validity check: comparison with Linear TTM solution

The first case study is a validity check of the TTM implementation in ABAQUS. For this purpose, the TTM implementation in ABAQUS is set for solving the linear cases, and the FEM results are compared with the linear TTM solutions of Eqs. (2.28) and (2.29).

Two temporal profiles are considered, a Gaussian and a rectangular profile. The Gaussian profile, S_G, is defined the same way as is done by Chen et al. (2005):

$$S_G(t) \equiv \frac{1}{t_p}\sqrt{\frac{4\ln(2)}{\pi}}\cdot\exp\left[-4\ln(2)\left(\frac{t-2\cdot t_p}{t_p}\right)^2\right] \quad (2.30)$$

And considering the FWHM of the Gaussian profile, the corresponding rectangular temporal profile S_R is defined as:

$$S_R(t) \equiv \frac{1}{t_p}\cdot[u(t-1.5\cdot t_p) - u(t-2.5\cdot t_p)]$$

Two 1-D spatial distributions of interest are the exponentially decreasing (S_E) and

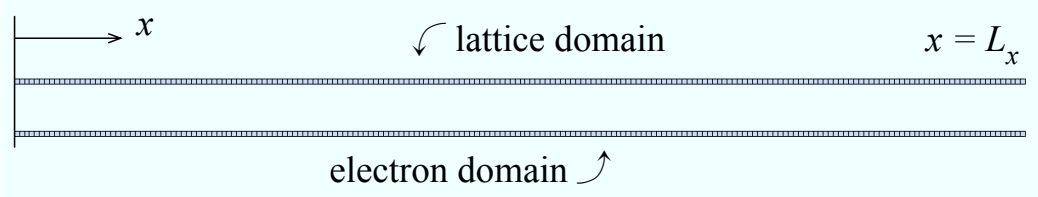

Fig. 2.4. A dual domain setup of the TTM implementation for ABAQUS (L_x = 200 nm, Δx = 1 nm)

step (S_S) distributions. Those are defined as follows:

$$S_E(x) \equiv \frac{1}{\delta_s} \cdot \exp\left(-\left|\frac{x}{\delta_x}\right|\right) \tag{2.31}$$

$$S_S(x) \equiv \begin{cases} 1/\delta_s & \text{if } |x| < \delta_s \\ 0 & \text{if } |x| \geq \delta_s \text{ and } |x| \leq L_x \end{cases}$$

Then, heat sources to be considered can now be written as

$$\begin{aligned} \dot{S}_{RS}(x,t) &\equiv [J \cdot (1-\mathscr{R})] \cdot S_R(t) \cdot S_S(x) \\ \dot{S}_{RE}(x,t) &\equiv [J \cdot (1-\mathscr{R})] \cdot S_R(t) \cdot S_E(x) \\ \dot{S}_{GS}(x,t) &\equiv [J \cdot (1-\mathscr{R})] \cdot S_G(t) \cdot S_S(x) \end{aligned}$$

Gold is selected as the processed material since it has been extensively investigated on laser-matter interaction for femtosecond laser pulses, and there is a significant amount of experimental data available for it. The ambient temperature material properties ($\approx$ 300 K) are used for the case study, as listed in Table 2.1. The lattice thermal conductivity is assumed as $k_l = 0$, i.e., $k = k_e$ for this and subsequent case studies. The domain thickness, L_x, is 200 nm. The element size in the laser input direction, Δx, is 1 nm. 2D 4-node planar pure heat transfer elements (DC2D4) are used, where the y-direction thermal behaviour is inactivated in the user subroutines and boundary conditions of $q(y = 0) = q(y = L_y) = 0$ are applied. The domain setup is shown in Fig. 2.4. A fixed time step (Δt) of 1 fs is used. For linear setting, Fouriers law is selected as the heat flux model. The fluence, J = 0.5 J/cm^2, and the pulse duration, t_p = 100 fs, are applied as laser parameters.

The lattice temperature histories at the top surface of the domain, $x = 0$, and

Table 2.1. Material properties of gold at ambient temperature

Properties	Value	Source
Density(ρ)	19300 kg/m^3	(Mills, 1992)
Specific electron heat capacity (c_e)	1.1 J/kgK	calculated from (Chen et al., 2005)
Specific lattice heat capacity (c_l)	129.5J/kgK	(Touloukian and DeWitt, 1970)
Thermal conductivity (k)	315 W/mK	(Mills, 1992)
Melting point (T_m)	1336 K	$= T_{ref}$, (Mills, 1992)
Electron-phonon coupling factor (G)	$2.6 \times 10^{16} W/m^3K$	(Qiu and Tien, 1993)
Reflectivity ($\mathscr{R}$)	0.93	(Chen et al., 2005)
Skin depth (δ_s)	14.5 nm	(Chen et al., 2005)

distributions at select times are plotted in Fig. 2.5. It is evident from Fig. 2.5 that the FEM results show good agreement with the analytical results, which demonstrates that the TTM implementation of ABAQUS is valid.

Figure 2.5 (a) shows that the temperature responses for different temporal profiles of heat sources give significantly different values only in the initial stages, i.e. roughly between 0.05 and 0.25 ps. With time, the temperature responses coincide, not only at the point $x = 0$, but over the entire domain, Fig. 2.5 (b). Thus the temporal profile of the heat source may not affect the temperature response over a long time period relative to the pulse duration, i.e., after 1 ps for a pulse duration of 100 fs (0.1 ps) in this case. This may be a unique characteristic for laser-material interaction, considering some studies on the effect of pulse profile for longer pulse durations done by Kramer et al. (2002) or Dijken et al. (2003). On the other hand, it is evident from Figs. 2.5 (c) and (d) that different spatial profiles give noticeably different temperature histories at $x = 0$ and the difference keeps increasing during the calculated time range.

2.4.2 Nonlinear case of low fluence input & hybrid element configuration

As mentioned previously, the electron-phonon coupling term $\dot{E}$ and material properties in Eqs. (2.12) to (2.17) can be either constant or functions of variables, including time, location and temperature. That means the TTM implementation can be used

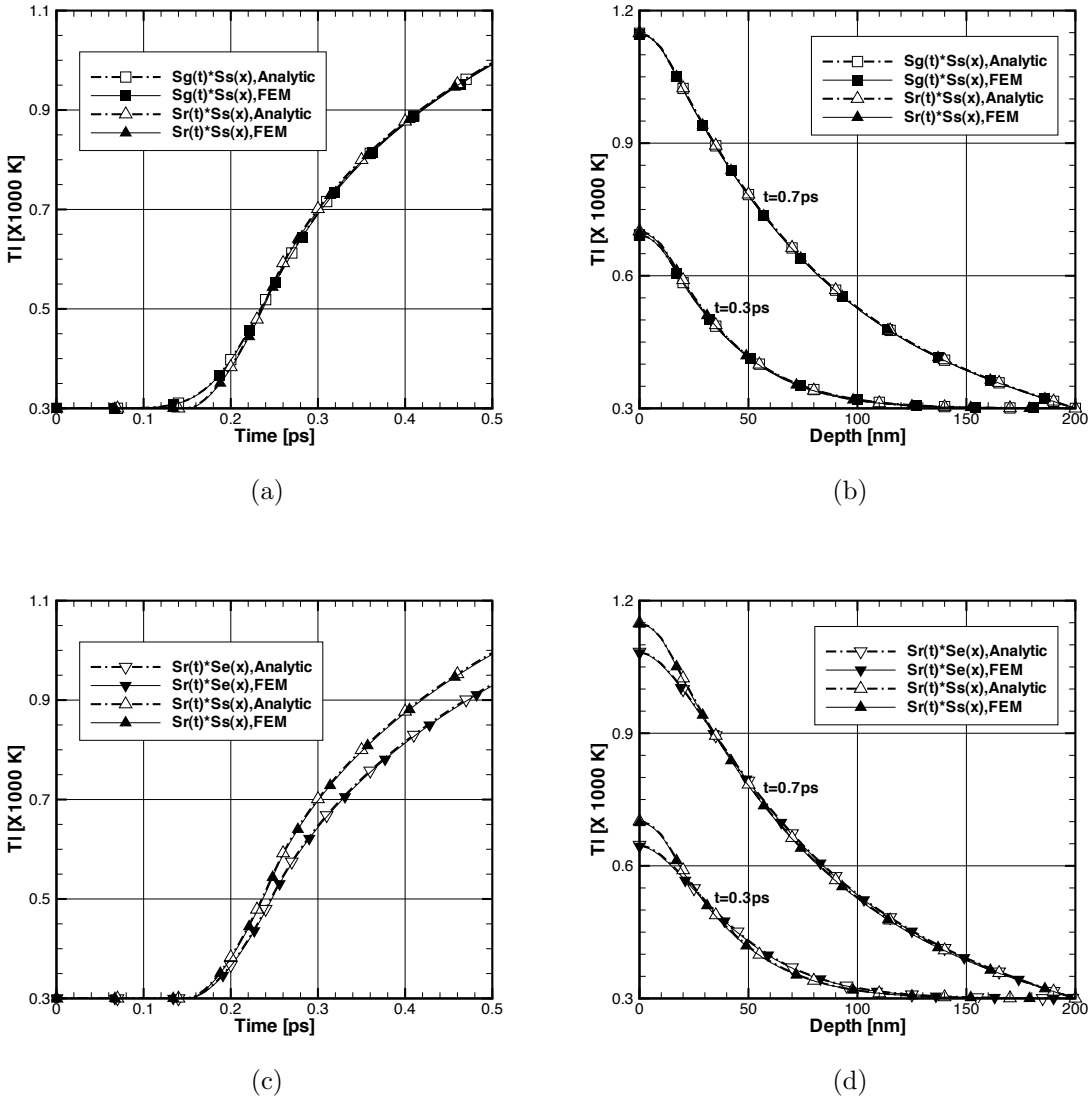

Fig. 2.5. (a) lattice temperature histories at the top surface for heat sources of different temporal profiles, and (b) corresponding temperature distributions at select times; (c) lattice temperature histories at the top surface for heat sources of different spatial distributions, and (d) corresponding temperature distributions at select times: the legend label "FEM" stands for results from ABAQUS, "Analytic" for results from analytical series solutions

for the nonlinear case with temperature dependent material properties. In this case study, a 1-D transient nonlinear problem stated in Qiu and Tien (1993) is investigated. And a hybrid element configuration is discussed for reducing calculation time without loss of precision.

As a temperature dependent electron heat capacity, a simple linear relation is used as follows (Qiu and Tien, 1993):

$$C_e(T_e) = \gamma \cdot T_e, \text{ where} \quad C_e(T_0) = \gamma \cdot T_0 = C_{e0} \tag{2.32}$$

Equations (3.2), (3.3) and (2.4) are adopted as the electron-phonon coupling model, the heat flux model, and the electron thermal conductivity, respectively. Gold is again used as the processed material, and calculation parameters, together with material properties are listed in Table 2.2. A heat source term used in this case study, for spatial and time domains of $0 \leq x \leq L_x$ and $-2t_p \leq t$, is taken from Qiu and Tien (1993) as follows:

$$\dot{S}(x,t) = \frac{J \cdot (1-\mathscr{R})}{t_p} \cdot \frac{1}{\delta_s} \cdot \exp\left(-\frac{x}{\delta_s}\right) \cdot \exp\left(-2.77 \cdot \left(\frac{t}{t_p}\right)^2\right)$$

which has a slightly different temporal profile from Eq. (2.30). For the FEM calculation, the time domain is shifted by $2t_p$, i.e. t in the heat source definition is replaced with $t - 2t_p$, because the starting time of simulation is fixed as zero in ABAQUS. Then, the time domain FEM results are shifted back by $-2t_p$, for comparison with results from Qiu and Tien (1993). Initial and boundary conditions taken from the reference are as follows:

$$\text{IC:} \quad T_e(x,t_0) = T_l(x,t_0) = T_0 \tag{2.33}$$

$$q_e(x,t_0) = q_l(x,t_0) = 0 \tag{2.34}$$

$$\text{BC:} \quad q_e(0,t) = q_e(L,t) = q_l(0,t) = q_l(L,t) = 0 \tag{2.35}$$

where t_0 is set as $-2t_p$ in the reference, but set as 0 for the FEM calculation because of the time domain shift of $t - 2t_p$. 2D planar 4-node pure heat transfer elements (DC2D4) are used to model the dual domain geometry shown in Fig. 2.4, and the

Table 2.2. Parameters for low fluence case study (Qiu and Tien, 1993)

Properties	Value
Reflectivity ($\mathscr{R}$)	0.93
Skin depth (δ_s)	15.3 nm
Thermal conductivity (k_{eq})	315 W/mK
Lattice heat capacity (C_l)	$2.5 \times 10^6 J/m^3K$
Electron heat capacity (C_{e0})	$2.1 \times 10^4 J/m^3K$
Relaxation time (τ_e)	0.04 ps
Initial temperature (T_0)	300 K
Electron-phonon coupling factor (G)	$2.6 \times 10^{16} W/m^3K$
Laser fluence (J)	10 J/m^2

element size Δx is selected as 5 nm for both thicknesses of 100 and 200 nm. For the fixed time steps, Δt, 10%, 2% and 1% of the pulse duration t_p are used.

Figures 2.6 (a) and 2.6 (b) show the normalized homogeneous electron temperature histories for a laser pulse input of $t_p = 96$ fs to different thicknesses, 100 and 200 nm. The normalized homogeneous electron temperature is defined as $(T_e - T_0)/(T_{e,max} - T_0)$, where $T_{e,max}$ is the maximum value of the electron temperature from the results, $T_e(x,t)$. It is evident from Fig. 2.6 that the FEM results agree with the results of Qiu and Tien (1993), especially for the smaller time step Δt of $t_p/50$. It can also be seen from Figs. 2.6 (a) and 2.6 (b) that the effect of the time step size is more critical when the domain size is smaller.

To examine the extreme case of deviation, the electron and lattice temperature distributions in the smaller domain, 100nm, are plotted in Fig. 2.7, which shows relatively good agreement between FEM results and numerical results taken from the reference. The smaller time step is changed to 1% t_p for this figure. It can be seen from Fig. 2.7 (a) that the FEM results for the electron temperature with 1% pulse duration show good agreement with the numerical results of Qiu and Tien (1993), except near the boundary at $x = 100$ nm for $t = 0.1$ ps. As shown in Fig. 2.6 (a), the electron temperature history for $x = 100$ nm changes rapidly between 0 and 0.2 ps. It implies that even a slight time offset between the FEM and numerical results "QT" in Fig. 2.7 will show significant deviation in the spatial domain at a specific

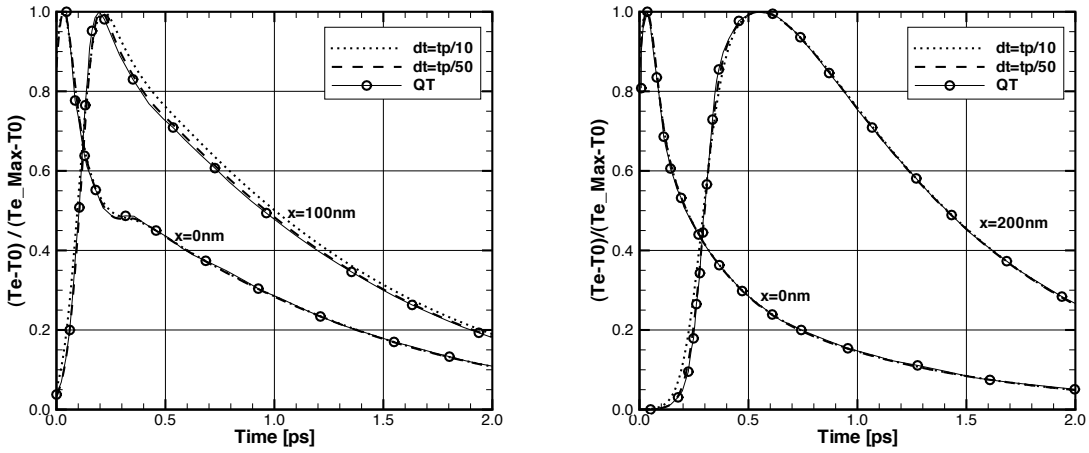

Fig. 2.6. Normalized homogeneous electron temperature histories for a laser pulse of $t_p = 96$ fs at the top and back surface for different material thicknesses of (a) 100 nm, and (b) 200 nm. Data set "QT" taken from Qiu and Tien (1993). In the legend, dt stands for Δt, and tp for t_p

time, especially for $t = 0 \sim 0.2$ ps. On the other hand, the lattice temperature results of the FEM calculation show good agreement with the numerical results of Qiu and Tien (1993), especially for the smaller time step, $\Delta t = t_p/100$.

In general, fewer elements and nodes require less calculation time and computation capability in FEM. A hybrid element configuration with smaller elements close to the heat source, but larger elements for the rest of the domain, Fig. 2.8 (b), is now considered, without loss of precision. The results of the hybrid element configuration are compared with those of the homogeneous element configuration ($\Delta x = 5$ nm) of the previous case study. The hybrid element domain is constructed for the domain thickness of $L_x = 200$ nm, as summarized in Table 2.3. The configuration of $L_x = 1000$ nm will be used in the next case study. A fixed time step Δt of 2 fs is used. The material properties, heat source, IC, BC and heat flux model are the same as in the previous case study. pulse duration, t_p, is 100 fs. The results for the two configurations are compared in Fig. 2.9, which shows that there is no significant deviation between them for both time history and spatial distribution. The computation time for the hybrid configuration is about 78% of that for the homogeneous configuration.

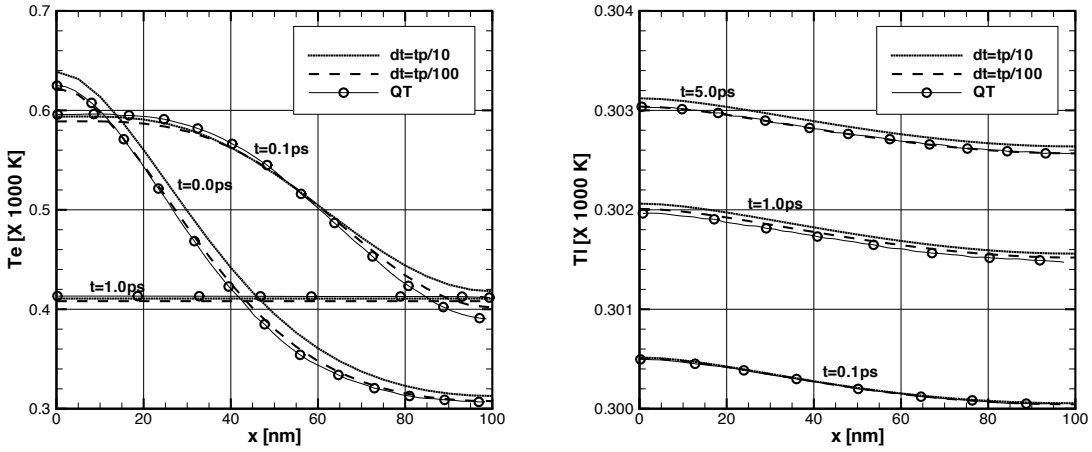

(a) (b)

Fig. 2.7. Temperature distributions inside a material ($L_x = 100$ nm) for a laser pulse of $t_p = 100$ fs at select times: (a) electron temperature, and (b) lattice temperature. Data set "QT" taken from Qiu and Tien (1993). In the legend, dt stands for Δt, and tp for t_p

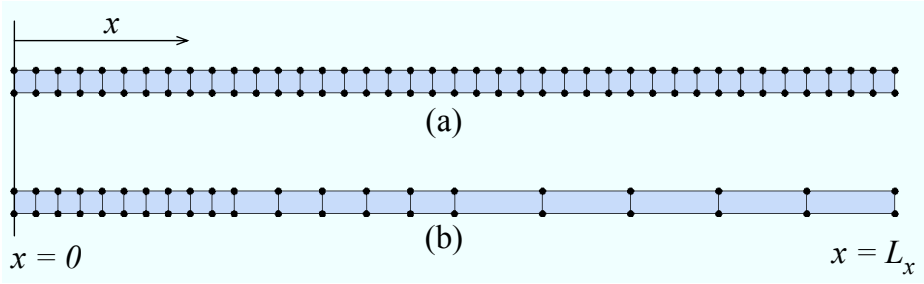

Fig. 2.8. (a) Homogeneous and (b) hybrid element configurations ($L_x = 200$ nm)

Table 2.3. Hybrid element configurations for the thickness of 200 and 1000 nm

Δx	$L_x = 200$ nm	$L_x = 1000$ nm
5 nm	$0 \le x \le 50$	$0 \le x \le 200$
10nm	$50 \le x \le 100$	$200 \le x \le 500$
20nm	$100 \le x \le 200$	$500 \le x \le 1000$

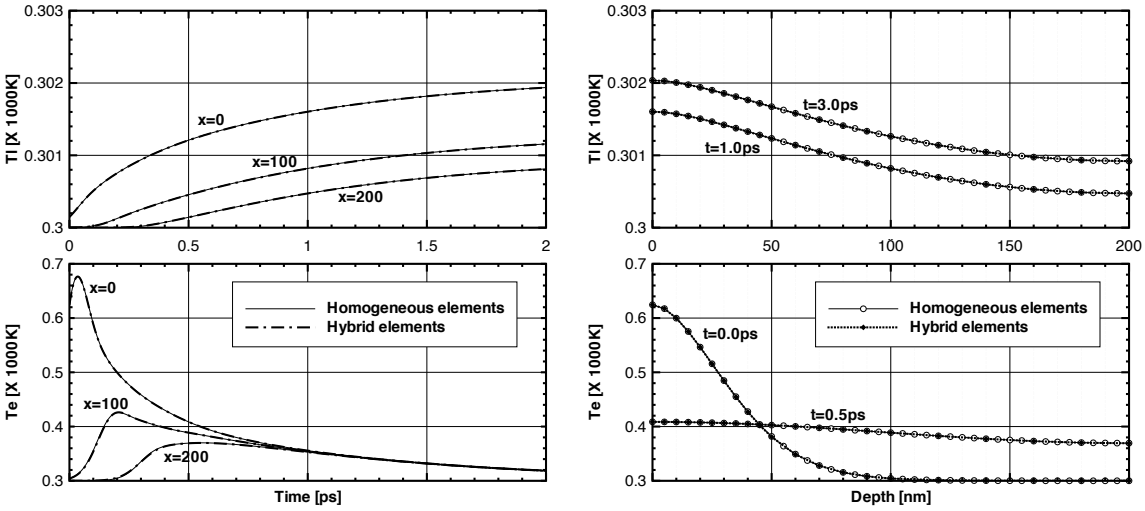

(a) (b)

Fig. 2.9. Comparison of FEM results for homogeneous and hybrid elements: (a) electron and lattice temperature histories at select locations, and (b) electron and lattice temperature distributions at select times. Marks in (b) represent the locations of nodes

2.4.3 Nonlinear case of high fluence input & feasibility of microwelding with UFL

In previous case studies for low fluence laser input, the lattice temperature response varies only within a limited range, near the ambient temperature of 300 K, as can be seen in Fig. 2.7 (b) or Fig. 2.9. Such small temperature changes are not adequate for normal materials processing, for example cutting, drilling or welding. Thus, temperature response under high fluence laser input as stated in Chen et al. (2005) is investigated in this case study. The feasibility of applying UFL to microwelding is then investigated in terms of the existence of a molten pool.

For this case study, Eqs. (3.3), (2.5), (2.6), (3.6) and (2.32) are used for the heat flux model, the electron thermal conductivity, the electron-phonon coupling factor, the electron relaxation time and the electron heat capacity, respectively. The lattice heat capacity of the solid phase is found from the relation , and set as constant for the liquid phase, as was done by Chen et al. (2005). The bulk heat capacity is obtained from Touloukian and DeWitt (1970). Gold is still considered as the processed material and the relevant material properties are listed in Table 2.4 and Table 2.1. The heat

Table 2.4. Material properties of Gold for high fluence case study (Chen et al., 2005)

Properties	Values
Reflectivity ($\mathscr{R}$)	0.93 for $\lambda = 800$ nm 0.332 for $\lambda = 248$ nm
Fermi Temperature (T_F)	$6.4 \times 10^4 K$
Electron heat capacity coeff. (γ)	70 J/m^3K
Coupling factor constant (G_{RT})	$2.2 \times 10^{16} W/m^3 K$
Latent heat (H_m)	$6.275 \times 10^4 J/kg$
Critical point (T_{tc})	7670 K

source term is defined in the same manner as Chen et al. (2005):

$$\dot{S}_{GE}(x,t) \equiv [J \cdot (1 - \mathscr{R})] \cdot S_G(t) \cdot S_E(x)$$

where $S_G(t)$ and $S_E(x)$ are defined in Eqs. (2.30) and (2.31), respectively. Equations (2.33) and (2.34) are adopted as initial conditions, and Eq. (2.35) as the boundary condition. Phase explosion is adopted for the ablation model, i.e. T_{crit} in Eq. (2.19) is selected as 90% of the thermodynamic critical temperature T_{tc}, as assumed in Chen et al. (2005). The homogeneous melting process is assumed, Eq. (2.18), and the hybrid element configuration for $L_x = 1000$ nm in Table 2.3 is adopted. 4-node plane stress elements coupled with temperature (CPS4T) are used for both the electron and lattice domains because the pure heat transfer element (DC2D4) does not support the nodal movement of the elements. $t_p = 500$ fs and $\lambda = 248$ nm are selected as laser parameters. The user subroutine source codes are listed in Appendix C.

Figure 2.10 (a) shows typical lattice temperature responses at the top surface ($x = 0$) and ablation histories for specific input fluences, with $\Delta T_m = 100$ and 500 K, and $\Delta t = 2$ and 5 fs. It can be seen from the figure that those settings give almost the same history for both the lattice surface temperature and ablation depth. On the other hand, those settings result in different spatial temperature distributions, as shown in Fig. 2.10 (b). When ΔT_m is small, the result is severe warpage in the lattice temperature distribution between $x = 70$ and 100 nm at $t = 22.0$ ps, when ablation

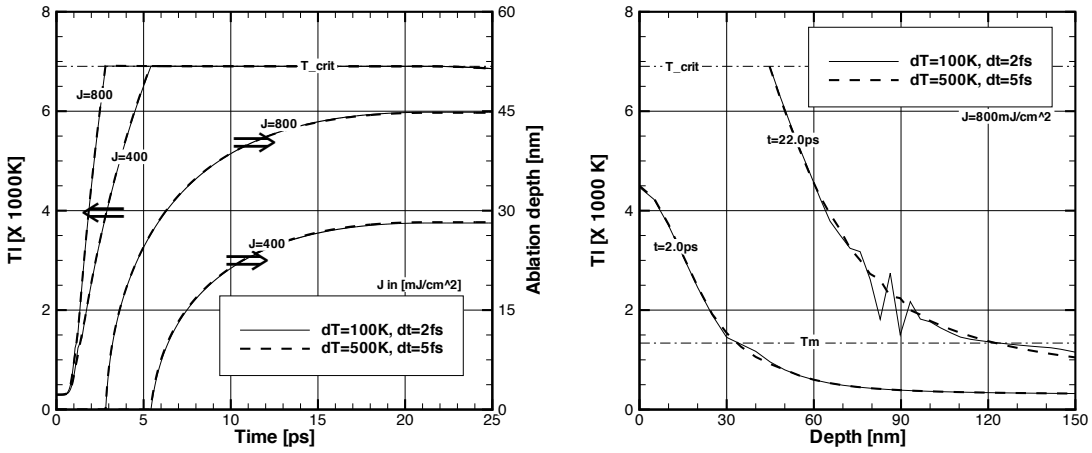

(a) (b)

Fig. 2.10. (a) Lattice temperatures at the top surface and ablation depth histories (b) Lattice temperature distributions for $t = 2.0$ and 22.0 ps, $J = 800$ mJ/cm^2. In the legends, dT stands for ΔT_m, dt for Δt

almost ends. This may due to a relatively large time step (Δt) and element size (Δx) for the ΔT_m. A fundamental approach for eliminating the warpage is using smaller Δx and Δt, but this will demand high computation capacity and long calculation time. For engineering purposes, the warpage can be effectively reduced by using a large ΔT_m, as can be seen from the graph of $\Delta T_m = 500$ K and $\Delta t = 5$fs at $t = 22.0$ ps, Fig. 2.10 (b). $\Delta T_m = 500$ K is therefore used for the rest of this case study.

Figure 2.11 shows the FEM results obtained for the ablation depth calculation for a single laser pulse with given fluence $J > J_{ab}$. The numerical results of Chen et al. (2005) and experimental results of Preuss et al. (1995) are plotted together in Fig. 2.11 (a) for comparison. The average ablation rate, $\dot{d}_{ab}$, in Fig. 2.11 (b) is calculated from the FEM outputs for ablation history as $\dot{d}_{ab} \equiv d_{ab}/(t_{e,ab} - t_{s,ab})$, where d_{ab}, $t_{s,ab}$ and $t_{e,ab}$ are the ablation depth, the starting, and ending time of the ablation, respectively. It can be seen from Fig. 2.11 (a) that the TTM implementation of ABAQUS produces reasonable results for ablation depth, compared with both the numerical and experimental results from the literature. It can also be observed from Fig. 2.11 (b) that the average ablation rate is of the order of 10^3 m/s, which is quite

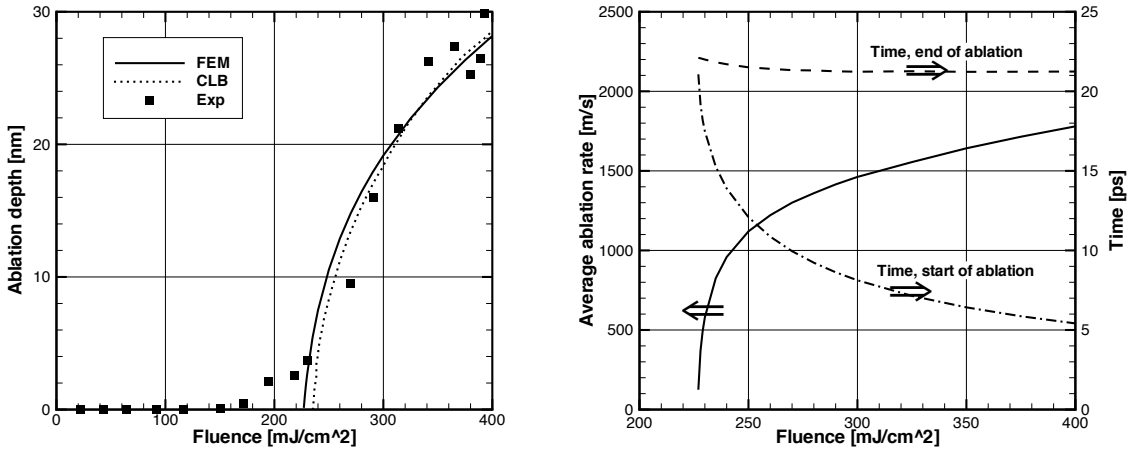

(a) (b)

Fig. 2.11. (a) Ablation depth with respect to the input fluence. Data set "CLB" taken from Chen et al. (2005), and "Exp" from Preuss et al. (1995). (b) Corresponding ablation starting and ending time, and average ablation rate with respect to the input fluence

high and further illustrates the effectiveness of UFL for material removal. Finally, Fig. 2.11 (a) shows that TTM analysis using ABAQUS is feasible for solving laser-matter interaction for high fluence ultra short pulse laser input.

In studying the feasibility of microwelding using UFL, the laser fluence range of interest is increased to include values below the ablation threshold. Even though the effect of convection due to flow of molten material may be significant, as a first approximation, it is not considered in this study due to the small amount of molten pool material involved. A molten pool edge is considered to be located inside the domain at points where the lattice temperature is at the melting point, T_m.

The history of the molten pool edge is shown in Fig. 2.12 (a) for select input fluences. The maximum molten pool thickness is plotted as a function of input fluence in Fig. 2.12 (b). The maximum molten pool thickness for a given fluence, θ_m, is calculated from the FEM results as $\theta_m = d_m - d_{ab}$, where d_m is the maximum molten pool depth of Fig. 2.12 (a), and dab is the ablation depth shown in Fig. 2.11 (a). It can be seen from Fig. 2.12 (a) that the trends of the molten pool edge histories change significantly near the ablation threshold, J_{ab} ($200 < J_{ab} < 250\ mJ/cm^2$). For

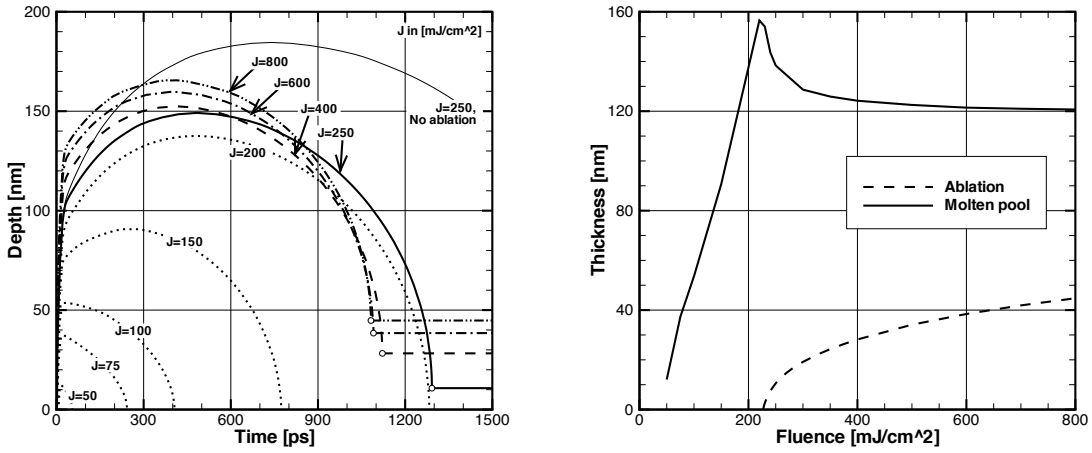

(a) (b)

Fig. 2.12. (a) Molten pool depth change history traced with melting point for select fluences (b) Estimation on molten pool thickness traced with melting point (Tm in the legend) and the liquidus (Tm+dT in the legend), with respect to the input fluence

fluence values lower than the ablation threshold (J_{ab}), the maximum depth of the molten pool and the peak time for the maximum molten pool depth increase as the fluence increases. However, the peak time decreases, while the maximum depth still shows an increasing trend, for fluence values higher than the ablation threshold. This change in trend may occur because ablation removes huge amounts of energy from the domain. Ablation occurs around $5 \sim 20$ ps as shown in Fig. 2.11 (b), which is in the early stages of the molten pool development, which occurs roughly over the time range from 1 ps to 1.5 ns. The effect of ablation on molten pool development can be observed by comparing the "J=250" and "J=250, No ablation" curves in Fig. 2.12 (a), which are obtained from a simulation with or without ablation for $J = 250\ mJ/cm^2$, respectively. It can also be observed from Fig. 2.12 (a) that the molten pool depths at high fluences,$J = 250$, 400, 600 and 800 mJ/cm^2, are nonzero at the end of the process. The different trends of molten pool development can also be clearly seen in Fig. 2.12 (b). For fluence values between the melting threshold J_m ($0 < J_m < 50\ mJ/cm^2$) and the ablation threshold Jab ($200 < J_{ab} < 250\ mJ/cm^2$), the molten pool thickness develops almost linearly. However, the thickness decreases abruptly when

the fluence exceeds the ablation threshold, and then converges to a constant value around 120 nm. The trend of molten pool thickness (θ_m) development with respect to the laser input fluence (J) can thus be briefly summarized as follows:

$$\begin{aligned} \frac{\partial \theta_m}{\partial J} &\approx const(\neq 0) \quad \text{if } J_m < J < J_{ab} \\ \frac{\partial \theta_m}{\partial J} &\approx 0 \quad \text{if } J \gg J_{ab} \end{aligned}$$

In summary, for the pulse duration investigated, the following observations were made: 1) the maximum molten pool size is obtained at the ablation threshold, 2) the maximum molten pool thickness is of the order of 10^2 nm, which implies that the thickness of material to be welded using UFL may have to be restricted to the order of 10^2 nm, and 3) laser-matter interaction under UFL is not free from molten-material on the micron scale, since θ_m is of the order of 10^2 nm. Thus some defects caused by the molten material during traditional laser processing may also occur during laser processing with UFL on a μm-sized material. It is also interesting to note from Fig. 2.12 (a) that the lattice temperature decreases to the melting point, T_m, after about 1.5 ns, i.e. the time scale of lattice temperature response for UFL is of the order of 1 ns. It implies that a pulse repetition rate of the order of $0.1 \sim 1$ GHz ($= 1$ ns^{-1}) may be necessary for thermal interaction between contiguous UFL pulses.

2.5 Conclusions

A general-purpose commercial FEM package, ABAQUS, is used to simulate the two-temperature model. The simulation results are validated by comparison with analytical solutions of the linear TTM and also by experimental results. Nonlinear simulations for low and high fluences are also validated using data from the literature. Thus the TTM can generally be analyzed numerically using ABAQUS.

For the conditions used, the TTM implementation illustrates the effectiveness of material removal process with UFL. The FEM results indicate that the maximum molten pool depth is obtained near the ablation threshold. The analysis depicts that a feasible thickness scale for laser microwelding using UFL is of the order of 10^2 nm.

The FEM results also suggest that a pulse repetition rate of the order of $0.1 \sim 1$ GHz will enable thermal interaction between pulses.

Chapter III

Numerical analysis on the feasibility of laser microwelding of metals by femtosecond laser pulses using ABAQUS

3.1 Introduction

Lasers have been used as a tool for precise materials processing due to its non-contact nature and the high intensity resulting from the ability to focus it to a small diameter. They have proven to have superior ability in fusion welding of various metals (Fabbro et al., 2005; Cao et al., 2006; Richter et al., 2007); dissimilar metals (Triantafyllidis et al., 2003; Mys and Schmidt, 2006; Sierra et al., 2007); even dissimilar non-metallic materials, for example, glass and silicon (Wild et al., 2001). CO_2 or Nd:YAG lasers in continuous wave (CW) mode or with pulse duration of the order of milliseconds are dominant in the laser welding industry (Kalpakjian and Schmid, 2001).

Lasers are considered to be the best choice among a variety of micro-scale material joining methods (Brockmann et al., 2002). Laser welding of thin foils of micrometer thickness has been successfully performed (Abe et al., 2003; Isamu et al., 2004). However, laser welding of components with overall dimensions of the order of microns is still a challenging task. Semak et al. (2003) indicated that pulse durations shorter than 1 ms may enable microwelding of fusion zones of the order of or smaller than 100 μm.

Ultrashort laser pulses, or ultrafast lasers (UFL), of sub-picoseconds pulse duration are considered to have the potential for laser microwelding of fully micron-scale parts. It is known that the conventional heat conduction model is not adequate for analyzing laser-matter interaction for ultrashort laser pulses, due to energy disequi-

librium between electron and lattice subsystems in metals (Kaganov et al., 1957). Even though there have been several models to describe such thermal behavior of a material (Tzou, 1997), the two-temperature model (TTM) proposed by Anisimov et al. (1974) has been widely adopted to understand the laser-matter interaction of ultrashort laser pulses for metals. It describes the interaction in terms of electron and lattice temperatures, and an electron-phonon coupling factor.

Laser-matter interactions of UFL for metals have been investigated experimentally (Preuss et al., 1995; Nolte et al., 1997; Furusawa et al., 1999; Dumitru et al., 2002), focusing primarily on the material removal process, or numerically using special-purpose codes based on the TTM for 1D (Qiu and Tien, 1993; Smith and Norris, 1998) or axisymmetric domain (Chen et al., 2002). The coupling factor of the TTM has also been experimentally measured at room temperature (Stuart et al., 1996; Hostetler et al., 1999; Hohlfeld et al., 2000). In addition, the uniqueness of the UFL for material removal over longer pulse durations has been demonstrated experimentally (Pronko et al., 1995; Chichkov et al., 1996; Zhu et al., 1999). Recently, successful microwelding of glasses with measurable joint strength has been achieved using UFL (Tamaki et al., 2006).

This paper deals with a feasibility study of laser microwelding of metals using UFL. The TTM is implemented using a general-purpose FEM package, ABAQUS, and select laser parameters of pulse repetition rate, pulse duration and focal radius, are examined numerically. Finally, requirements on those laser parameters for feasible microwelding of metals with UFL are proposed.

3.2 Background

Anisimov et al. (1974) proposed the two-temperature model (TTM) as follows:

$$C_e \frac{\partial T_e}{\partial t} = -\vec{\nabla} \cdot \vec{q}_e - \dot{E}(T_e, T_l) + \dot{S}(\vec{s}, t) \tag{3.1a}$$

$$C_l \frac{\partial T_l}{\partial t} = \dot{E}(T_e, T_l) \tag{3.1b}$$

where C_e, C_l, $\vec{q}_e$, and $\dot{S}$ are electron and lattice heat capacities, heat flux, and heat

source, respectively. The energy interaction between electrons and the lattice, $\dot{E}$, is simplified from the work of Kaganov et al. (1957) in terms of electron and lattice temperatures, T_e and T_l, respectively, and a material constant G, as:

$$\dot{E}(T_e, T_l) = \frac{\pi^2 m_e N V_s^2}{6} \cdot (T_e - T_l) \equiv G \cdot (T_e - T_l) \tag{3.2}$$

where m_e, N, and V_s are electron mass, number density of electrons, and speed of sound, respectively. The constant G is the electron-phonon coupling factor.

Qiu and Tien (1993) introduced a damped version of Fouriers law for their numerical analysis of Eq. (3.1). This was originally proposed by Cattaneo in 1948 (Jou et al., 2001) and was used to replace Fourier's law ($q_e = k_e \cdot \partial T_e / \partial x$) in the originally proposed model as follows:

$$\tau_e \frac{\partial q_e}{\partial t} + q_e = -k_e \frac{\partial T_e}{\partial x} \tag{3.3}$$

where k_e is electron thermal conductivity, and the electron relaxation time, τ_e, is assumed to be constant due to the small temperature change in their study. Wang et al. (1994) derived an electron temperature dependent electron-phonon coupling factor, $G(T_e)$, based on the work of Allen (1987), experimental measurement of $\lambda_e \langle \omega^2 \rangle$ $= 23 \pm 4$ meV^2 for gold (Brorson et al., 1990), and their assumptions, as follows:

$$G(T_e) = \frac{\pi \hbar k_B \cdot \lambda_e \langle \omega^2 \rangle}{D(\varepsilon_F)} \int_{-\infty}^{\infty} D^2(\varepsilon) \cdot \left(-\frac{\partial f_e(\varepsilon, T_e)}{\partial \varepsilon} \right) \cdot d\varepsilon \tag{3.4}$$

where $\hbar$ and k_B are Planck's and Boltzmann's constants, respectively, $D(\epsilon)$ is density of state (DOS) of free electrons, and $f_e(\epsilon, T_e)$ is the Fermi-Dirac distribution for free electrons, given as:

$$f_e(\epsilon, T_e) = \left[\exp\left(\frac{\epsilon - \mu(T_e)}{k_B \cdot T_e} \right) + 1 \right]^{-1} \tag{3.5}$$

where $\mu(T_e)$ is the chemical potential. They also considered electron and lattice temperature dependent τ_e as follows:

$$\tau_e = \frac{1}{A_e \cdot T_e^2 + B_l \cdot T_l} \tag{3.6}$$

where $A_e = 1.2 \times 10^7 \ K^{-2} s^{-1}$ and $B_l = 1.23 \times 10^{11} \ K^{-1} s^{-1}$ for gold. Smith and Norris (1998) introduced a density of state (DOS) with free electrons in the s and d

orbits for gold, and adopted Eq. (3.4) in their study as follows:

$$D(\epsilon) = D_s(\epsilon) + D_d(\epsilon) \tag{3.7a}$$

where $D_s(\epsilon)$ and $D_d(\epsilon)$ are simplified densities of state (DOS) for free electrons in s and d orbits, respectively, given as:

$$D_s(\epsilon) = \frac{3N_s}{2\epsilon_F}\sqrt{\frac{\epsilon}{\epsilon_F}} \tag{3.7b}$$

$$D_d(\epsilon) = \frac{N_d}{\epsilon_1 - \epsilon_2}\left\{u\Big(\epsilon - (\epsilon_F - \epsilon_1)\Big) - u\Big(\epsilon - (\epsilon_F - \epsilon_2)\Big)\right\} \tag{3.7c}$$

with $\epsilon_F = 5.5$ eV, $\epsilon_1 = 7.4$ eV and $\epsilon_2 = 2.2$ eV. Lin and Zhigilei (2006) introduced a more complex density of state for d-electrons for their study.

While Kelly and Miotello (1996) discussed that material ablation due to high fluence and short pulse duration can be modeled as a phase explosion model, they also indicated that the subsurface boiling model proposed by Dabby and Paek (1972) as

$$\rho \cdot H_v \cdot \left(\frac{\partial x}{\partial t}\right)_{x=0} = k \cdot \left(\frac{\partial T}{\partial x}\right)_{x=0}$$

should be replaced with one based on the Hertz-Knudsen equation for describing ablation rate at the top surface as follows:

$$\left(\frac{\partial x}{\partial t}\right)_{x=0} = \frac{\alpha_s \cdot P_b}{\rho}\sqrt{\frac{m_a}{2\pi k_B \cdot T_{top}}} \cdot \exp\left[\frac{H_v m_a}{k_B}\left(\frac{1}{T_b(P_b)} - \frac{1}{T_{top}}\right)\right] \tag{3.8}$$

where P_b, $T_b(P_b)$, m_a, ρ, and H_v are boiling pressure, boiling point at pressure P_b, atomic mass, mass density, and heat of vaporization, respectively. The revised subsurface boiling model, Eq. (3.8), has been adopted for laser-matter interaction analysis for laser pulse duration of the order of nanosecond (Craciun et al., 1998; Bulgakova et al., 2004). However, the model has not been used for pulse duration of the order of femtosecond, and it needs consideration for ablation analysis involving femtosecond laser pulse.

In this study, the TTM implementation for a general-purpose FEM package, ABAQUS, is used for studying the feasibility of laser microwelding of metals with UFL. The effects of pulse repetition rate, pulse duration and focal radius are in-

vestigated. For the repetition rate, two consecutive pulses are considered and the relative amount of molten pool generated by two pulses as compared to a single pulse is examined. For the pulse duration, first, the validity of the TTM implementation is checked by comparison with experimental data from the literature. The molten pool development is then investigated for select pulse durations. Finally, for the focal radius, the geometry is extended to axisymmetric 3D using ABAQUS, and the TTM implementation is applied to the case study. In addition, the feasibility of using metals as top coating for laser shock peening is briefly discussed.

3.3 Analysis

3.3.1 Overview of the TTM implementation in ABAQUS

The conventional conduction model in ABAQUS can be expressed in terms of the volumetric internal energy, U, as follows:

$$\rho\frac{\partial u}{\partial t} = -\vec{\nabla}\cdot\vec{q} + \dot{S} \quad \text{or} \quad \dot{U}_{eff} = -\vec{\nabla}\cdot\vec{q} \tag{3.9}$$

where $U_{eff} \equiv U - S$ and the upper dots represent partial differentiation with respect to time. Equation (3.1) can be rewritten using the thermodynamic relation $c = \partial u/\partial T$ as:

$$\dot{U}_{e,eff} = -\vec{\nabla}\cdot\vec{q} \tag{3.10a}$$

$$\dot{U}_{l,eff} = 0 \tag{3.10b}$$

where $U_{e,eff} \equiv U_e + E - S$ and $U_{l,eff} \equiv U - E$. It can be seen from comparison of Eqs. (3.9) and (3.10) that the TTM can be implemented by two geometrically independent but thermally interacting domains, i.e., a dual domain configuration, Fig. 3.1, with user subroutines of ABAQUS, which are UMATHT, USDFLD and UMESHMOTION in this study.

The user subroutine UMATHT allows the user to customize thermal behavior of a material. Thus, Eqs. (3.1) and (3.3) can be coded for ABAQUS in this subroutine. The subroutine is called at integration points of a finite element at each time step,

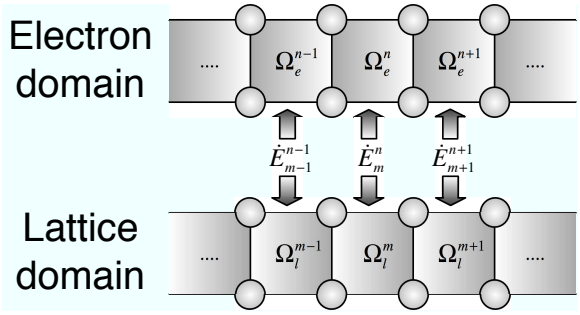

Fig. 3.1. A dual domain configuration for the TTM in ABAQUS

Table 3.1. The updating relations for internal energy and heat flux related terms in the user subroutine UMATHT

Electron system	Lattice system
$U_{e,eff}^{t+\Delta t} = U_{e,eff}^{t} + \left[\left(\frac{\partial U_e}{\partial T_e} \right) \cdot \Delta T_e + \left(\dot{E} - \dot{S} \right) \cdot \Delta t \right]$	$U_{l,eff}^{t+\Delta t} = U_{l,eff}^{t} + \left[\left(\frac{\partial U_l}{\partial T_l} \right) \cdot \Delta T_l - \dot{E} \cdot \Delta t \right]$
$\frac{\partial U_e}{\partial T_e} = C_e$	$\frac{\partial U_l}{\partial T_l} = \frac{U_l}{\rho(T_l)} \cdot \frac{\partial \rho}{\partial T_l} + C_l$
$\frac{\partial U_e}{\partial (\vec{\nabla} T_e)} = \vec{0}$, assumed	$\frac{\partial U_l}{\partial (\vec{\nabla} T_l)} = \vec{0}$, assumed
$q_{e,x}^{t+\Delta t} = \frac{1}{\tau_e + \Delta t} \cdot \left(\tau_e \cdot q_{e,x}^{t} - \Delta t \cdot k_e \cdot \frac{\partial T_e}{\partial x} \right)$	–
$\left(\frac{\partial q}{\partial T} \right)_{e,x}^{t+\Delta t} = \frac{1}{\tau_e + \Delta t} \cdot \left[\tau_e \cdot \left(\frac{\partial q}{\partial T} \right)_{e,x}^{t} + \frac{\partial \tau_e}{\partial T_e} \cdot \frac{\Delta t}{\tau_e + \Delta t} \cdot \left(k_e \frac{\partial T_e}{\partial x} + q_{e,x}^{t} \right) - \Delta t \cdot \frac{\partial k_e}{\partial T_e} \cdot \frac{\partial T_e}{\partial x} \right]$	–
$\left(\frac{\partial q}{\partial (\vec{\nabla} T)} \right)_{e,x}^{t+\Delta t} = \frac{1}{\tau_e + \Delta t} \cdot \left[\tau_e \cdot \left(\frac{\partial q}{\partial (\vec{\nabla} T)} \right)_{e,x}^{t} - \Delta t \cdot k_e \right]$	–

t, and three internal energy and heat flux related terms should be updated by the user for the next time step, $t + \Delta t$. The updating relations for the three internal energy related terms ($U, \partial U/\partial T$ and $\partial U/\partial(\nabla T)$) and three heat flux related terms ($q, \partial q/\partial T$ and $\partial q/\partial(\nabla T)$) are summarized in Table 3.1. It should be noted that material properties and the electron-phonon coupling term in the relations can be either constants or temperature dependent terms. Those can be evaluated in, or passed into this subroutine. It should also be noted that the heat flux model of Eq. (3.3) is considered in the relations.

A user subroutine USDFLD is employed to evaluate the electron-phonon coupling term, $\dot{E}(T_e, T_l)$, and temperature dependent properties, including C_e, C_l, τ_e, ρ and k_e. Most of the terms can be evaluated from temperature information at integra-

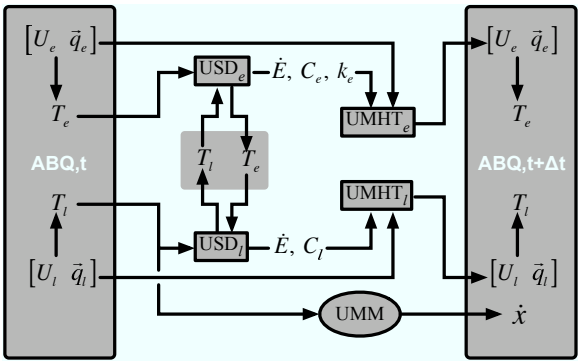

Fig. 3.2. Overall workflow of ABAQUS user subroutines for the TTM implementation: USD stands for USDFLD, UMTH for UMATHT, and UMM for UMESHMOTION

tion points of a finite element in which the subroutine is called, except the coupling term. The coupling term $\dot{E}(T_e, T_l)$ needs both electron and lattice temperatures, but there is a technical difficulty in obtaining temperature of a finite element other than the one calling the subroutine. To resolve this issue, the subroutine reserves a common memory block to provide inter-element temperature information sharing between electron and lattice domains. It should be noted that material properties and the coupling term can be easily passed into the subroutine UMATHT via internal variables provided by ABAQUS.

A user subroutine UMESHMOTION can be used to evaluate deformation due to ablation. The subroutine allows the ablation to be specified in either material removal amount or rates. The amount may be specified in terms of temperature of the top surface for the phase explosion model (Kelly and Miotello, 1996), but the rates should be specified for subsurface boiling model, Eq. (3.8), which is used in this study. In addition, Eq. (3.8) is evaluated using the lattice temperature.

The overall workflow of the subroutines necessary for implementing the TTM for ABAQUS is illustrated in Fig. 3.2, highlighting the variables passed in to and out of the user subroutines. The symbol $[U, \vec{q}]$ in the figure is an abbreviation for all the internal energy and heat flux related variables to be updated in the user subroutine UMATHT. The subscripts, e and l for the user subroutine symbols, UMHT and USD in the figure, indicate that those have two logical branches in them to evaluate different material properties of electron and lattice subsystems.

3.3.2 Evaluation of temperature dependent material properties

In this study, temperature dependent material property models are applied for density, electron and lattice heat capacities, and electron thermal conductivity. The electron-phonon coupling term and the electron relaxation time are also considered as temperature-dependent, Eqs. (3.4) and (3.6). These are all coded in the user subroutine, USDFLD.

The electron heat capacity, $C_e(T_e)$, can be obtained from free electron gas theory as (Ashcroft and Mermin, 1976):

$$C_e(T_e) = \int_{-\infty}^{\infty} (\epsilon - \epsilon_F) \cdot \frac{\partial f_e(\epsilon, T_e)}{\partial T_e} \, d\epsilon \tag{3.11}$$

where $f_e(\epsilon, T_e)$ is given as Eq. (3.5). At this point, it should be noted that $f_e(\epsilon, T_e)$ is unknown unless the chemical potential, $\mu(T_e)$, in Eq. (3.5) is evaluated for a density of state (DOS) of consideration, Eq. (3.7) in this study. The chemical potential $\mu(T_e)$ is also required to evaluate $G(T_e)$, Eq. (3.4).

The chemical potential can be obtained as a function of electron temperature using the conservation of numbers of electrons, $N(T_e)$, for temperature change, i.e., by setting

$$N\big(T_e(>0)\big) = N\big(T_e = 0\big), \quad \text{where } N(T_e) = \int_{-\infty}^{\infty} D(\epsilon) \cdot f_e(\epsilon, T_e) \, d\epsilon$$

It should be noted that $N(T_e = 0)$ is a constant. The evaluated $\mu(T_e)$ for s and d electrons and for the Sommerfeld expansion for s electron only configuration (Ashcroft and Mermin, 1976) are plotted together in Fig. 3.3 (a). As is well known, both chemical potentials show the same value as the Fermi energy at room temperature ($\epsilon_F = 5.5$ eV for gold), for the low temperature range of the figure. But as temperature increases, the chemical potentials deviate from the Fermi energy, to higher values for the s and d electron configuration, or to lower values for the Sommerfeld expansion. These deviations are due to the difference in numbers of free electrons for those configurations, noting that the electron configuration of gold is [Xe] $4f^{14}$ $5d^{10}$ $6s^1$ (Ashcroft and Mermin, 1976), i.e., the $5d$ orbital has 10 times as many electrons as

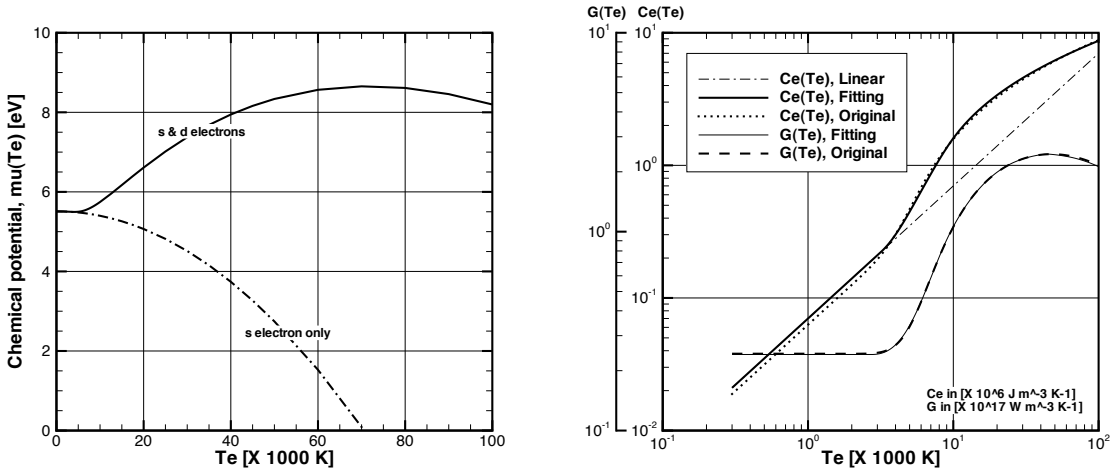

(a) (b)

Fig. 3.3. (a) Chemical potentials evaluated for DOS with s and d electrons and s electron only configurations (b) Curve-fitted $G(T_e)$ and $C_e(T_e)$ with original values; $C_e(T_e)$ of linear model ($C_e = \gamma \cdot T_e$) is also plotted. For the T_e axis, "[X 1000 K]", indicates that the number on the axis should be multiplied by 1000 for the exact value of K, i.e., "40" in (a) should read 40000 K.

the $6s$ orbital, and electrons in the $5d$ orbital are considered as free electrons in the s and d electron configuration, where [Xe] indicates that the electron configuration of inner orbits of gold is identical to that of xenon.

After obtaining $\mu(T_e)$, $G(T_e)$ and $C_e(T_e)$ of Eqs. (3.4) and (3.11) can be evaluated, and curve-fitted in the form of a piecewise function with respect to electron temperature for simple coding in the user subroutine, as follows:

$$C_e(T_e) = \begin{cases} \gamma \cdot T_e & \text{if } T_e < 3200 \text{ K} \\ \displaystyle\sum_{n=0}^{3} a_n \cdot T_e^n & \text{if } 3200 \text{ K} \leq T_e \leq 9500 \text{ K} \\ b_0 + b_1 \cdot T_e^{b_2} & \text{if } T_e > 9500 \text{ K} \end{cases} \tag{3.12}$$

Table 3.2. Coefficients of piecewise curve-fitting functions of Eqs. (3.12) and (3.13)

	$n=0$	$n=1$	$n=2$	$n=3$	$n=4$
a_n	4.093×10^5	-2.067×10^2	5.304×10^{-2}	-2.042×10^{-6}	–
b_n	-9.467×10^6	1.524×10^6	0.215	–	–
c_n	3.167×10^{16}	-3.179×10^{12}	-8.738×10^{-8}	4.446×10^5	-2.521×10^1
d_n	-1.173×10^{17}	3.198×10^{13}	-1.147×10^9	1.956×10^4	-1.306×10^{-1}
e_n	2.320×10^{17}	1.112×10^{12}	-2.308×10^7	1.219×10^2	-2.214×10^{-4}

where $\gamma \approx 70$ J m^{-3} K^{-2} for gold (Wang et al., 1994) and

$$G(T_e) = \begin{cases} G_L(T_e = 2748.6 \text{ K}) & T_e \leq 2748.6 \text{ K} \\ G_L(T_e) = \sum_{n=0}^{4} c_n \cdot T_e^n & 2748.6 \text{ K} < T_e \leq 8476.4 \text{ K} \\ \sum_{n=0}^{4} d_n \cdot T_e^n & 8476.4 \text{ K} < T_e \leq 46269.4 \text{ K} \\ \sum_{n=0}^{4} e_n \cdot T_e^n & T_e > 46269.4 \text{ K} \end{cases} \tag{3.13}$$

It should be noted that Eqs. (3.12) and (3.13) with coefficients listed in Table 3.2 are valid only for specific units, T_e in K, $G(T_e)$ in W m^{-3} K^{-1}, and $C_e(T_e)$ in J m^{-3} K^{-1}. Equations (3.12) and (3.13) are plotted in Fig. 3.3 (b), together with original evaluations used for the curve-fittings. It can be seen from Fig. 3.3 (b) that Eq. (3.11) with $\mu(T_e)$ results in values which are close to the low temperature linear approximated electron heat capacity, $C_e = \gamma \cdot T_e$, for the electron temperature range of $T_e < 3200$ K. This is considered in curve-fitting the low temperature range of Eq. (3.12). It can also be seen from Fig. 3.3 (b) that the electron-phonon coupling factors for both the original evaluation and curve-fitted piecewise function are almost constant at 2.4×10^{16} W m^{-3} K^{-1} for the low temperature range. It should be noted that the constant value for the low temperature range coincides with experimentally measured G at room temperature (Wang et al., 1994).

The mass density, $\rho(T_l)$, is assumed as lattice temperature dependent, and is obtained from a relation between the mass density and the volumetric thermal expansion

coefficient, β, as (Touloukian and DeWitt, 1970):

$$\beta = -\frac{1}{\rho}\left(\frac{\partial \rho}{\partial T_l}\right)_P \quad \text{or} \quad \rho(T_l) = \rho_0 \cdot \exp\left[-\int_{T_0}^{T_l} \beta(T)\, dT\right] \tag{3.14}$$

The volumetric thermal expansion coefficient β is also assumed to be related to the linear thermal expansion coefficient, α, as $\beta = 3\alpha$. The linear thermal expansion coefficient is taken from Touloukian and DeWitt (1970) as a function of temperature for solids, and constant for liquids and gases.

The lattice heat capacity, C_l, is obtained from the specific heat capacity, c, also taken from Touloukian and DeWitt (1970), as $C = \rho c$ and

$$C = C_e + C_l \tag{3.15}$$

The lattice heat capacity is also used for modeling homogeneous phase change between the solid and liquid, as recommended by ABAQUS (ABAQUS Inc., 2006):

$$c_{sl} = \frac{H_m}{2 \cdot \Delta T_m} + \frac{c_{so}(T_{so}) + c_{lq}(T_{lq})}{2}, \quad T_{so} < T < T_{lq}$$

where c_{sl} is effective specific heat capacity during phase change between solid and liquid, c_{so} and c_{lq} are specific heat capacity for the solid and liquid phase, respectively, of gold, and H_m is specific latent heat of gold. Pseudo solidus (T_{so}) and liquidus (T_{lq}) for gold are introduced as $T_{so} = T_m - \Delta T_m$ and $T_{lq} = T_m + \Delta T_m$, with $\Delta T_m = 500$ K in this study.

Finally, the electron thermal conductivity, k_e, can be obtained from C_e of Eq. (3.12) and τ_e of Eq. (3.6) as (Smith and Norris, 1998):

$$k_e(T_e, T_l) = \frac{1}{3} \cdot C_e(T_e) \cdot V_F^2 \cdot \tau_e(T_e, T_l) \tag{3.16}$$

where V_F is the Fermi velocity, $V_F = 1.39 \times 10^8$ cm/s for gold.

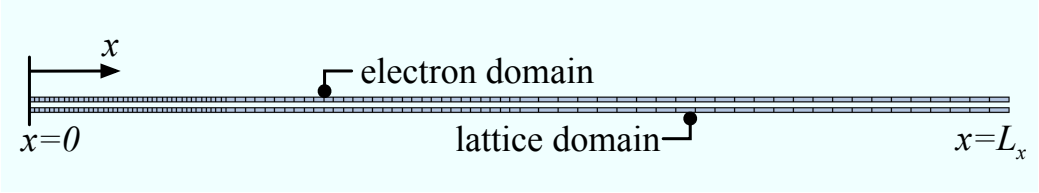

Fig. 3.4. 1D dual domain configuration of TTM implementation for ABAQUS

3.4 Results and discussion

3.4.1 Feasibility of LMW with UFL - multiple pulses

In this case study, the validity of the material model for TTM implementation in ABAQUS and the feasibility of laser microwelding with UFL for single pulse and two consecutive pulses with different repetition rates are examined.

Gold is selected as the processed material, with thickness of $L_x = 1$ μm, since gold has been studied extensively for laser-matter interaction involving femtosecond lasers, even though the material is not widely used in the welding industry. It should be noted that due to differences in material properties for metals frequently used in industry, for example, the ionization potential, significantly different results may be obtained from gold. However gold is considered in this study due to the lack of experimental data for such metals.

The geometry is modeled as a dual domain configuration, Fig. 3.4. The portion near the laser irradiation is modeled with fine elements, but regions farther away are modeled with coarse elements, to reduce computation effort without significant loss of accuracy. 4-node plane stress elements coupled with temperature (CPS4T) of ABAQUS are used for concurrent analysis of temperature response and ablation. As material property models, Eqs. (3.6) and (3.12) to (3.16) are used for electron relaxation time, electron heat capacity, electron-phonon coupling factor, density, lattice heat capacity and electron thermal conductivity. Equation (3.8) is adopted as the ablation model, with an assumption of $\alpha_s = 11$. The value is assumed from comparison between ABAQUS results and the experimental results taken from Preuss et al. (1995). It should be noted that α_s of this study ($= 11$) is significantly larger than the value normally used in the literature (≈ 1). For a laser source, a Gaussian temporal,

Table 3.3. Constants used for the material model and problem set-up

Parameters	Values	Source
Reflectivity ($\mathscr{R}$)	0.93 @ $\lambda = 800$ nm	Chen et al. (2002)
	0.332 @ $\lambda = 248$ nm	Chen and Beraun (2003)
Skin depth (δ_s)	14.5 nm	Chen and Beraun (2003)
Density ($\rho(T_0)$)	19300 kg/m^3 @ $T_0 = 300$ K	Mills (1992)
Melting point (T_m)	3078 K @ 101.3 kPa	Mills (1992)
Initial temperature (T_0)	300 K	–

exponentially decaying spatial profile is considered as (Chen and Beraun, 2003):

$$\dot{S}(x,t) \equiv J \cdot (1-\mathscr{R}) \cdot \frac{\sqrt{b/\pi}}{t_p \cdot \delta_s} \cdot \exp\left[-\left(\frac{x}{\delta_s}\right) - b \cdot \left(\frac{t-2t_p}{t_p}\right)^2\right] \tag{3.17}$$

with $b = 4\ln(2)$, wavelengh $\lambda = 248$ nm, and pulse duration $t_p = 500$ fs. Reflectivity is assumed as temperature independent, but wavelength dependent. Boundary conditions (BC) and initial conditions (IC) are considered as follows (Chen and Beraun, 2003):

$$\text{IC:} \quad T_e(x,0) = T_l(x,0) = T_0 \qquad q_e(x,0) = 0 \tag{3.18a}$$

$$\text{BC:} \quad q_e(0,t) = q_e(L_x,t) = 0 \tag{3.18b}$$

In addition, adiabatic boundary condition for the y-direction ($q_y = 0$) is also applied. Related constants are summarized in Table 3.3.

Comparison between our numerical results and experimental data taken from Preuss et al. (1995) are shown in Fig. 3.5 (a) for ablation depth with respect to input fluence, indicating good correlation between them. This indicates that the material models used in this study and the subsurface boiling model are appropriate for analyzing laser-matter interaction for ultrashort laser pulses. It is interesting to note that even though the results from the phase explosion model (Chen and Beraun, 2003) shows reasonably good correlation with experimental data, the subsurface boiling model results in slightly better results for the low input fluence range of 100 $\sim$ 300 mJ/cm^2, which is the fluence range of interest in this study. The corresponding molten pool evolution is examined using the lattice temperature distribution. A

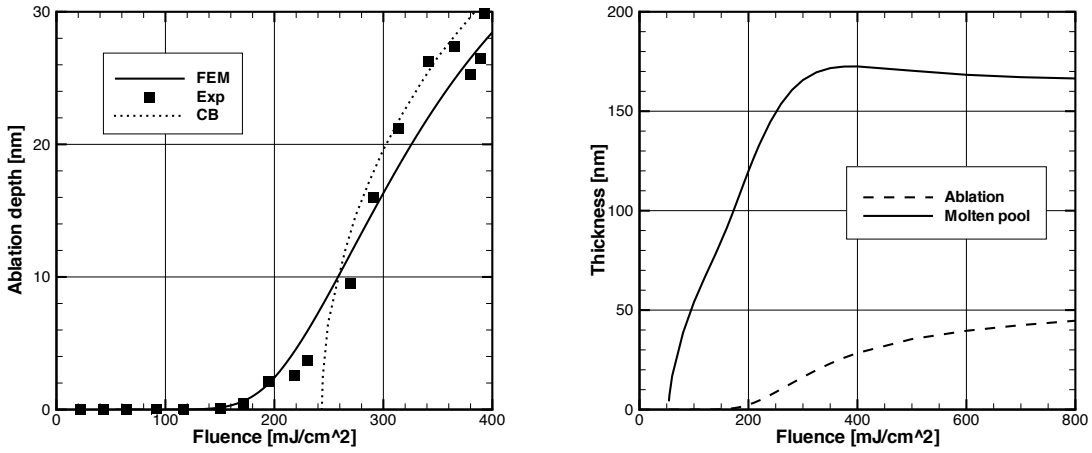

(a) (b)

Fig. 3.5. (a) Ablation depth with respect to input fluence. Data set "Exp" taken from Preuss et al. (1995), and "CB" from Chen and Beraun (2003). (b) Maximum molten pool thickness and ablation depth with respect to input fluence

molten pool edge is determined as a location inside a lattice domain where its lattice temperature is equal to the melting point. Molten pool flow is neglected. Then, the amount of molten material available for fusion welding can be estimated from the molten pool thickness, $\theta_m \equiv d_m - d_{ab}$, where d_m and d_{ab} are maximum molten pool depth and ablation depth, respectively. Variation of the molten pool thickness with fluence is shown in Fig. 3.5 (b), where it is seen that the molten pool thickness increases for low fluences, but saturates ($\approx$ 170 nm) as fluence increases:

$$\frac{\partial \theta_m}{\partial J} \approx const(> 0) \qquad \text{if } J < J_{ab} \tag{3.19a}$$

$$\frac{\partial \theta_m}{\partial J} \approx 0 \qquad \text{if } J \gg J_{ab} \tag{3.19b}$$

Such change of trend in molten pool thickness occurs due to significant ablation for high fluence, shown as the dashed curve in the figure. It is interesting to note that the overall trend of molten pool thickness with respect to fluence is similar to results from the phase explosion model, except that the phase explosion model shows a sharp transition between the two trends at the ablation threshold, while the subsurface boiling model in Fig. 3.5 (b) shows a smooth transition. In summary, these trends

of molten pool evolution indicate that only a limited amount of molten pool can be obtained from a single ultrashort laser pulse, regardless of input fluence, which is a disadvantage for welding. But, it should also be noticed that the limited molten pool evolution can be considered as favorable for precise material removal.

The limitation on molten pool development may still exist for multiple pulses if repetition rates are low, since the temperature then cools down to its initial temperature between pulses. To study this case, two consecutive pulses with high repetition rates in the range of $0.1 \sim 10$ GHz are considered. Pulse duration of 500 fs and low input fluence of 100 mJ/cm^2 are selected as laser parameters. A low fluence is used to minimize the ablation effect. A heat source term for two pulses ($\dot{S}_2$), which replaces the heat source ($\dot{S}$) of Eq. (3.1) in this case study, is defined as follows:

$$\dot{S}_2(x,t) = \begin{cases} \dot{S}(x,t) & \text{if } t < 1/f \\ \dot{S}(x,t) + \dot{S}(x,t-1/f) & \text{if } t \geq 1/f \end{cases}$$

where f is the pulse repetition rate, and $\dot{S}(x,t)$ is defined in Eq. (3.17). It is assumed that there is no surface condition change of the target material after the first irradiation, i.e., the same reflectivity is used for both pulses. The calculation was conducted over a long enough period to account for heating and cooling of the material due to the two pulses.

Molten pool evolution histories for select repetition rates are shown in Fig. 3.6 (a). It can be observed from the figure that repetition rates higher than 2.5 GHz will enable continuous existence of molten pool inside the material. To demonstrate the effect of multiple pulses, the maximum relative molten ($\theta_{m,2/1}$) and ablation ($\theta_{ab,2/1}$) thicknesses are defined as $\theta_{m,2/1} \equiv \theta_{m,2}/\theta_{m,1}$ and $\theta_{ab,2/1} \equiv \theta_{ab,2}/\theta_{ab,1}$, respectively, where $\theta_{m,1}$ and $\theta_{m,2}$ are maximum molten pool thickness after the first and second pulse, and $\theta_{ab,1}$ and $\theta_{ab,2}$ are ablation thickness after the first and second pulse, respectively. Those are plotted in Fig. 3.6 (b). The figure shows that the molten pool thickness after the second pulse is generally larger than the one after the first pulse. It can also be observed that the molten depth saturates as repetition rates increase, due to increased ablation for the high repetition rates. It is interesting to note that

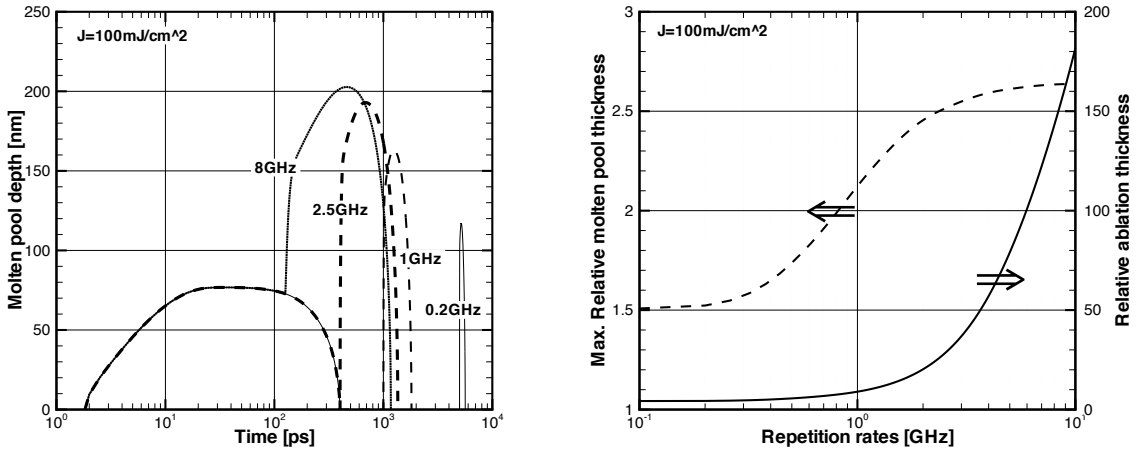

(a) (b)

Fig. 3.6. (a) Lattice temperature histories at the top surface for select pulse repetition rates. (b) Maximum relative molten pool and ablation thicknesses with respect to repetition rates. In the figure, pulse duration is 500 fs.

two pulses at high repetition rates result in more than two and a half times deeper molten pool thickness. Thus, repetition rates on the order of 10 GHz are expected to enable more molten pool in the target material, which may provide favorable conditions for laser micro welding with UFL. However the ablation rate also increases with repetition rate. On the other hand, the high repetition rates may not be appropriate for material removal, due to the increased molten pool generation.

3.4.2 Feasibility of LMW with UFL - pulse duration

The second case study involves the feasibility of laser microwelding for different pulse durations. Pulse durations in the range from fs to sub-ns are considered with the TTM implementation in ABAQUS. The validity of the TTM implementation for different pulse durations is examined by comparison with experimental results from the literature. The effect of pulse duration on molten pool generation is then investigated numerically. Finally, local disequilibrium for different pulse durations is investigated, which is closely related to the validity of the conventional heat conduction model with respect to pulse duration.

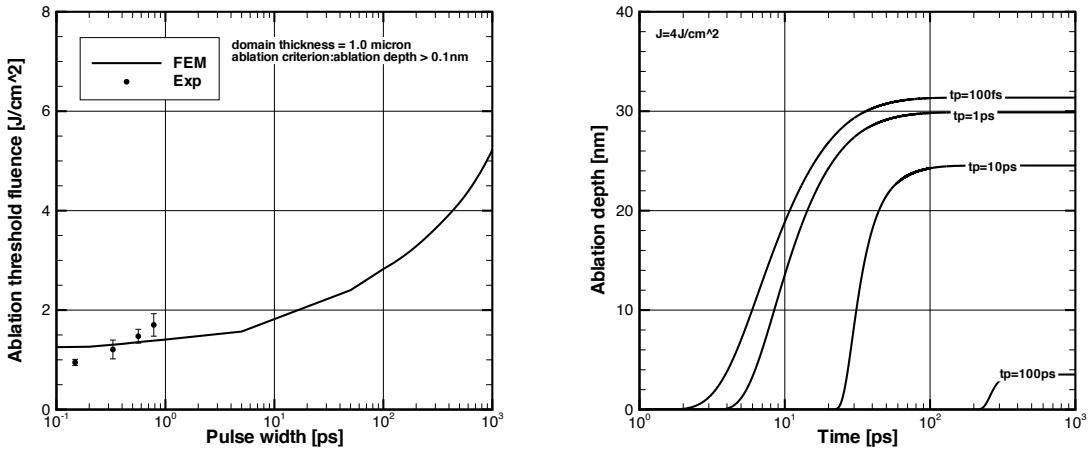

(a) (b)

Fig. 3.7. (a) Ablation threshold fluence with respect to pulse duration. Experimental data set "Exp" taken from Furusawa et al. (1999). (b) Ablation histories at the top surface for select pulse durations with $J = 4$ J/cm^2.

The material to be processed is again selected as gold. Boundary conditions, initial conditions, the material model and the related constants are identical to the previous case study except for the heat source reflectivity, due to the change of laser wavelength to $\lambda = 800$ nm, from 248 nm of the previous case study. The corresponding reflectivity is listed in Table 3.3. The pulse duration range of interest is 100 fs $\leq t_p \leq$ 100 ps.

The ablation threshold fluence is defined as the fluence that results in an ablation depth of 0.1 nm in this study. The threshold fluences are obtained from interpolative calculations for a given pulse duration while varying fluences to obtain the ablation depth of 0.1 nm. The numerical results of ablation threshold fluence obtained from ABAQUS and experimental results of Furusawa et al. (1999) are compared in Fig. 3.7 (a). Both results show overall increasing trends of ablation threshold fluence as pulse duration increases, which demonstrate validity of the model for qualitative estimations. Corresponding ablation histories for different pulse durations with $J = 4$ J/cm^2 are shown in Fig. 3.7 (b). The figure shows that shorter pulse duration results in deeper ablation depth for a given fluence. This demonstrates that shorter pulse

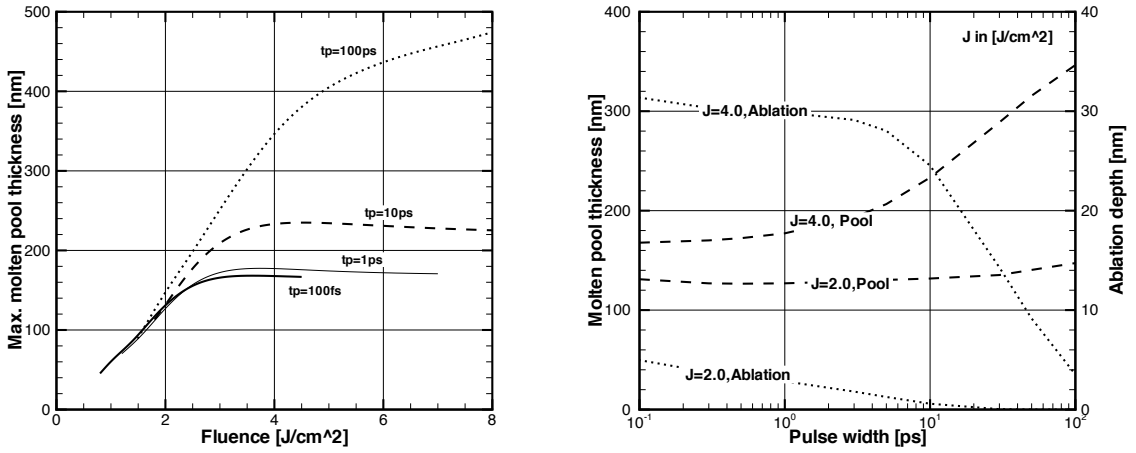

(a) (b)

Fig. 3.8. (a) Maximum molten pool thickness with respect to input fluence for select pulse durations. (b) Corresponding molten pool thickness and ablation depth with respect to pulse duration

durations are favorable for material removal.

Next, the effect of pulse duration on molten pool thickness is examined by tracking the molten pool edges for select pulse durations, as shown in Fig. 3.8. In the figure, all the pulse durations show similar molten pool generation trends for low fluence of $J < J_{ab}$, i.e., Eq. (3.19a) is still valid for long pulse durations. However, the long pulse duration of 100 ps in the figure shows a significantly different trend from the short pulse durations, Eq. (3.19b), in which the molten pool thickness increases as fluence increases. Thus, Eq. (3.19b) for $J \gg J_{ab}$ should be revised for pulse durations as follows:

$$\frac{\partial \theta_m}{\partial J} \approx 0 \qquad \text{if } t_p \leq 10 \text{ ps} \tag{3.20a}$$

$$\frac{\partial \theta_m}{\partial J} \gg 0 \qquad \text{if } t_p \gg 10 \text{ ps} \tag{3.20b}$$

It is interesting to note from Fig. 3.7 (b) and Fig. 3.8, especially for the higher fluence of 4 J/cm^2, that the molten pool thickness increases but ablation depth decreases, as pulse duration increases. Thus, it can be deduced that ablation and molten pool dominant pulse duration ranges are mutually exclusive. In addition to the energy

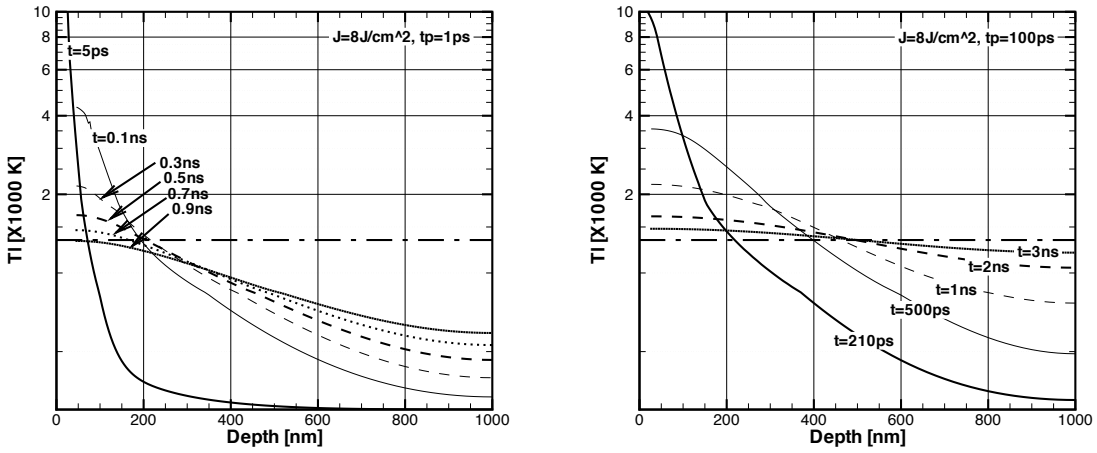

(a) (b)

Fig. 3.9. Lattice temperature distributions at select times with fluence of 8 J/cm^2 for pulse duration of (a) 1 ps, and (b) 100 ps; Horizontal dot-dashed line in both figures represents the melting point.

removal effect of ablation, the exclusiveness may also be related to the dependence of thermal penetration depth (δ_{th}) on the time scale of energy supply, i.e. $\delta_{th} = \sqrt{\kappa \cdot t_p}$, where κ and t_p are the thermal diffusivity and laser pulse duration, respectively. These imply that 1) longer pulse durations provide more favorable conditions for laser microwelding of micrometer-scaled objects than shorter pulse durations, 2) the input fluence should be stable for laser microwelding with longer pulse durations to avoid total melting of the objects.

The lattice temperature distributions at select times for different pulse durations, $t_p = 1$ and 100 ps, are shown in Fig. 3.9. The figures indicate that temperatures do not return to their initial value of T_0 at the final steady state, but converge to a final equilibrium temperature higher than T_0, mainly due to the adiabatic boundary condition, Eq. (3.18), for the limited domain size. In other words, the boundary condition neglects energy loss across the boundary, which may not represent the real situation correctly, especially for an energy input and response over a long time in small domain. However, the boundary condition is adequate for investigating the thermal behavior of a material in the initial stages of the response. Those show that

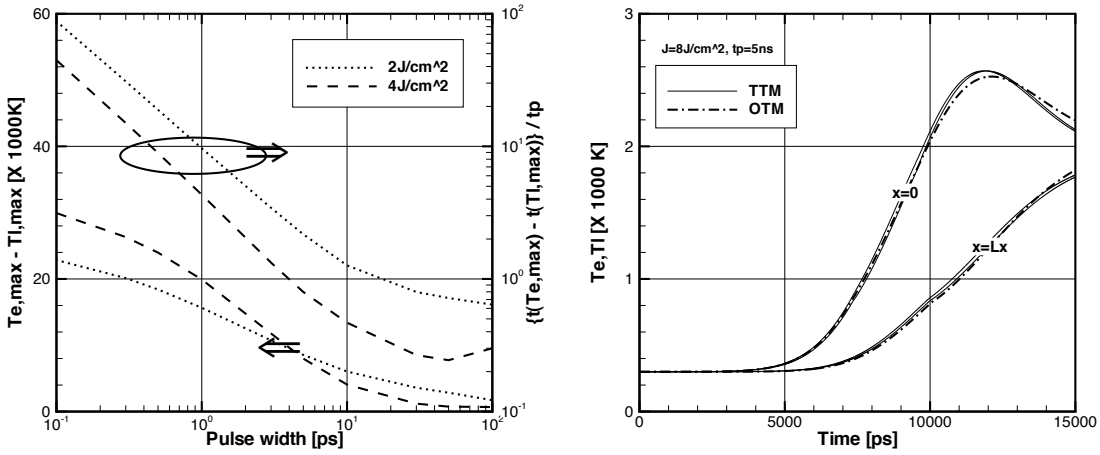

(a) (b)

Fig. 3.10. (a) Difference between maximum electron and lattice temperature for select fluences with respect to pulse duration, and corresponding relative time delay between electron and lattice maximum temperatures; in the figure, "Te,max" and "Tl,max" represent $T_{e,max}$ and $T_{l,max}$, respectively. (b) Comparison of temperature histories at the top and bottom surface evaluated from the TTM and conventional heat conduction model (denoted as "OTM" in the legend) for $t_p = 5$ ns, $J = 8$ J/cm^2; in the figure, Te and Tl represent T_e and T_l, respectively.

longer pulse durations result in higher temperatures in the overall domain and at the other end of the domain as time proceeds, i.e. deeper thermal penetration.

It is well known that the pulse duration is closely related to local disequilibrium between electrons and the lattice of a metal. To quantify the disequilibrium, the difference between electron and lattice temperatures, ΔT_{max}, and relative time delay between temperatures, $\Delta t(T_{max})$, are defined as:

$$\begin{aligned} \Delta T_{max} &\equiv T_{e,max} - T_{l,max} \\ \Delta t(T_{max}) &\equiv \big(t(T_{l,max}) - t(T_{e,max})\big)/t_p \end{aligned}$$

where $T_{e,max}$ and $T_{l,max}$ are maximum electron and lattice temperatures, respectively, for given laser input and $t(T_{e,max})$ and $t(T_{l,max})$ are times when electron and lattice temperatures reach their respective peaks. The temperature deviation and the relative time delay are shown in Fig. 3.10 (a), which shows that both temperature deviation and relative time delay decrease as pulse duration increases. More specifically, the

relative time delay shows a simple dependency on fluence, with higher fluence resulting in lower relative time delay. However, the temperature deviation shows a different trend from the time delay, i.e., higher fluence results in higher temperature deviation for shorter pulse durations than lower fluence, but lower deviation for longer pulse durations. Thus, the disequilibrium is negligible for laser pulse with longer pulse durations. To demonstrate this, when the energy interaction term, $\dot{E}$, is eliminated from Eq. (3.1) with $T = T_e = T_l$, we have

$$\left(C_e + C_l\right) \cdot \frac{\partial T}{\partial t} = \vec{\nabla} \cdot \vec{q}_e + \dot{S}$$

This is identical to the conventional heat conduction equation. Both the conventional heat conduction model and the TTM give similar results, Fig. 3.10 (b), for long pulse duration ($t_p \geq 5$ ns) and high fluence ($J = 8$ J/cm^2). Thus, the conventional heat conduction model is appropriate for pulse durations of the order of ns.

3.4.3 Feasibility of LMW with UFL - focal radius

The last case study is the effect of focal radius on feasibility of laser microwelding, which is analyzed using an axisymmetric 3D domain in ABAQUS.

The geometry is illustrated in Fig. 3.11 (a), with radius (R) and thickness (Z) of 3.0 and 0.5 μm, respectively. The domain is constructed using finite element "CAX4T", which replaces "CPS4T" of the 1D linear configuration.Gold is the processed material, as in the previous case studies. An axisymmetric heat source is defined for Gaussian and exponentially decaying distributions in the radial (r) and depth (z) coordinates, respectively, and Gaussian temporal profile as:

$$\dot{S}(x,t) \equiv J \cdot (1 - \mathscr{R}) \cdot \frac{\sqrt{b/\pi}}{t_p \cdot \delta_s} \cdot \exp\left[-\left(\frac{r}{r_f}\right)^2 - \left(\frac{z}{\delta_s}\right) - b \cdot \left(\frac{t - 2t_p}{t_p}\right)^2\right]$$

Initial (IC) and boundary (BC) conditions are also extended for axisymmetric 3D

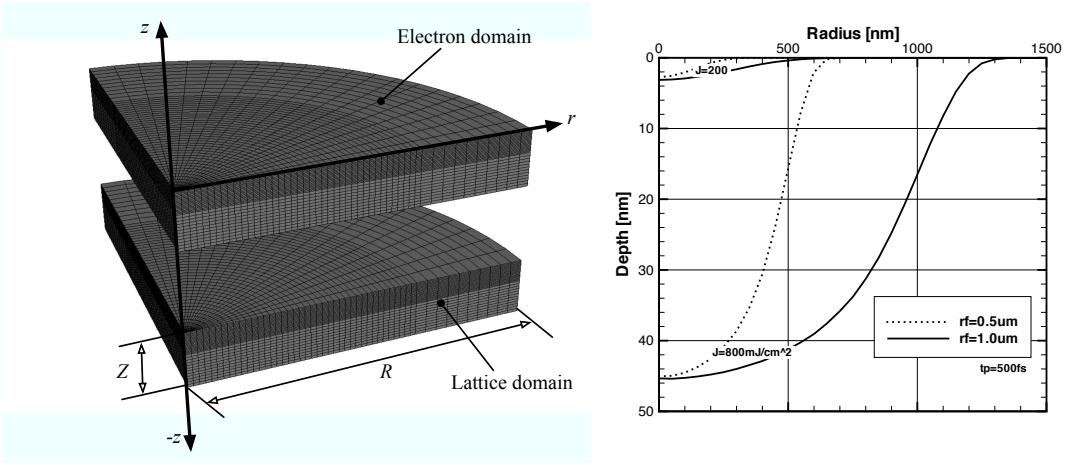

(a) (b)

Fig. 3.11. (a) Axisymmetric 3D dual domain configuration. (b) Ablated top surface ($z = 0$) profile for select focal radii and fluences. Note that unit length scales are different for depth and radius coordinates.

geometry as follows:

$$\text{IC:} \qquad T_e(r,z,0) = T_l(r,z,0) = T_0, \qquad q_e(r,z,0) = 0$$

$$\text{BC:} \qquad q_e(r,0,t) = q_e(r,Z,t) = 0, \qquad q_e(0,z,t) = q_e(R,z,t) = 0$$

For laser parameters, wavelength $\lambda = 248$ nm, focal radii $r_f = 0.5$ and 1.0 μm, pulse duration $t_p = 0.5$ and 500 ps, and fluence $J = 200$, 400 and 800 mJ/cm^2 are considered.

The ablated profiles of the top surface ($z = 0$) for select fluences and focal radii at $t_p = 0.5$ ps are shown in Fig. 3.11 (b). As the figure indicates, different focal radii with the same fluence result in the same maximum depth at the center ($r = 0$), and smaller focal radius with the same energy per pulse results in deeper ablation depth, as can be seen from comparison between the cases of $J = 200$ with $r_f = 1.0$ μm and $J = 800$ with $r_f = 0.5$ μm. Thus for a given energy input, a smaller focal radius with higher fluence may be more efficient for precise material removal, and that fluence is one of the key parameters that determines ablation depth.

Molten pool edges at select times for $r_f = 0.5$ μm, $J = 800$ mJ/cm^2 and $t_p = 0.5$ ps are shown in Fig. 3.12 (a). It is evident that the molten pool is relatively

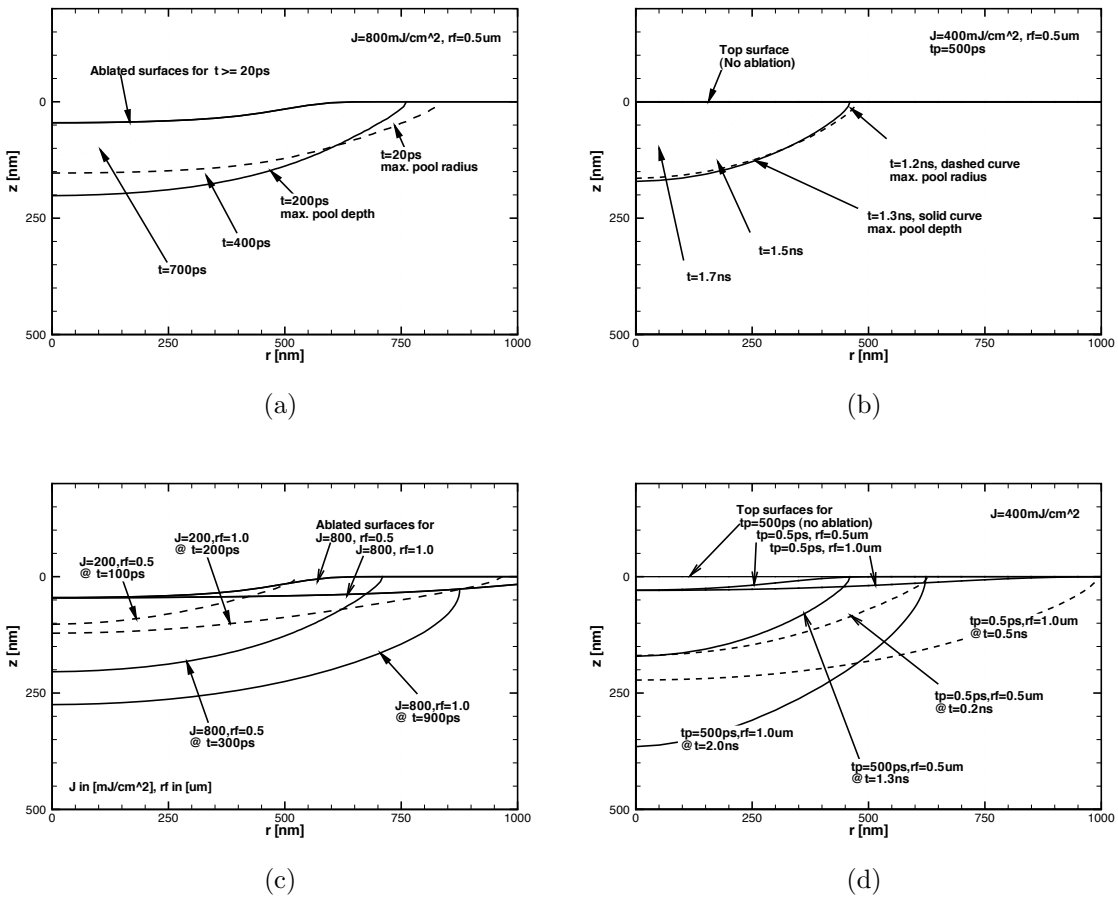

Fig. 3.12. Molten pool edge and top surface profile developed by a beam radius of $r_f = 0.5$ μm at select times for (a) $J = 800$ mJ/cm^2 and $t_p = 0.5$ ps, and for (b) $J = 400$ mJ/cm^2 and $t_p = 500$ ps; Comparison of molten pool edges developed by select beam focal radii at the times of maximum depths for (c) select fluences and $t_p = 0.5$ ps, and (d) select pulse durations and $J = 400$ mJ/cm^2

shallow for short pulse durations. It takes about 10 ps for the molten pool to reach its maximum size in the radial direction, but of the order of 100 ps for the depth. On the other hand, as can be seen from Fig. 3.12 (b) for a longer pulse duration $t_p = 500$ ps, the time scale for the molten pool development in the depth and radial directions are similar, i.e., maximum pool diameter at $t = 1.2$ ns and maximum pool depth at $t = 1.3$ ns. Molten pool edges of select fluences and focal radii for $t_p = 0.5$ ps at the time of maximum pool depth are shown in Fig. 3.12 (c). It is interesting to note from the figure that different maximum molten pool depths are obtained for the same fluence when the focal radius is changed, i.e., a deeper molten pool can be obtained for a larger focal radius with the same fluence, which corresponds to a higher energy per pulse. This trend is different from the one observed for the ablation depth and input fluence. Also, a higher fluence results in a deeper molten pool depth for the same energy per pulse, as can be seen by comparing the cases of $J = 200$ with $r_f = 1.0$ μm and $J = 800$ with $r_f = 0.5\mu$m. Thus, higher energy per pulse and fluence may provide more favorable conditions for laser microwelding with UFL. However, from the viewpoint of precise material removal, smaller focal radius and energy per pulse might be preferable, as it would result in better quality with reduced molten material. It can be seen from Fig. 3.12 (d) that longer pulse durations can produce similar or deeper molten pools for the same fluence. As focal radius increases, shorter pulse durations result in significant increase in molten radius, while longer pulse durations increase the depth. Thus longer pulse durations enable more favorable conditions for laser microwelding for a given fluence or energy per pulse.

3.5 Conclusions

The feasibility of laser microwelding using ultrafast lasers is numerically investigated for select parameters of pulse repetition rate, pulse duration, and focal radius, by implementing the two-temperature model in ABAQUS. A material model is constructed using models derived from physics and the subsurface boiling model for ablation. The validity of the model is investigated by comparison with experimental

results from the literature.

For the conditions examined, the results indicate that laser microwelding is feasible for 1) low fluence ultrashort pulses with high repetition rates of the order of $1 \sim 10$ GHz, 2) longer pulses from a stable laser generator with high fluence capability, or 2) larger focal radius for a given fluence i.e., high energy per pulse and fluence. On the other hand, the results indicate that lower repetition rate, shorter pulse duration, and smaller focal radius for a given fluence provide favorable conditions for precise material removal such as laser cutting or drilling, as those conditions maximize ablation, and minimize molten pool generation.

Chapter IV

Experimental investigation of laser shock peening using femtosecond laser pulses

4.1 Introduction

Surface treatment has been widely used to improve wear and fatigue resistance in several applications (Kalpakjian and Schmid, 2001). Laser shock peening is known to be superior to conventional shot peening for such surface treatment since it results in deeper compressive residual stresses and smoother processed surface, and is also more suited for localized processing (Montross et al., 2002).

Following early studies on momentum transfer (Gregg and Thomas, 1966) and stress waves generation inside a target metal (Anderholm, 1970) due to laser pulses, laser shock peening (LSP) for surface treatment has been intensively investigated for various materials, including steel (Peyre et al., 2000; Yilbas et al., 2003; Yakimets et al., 2004; Aldajah et al., 2005; Farrahi and Ghadbeigi, 2006), aluminum (Fairand et al., 1972; Peyre et al., 1996; Hong and Chengye, 1998; Rubio-González et al., 2004; Tan et al., 2004) and nickel alloy, molybdenum and copper (Forget et al., 1990; Hammersley et al., 2000; Kaspar et al., 2000; Zhang et al., 2004). It has also been successfully applied to improve fatigue life of automotive ring and pinion gears and aircraft engine turbine blades (See et al., 2002).

A high power Q-switched Nd:YAG laser with pulse duration of the order of 1 $\sim$ 100 ns is frequently used for laser shock peening, and the specimen is usually prepared with a thermo-protective absorbing coating with a transparent confining layer on top, to maximize the effect of the process (Fabbro et al., 1998; Montross et al., 2002). Despite significant improvements over the years, Fabbro et al. (1998)

indicated the potential for improving the process by adopting extremely short laser pulses to achieve higher pressure, and thus deeper processed layers.

Ultrashort laser pulses, or ultrafast lasers (UFL), of sub-picoseconds pulse duration have been investigated experimentally, primarily for material removal (Nolte et al., 1997; Dumitru et al., 2002; Pronko et al., 1995; Zhu et al., 1999). Liu et al. (1997) discuss laser-matter interaction involving femtosecond laser pulses in detail.

Femtosecond laser pulses are expected to be a good tool not only for material removal, but also for shock generation inside a metal, due to its extremely short pulse duration (Fabbro et al., 1998). This can be inferred from experimental demonstration of acoustic signal generation using short laser pulse durations between 100 fs and 150 ps (Dehoux et al., 2006).

There have been few investigations on laser shock peening using short pulses of the order of picosecond or femtosecond duration. Banaś et al. (1990) conducted an experiment using a pulse duration of 150 ps for laser shock peening of an uncoated steel in water confined configuration, and Chu et al. (1999) used a pulse duration of 600 ps for low carbon steel in vacuum. However, Kaspar and Luft (2001) indicated in their experiment using a pulse duration of 210 fs for molybdenum without a top coating that the shock affected depth for the femtosecond laser pulses is too shallow to make femtosecond pulses interesting for laser shock peening application, even though the femtosecond laser pulses deliver higher peak pressure than longer pulse duration lasers. They also indicated that optical breakdown of the transparent confining layer, water, may limit the possibility of valid laser shock peening with femtosecond laser pulses. This is discussed by Vogel et al. (2005) in greater detail. Thus, it can be summarized that the process of laser shock peening using sub-picosecond pulse duration needs further investigation.

In this study, the feasibility of laser shock peening of top coated steel in water confined configuration using ultrafast laser pulses is experimentally investigated. Optical breakdown of the transparent confining layer and selection of the top coating material are carefully considered to enhance the prospect of laser shock peening using ultrafast laser pulses.

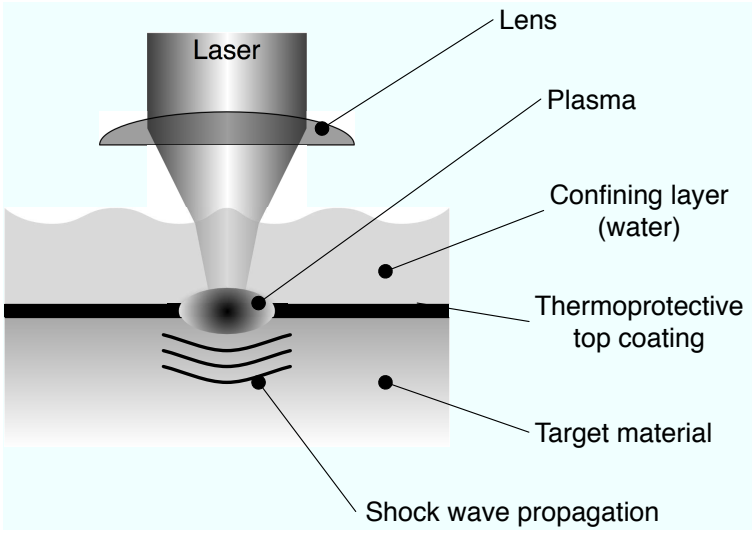

Fig. 4.1. A water confined configuration for laser shock peening

4.2 Background

The laser shock peening process is illustrated schematically in Fig. 4.1. As summarized by Fabbro et al. (1998) and Montross et al. (2002), a confining layer and top coating are used to maximize the laser induced pressure on the top surface of the target material.

One of the potential advantages of using UFL for LSP over long pulse duration laser is their ability to minimize thermal penetration depth (δ_s), which is related to the pulse duration (t_p) and thermal diffusivity (α) by $\delta_s \propto \sqrt{\alpha \cdot t_p}$ (Mills, 1992; Liu et al., 1997). In addition, a shorter pulse duration is expected to increase pressure (P) induced by the laser (Fabbro et al., 1998; Dehoux et al., 2006). Fabbro et al. (1998) presented a relation between pressure (P) induced by the laser and the depth (L_p) of the plastically deformed region, which can be expressed as

$$L_p \propto t_p \cdot P \quad \text{and} \quad P \propto \sqrt{I_0}$$

where t_p, I_0 and P are the pulse duration, beam intensity and pressure generated by the laser input, respectively. This indicates that a shorter pulse duration may result in a relatively thin shock peened layer. Hence, further investigation is needed to determine whether the laser induced pressure increment can compensate for the

Table 4.1. Thermal properties (Mills, 1992) of select materials

Material	Thermal diffusivity $[m^2/s \times 10^{-6}]$	Melting point [K]
Aluminum	97.1	933
Iron	20.7	1810
Lead	24.1	601
Magnesium	87.6	929
Zinc	41.8	693

decrement of the shock peened layer thickness when using an UFL for LSP.

Kaspar and Luft (2001) indicated very low feasibility of LSP using UFL, but they conducted their experiment without a top coating. The top coating is adopted in this study. Materials that are frequently used for the top coating are black paint and aluminum (Montross et al., 2002). For this study, zinc is selected for the top coating material since it has a lower thermal diffusivity than aluminum, Table 4.1, to maximize the thermal protective effect, and also since zinc is widely used as a coating for steel in industry. In addition, zinc is expected to provide useful information on the feasibility of laser microwelding for low melting point metals using UFL.

Another issue to be considered for LSP using UFL is related to the transparent confining layer (water layer in this study), Fig. 4.1. As discussed by Vogel et al. (2005), optical breakdown of water occurs at lower laser input fluence for shorter pulse duration due to multiphoton ionization. Chu et al. (1999) conducted their LSP experiment in a vacuum chamber to avoid optical breakdown. The confining layer is adopted in this study. The optical breakdown of water can be decreased by using a high numerical aperture focusing lens for UFL (Vogel et al., 2005).

The main objective of this study is to investigate the feasibility of laser shock peening (LSP) using ultrafast laser (UFL) pulses on a zinc coated steel specimen, galvanized steel, with water as the confining medium. A zinc alloyed steel, i.e., galvannealed steel is also used for comparison. Vickers microhardness is used to determine the extent of shock peening using UFL.

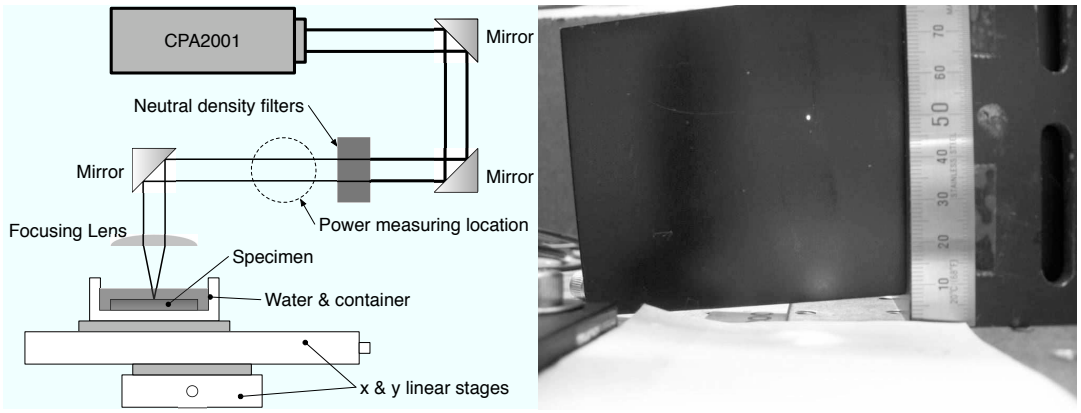

(a) (b)

Fig. 4.2. (a) Overall layout of experimental set-up (b) A focused UFL forming a visible spot in air

4.3 Experiment

The overall experimental set-up is shown in Fig. 4.2 (a). A Clark-MXR CPA-2001 laser was used in this experiment (λ = 775 nm, 0.8 mJ @ 1 kHz, $t_p \approx$ 200 fs). The beam is guided by mirrors to an aspheric focusing lens of high numerical aperture, NA $\approx$ 0.5. The lens is selected 1) to obtain a small focal diameter to minimize spherical aberration (Hecht, 2002), resulting in high input fluence (J) for a given laser beam power with better beam quality on the focal plane, and 2) to minimize optical breakdown of a confining water medium for a given laser fluence (Vogel et al., 2005). The lens is mounted on an one-axis linear stage to align the focal plane with the specimen top surface by observing a visible spot formed by the focused UFL, Fig. 4.2 (b).

Neutral density filters of optical density (OD) labeled as 0.5, 1.0 and 2.0 are used to control the laser power (and fluence). The actual OD values of the filters were measured by comparing the laser beam power obtained with or without the filters, and the values are used to evaluate corresponding fluences (J) with the filter using the relationship $J = 10^{-OD} \cdot J_0$, where J_0 is the fluence without the filters. The laser fluence J_0 was estimated from measured laser beam powers and a focal diameter estimated as follows: Actual average power of the laser beam (P) was measured using a power meter. The average power obtained for several measurements was 643.7 $\pm$

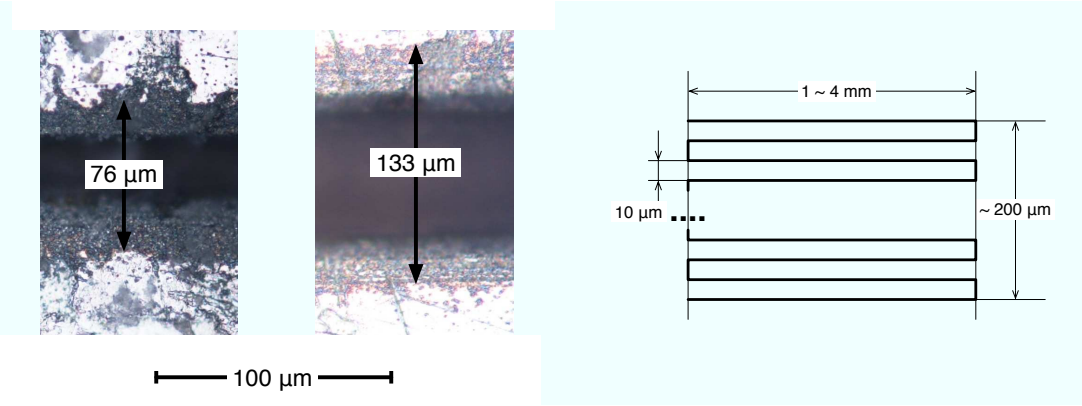

(a) (b)

Fig. 4.3. (a) Two examples of microscope photos for single line scanning on the top surface of galvanized steel specimen. (b) Scanning pattern on the top surface of a specimen.

5.8 mW. The width of the single line scan was measured from microscope photos, and taken as the focal diameter (d), Fig. 4.3 (a). The focal diameter was estimated to be 122.8 $\pm$ 15.7 μm. Thus, the input fluence J_0 is obtained as 5.43 J/cm^2, from $J_0 = P/(0.25\pi d^2 \cdot \phi)$, where ϕ is the repetition rate of the laser pulse. At this point, it should be noted that the width of the scanned line in the figure does not exactly represent the focal diameter, but is strongly related to the diameter and input fluence. Thus the fluence value is not absolute, but rather a relative measurement. Moreover, the focal diameter is strongly dependent on the distance between the target top surface and focusing lens, especially for high NA focusing lens. This may increase uncertainty in fluence values in this experiment. These values were used in estimating the fluence and the results are summarized in Table 4.2. It should be noted that the fluence estimation does not consider any uncertainty for the beam delivery system and the confining configuration for laser shock peening, for example, reflection loss of mirrors and absorption of the confining water.

The water layer thickness was 2 mm, and was controlled using an injection needle. The specimen was mounted in the water container, which was installed on a two-axes computer-controlled linear stage. The specimens were processed on the top surface with each scan line being 4 mm in length, and spaced apart by 10 μm pitch, Fig. 4.3 (b).

Table 4.2. Labeled and measured optical densities (OD) of neutral density filters and corresponding fluences calculated from $J = 10^{-OD} \cdot J_0$, where $J_0 = 5.43$ J/cm^2

OD, labeled	OD, measured	Fluence [J/cm^2]
0.5	0.50	1.73
1.0	0.99	0.21
2.0	1.78	0.09

Table 4.3. Chemical composition (wt%) of an AKDQ steel (Zhang and Senkara, 2006)

C	Mn	P	S	Si	Cu	Ni	Cr	Mo	Sn	Al	Ti
0.035	0.210	0.006	0.011	0.007	0.020	0.009	0.033	0.006	0.004	0.037	0.001

The specimens were as-received 1 mm thick galvanized and galvannealed AKDQ steel sheets, Table 4.3 (Zhang and Senkara, 2006). The galvanized steel was the main material for the LSP experiment, considering the zinc coating of the steel as the top metallic ablative coating for laser shock peening. The thickness of the zinc coating on galvanized steel was measured from a cross-section, Fig. 4.4, of the specimen and ranged from 16.0 to 39.3 μm, with an average value of 26.9 μm. The galvannealed steel was used for a comparison study on the effect of the metallic coating.

For the galvanized steel, a full factorial experimental design was used with two factors of laser input fluence (J) and feed rate (f), with four levels for the input fluence (three fluences with, and one without the filters) and two levels for feed rate,

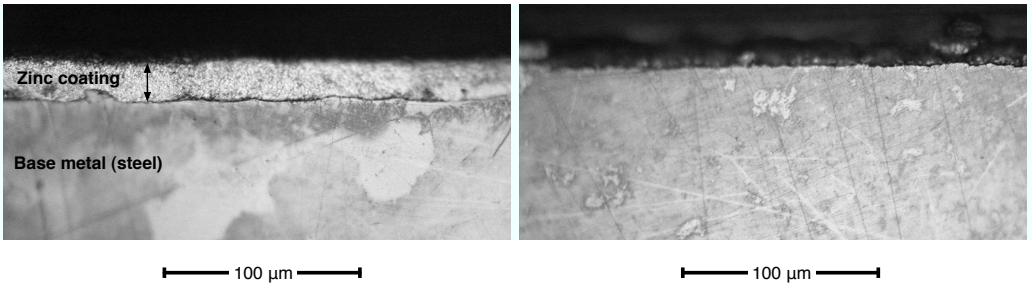

(a) (b)

Fig. 4.4. Sections of (a) galvanized, and (b) galvannealed steel specimens. Specimens were sectioned, cold mounted, polished and etched using 0.5% nitol (Vander Voort, 2004).

500 and 1000 μm/s. A slow feed rate of 50 μm/s was separately investigated. For the galvannealed steel, a fixed feed rate of 500 μm/s was used. After the experiments, the top surface Vickers microhardness values of the specimen were measured using Buehler's Micromet II. The microhardness values for galvanized and galvannealed steel specimens on the top surfaces before the experiment were found to be 69.5 $\pm$ 4.0 and 121.5 $\pm$ 2.4 Hv, respectively. The microhardness of base low carbon steel was found to be 97.6 $\pm$ 1.8 Hv. The uncertainty of measurement was determined with a 99% confidence level. After processing, the microhardness of each specimen was measured 10 times. The microscope was used for visual inspection of the top surface, and for estimating the maximum depth of the processed region using a 40X objective lens which has a shallow depth of focus, thus providing high spatial resolution.

4.4 Results and discussion

The effect of input fluence and feed rate on microhardness of galvanized steel specimens is examined first, Fig. 4.5 (a). For $f = 500$ μm/s, the microhardness is observed to increase abruptly between 0.09 and 0.21 J/cm^2 fluence, and level off at 106.7 $\pm$ 8.2 Hv, as fluence increases above 0.21 J/cm^2. The level off value was statistically determined from mean difference tests with 1% significance level (Montgomery, 1991) on microhardness values for $J = 0.21$, 1.73 and 5.43 J/cm^2. For $f = 1000$ μm/s, the level off is observed at 95.5 $\pm$ 6.0 Hv, but only for J = 1.73 and 5.43 J/cm^2. However, it is not clear whether $f = 500$ μm/s results in higher microhardness than $f = 1000$ μm/s since those level off values are within the uncertainty range of each other. The mean difference test also indicates that there is no significant difference between the level off hardness for $f = 500$ and 1000 μm/s. The uncertainty is mainly due to the surface roughness of the LSP regions, and different hardness values for the various iron-zinc intermetallic phases that may form (Korb and Olson, 1987). However, it is interesting to note that the level off value for $f = 1000$ μm/s is very close to the original value of the base steel, 97.6 $\pm$ 1.8 Hv. Considering the fluence values of J2 = 0.21 and J3 = 1.73 J/cm^2 for galvanized steel, Fig. 4.10 (a), and the observation that

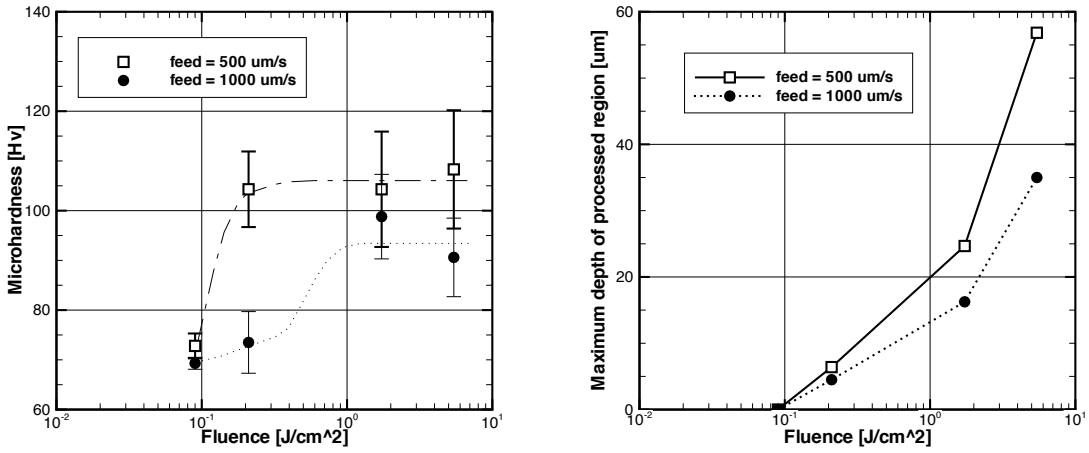

(a) (b)

Fig. 4.5. Experimental data comparison of galvanized steel specimens for select feed rates, $f = 500$ and 1000 μm/s, with respect to input fluence: (a) Microhardness. (b) Maximum depth of the processed region. In the figure, "um" represents μm.

the microhardness levels off for $J \geq 0.21$ J/cm^2, Fig. 4.5 (a), it can be deduced that the bright top surface is due to a thin zinc layer until complete zinc removal occurs when $J \geq 5.43$ J/cm^2. Material removal occurs mainly for zinc when $0.09 \leq J < 1.73$ J/cm^2; then for steel when $J \geq 1.73$ J/cm^2. Thus the microhardness increment is mainly due to removal of the soft top coating.

Figure 4.5 (b) shows the corresponding maximum depth of the processed region. The maximum depth is observed to be more than the zinc layer thickness (26.9 μm average) for high fluence when $f = 500$ μm/s. It is interesting to note from the figure that the maximum depth for galvanized steel, which has zinc coating on top of steel, follows the trend of two logarithmic dependency with respect to the input fluence, as discussed by Nolte et al. (1997). The microhardness for $f = 50$ μm/s could not be measured for high fluence due to the formation of a severe groove, Fig. 4.6, but was measured for low fluence. However, the microhardness for $f = 50$ μm/s with the low fluence was not significantly different from the value for $f = 500$ μm/s. It should be noted that debris generation was observed for $f = 50$ μm/s, Fig. 4.7 (b), which became more severe as feed rate decreased and fluence increased. The debris

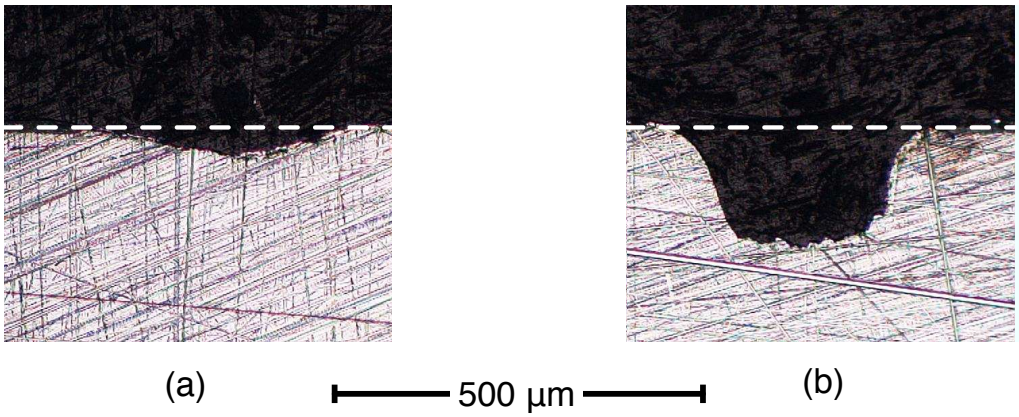

Fig. 4.6. Section of galvanized steel specimen after LSP with $J = 5.43$ J/cm^2 for feed rate of (a) 500 μm/s and (b) 50 μm/s

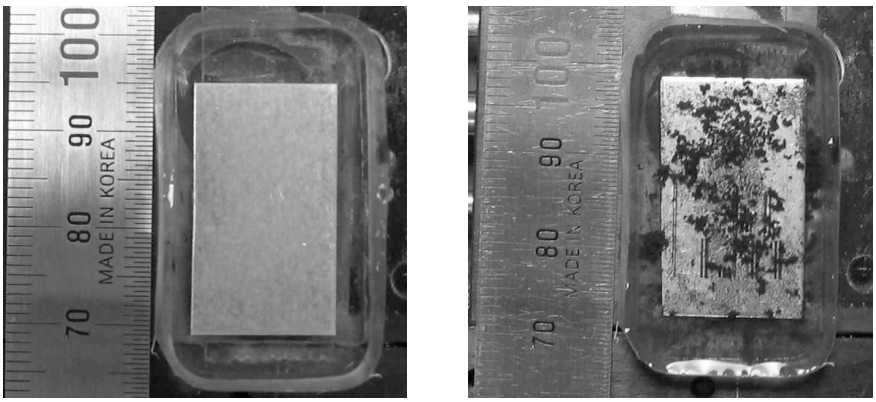

(a) (b)

Fig. 4.7. Debris generated during galvanized steel experiment: (a) Before and (b) after the experiment

generation is one possible reason for the microhardness leveling off at the high fluence. To minimize the debris interference, the water in the container was replaced after each run. But this did not completely eliminate debris interference during an experimental run. Such debris generation, however, was not observed during experiments with the galvannealed steel specimen. Another possible reason for the level off is optical breakdown of water. Vogel et al. (2005) state that optical breakdown of water occurs for fluence higher than 5.6 J/cm^2 by femtosecond laser pulses (pulse duration = 100 fs, wavelength = 800 nm) focused using a lens of NA = 0.65. The level off was observed for fluence higher than 0.21 J/cm^2 with NA $\approx$ 0.5 in this study. Even though the level

Table 4.4. ANOVA table of data for galvanized steel. In the table, "DoF" stands for degree of freedom. "F_{crit}" is the critical F ratio for a given degree of freedom. Levels for the factors J and f are 0.09, 0.21, 1.73 and 5.43 J/cm^2, and 500 and 1000 μm/s, respectively.

Source of variation	DoF	Sum of Squares	Mean Squares	F	F_{crit}	p-value
Fluence, J	3	150181	50060	215.3	3.8	$p \ll 1.0 \times 10^{-13}$
Feed rate, f	1	10833	10833	46.6	6.7	1.6×10^{-11}
Interaction, $J \times f$	3	14406	4802	20.7	3.8	5.8×10^{-13}
Error	934	217139	232	–	–	–
Total	941	392558	–	–	–	–

off fluence is lower than the threshold fluence, the possibility of optical breakdown for J $\geq$ 0.21 J/cm^2 cannot be completely ruled out due to the lower NA used in this study, and uncertainty of the focal diameter estimation, i.e., the focal diameter from line scans, Fig 4.3 (b), might be an overestimation. The optical breakdown of water was not experimentally investigated in this study. However, it is interesting to note that the microhardness did not change drastically for high fluence, Fig. 4.5 (a), while material removal occurred significantly for the fluence, Fig. 4.5 (b). This indicates that the femtosecond laser is a good tool for material removal for the conditions used in this experiment.

Table 4.4 summarizes ANOVA results (Montgomery, 1991) of microhardness values obtained from galvanized steel experiments with factors J (four levels - 0.09, 0.21, 1.73 and 5.43 J/cm^2) and f (two levels - 500 and 1000 μm/s). For the levels studied, the large F ratio for J in Table 4.4 indicates that the fluence has the dominant effect on microhardness. The feed rate (f) and interaction effects on the microhardness is relatively small. The small effect of feed rate may be due to the fact that the number of shots is related to both feed rate and scanning line distance, 10 μm, Fig. 4.3 (b), which was kept constant in this experiment. It should also be noted that Duncan's post test (Montgomery, 1991) on microhardness indicates that all the fluences, except the lowest ones, result in the same microhardness, which confirms the previous observation from mean difference tests, and from Fig. 4.5 (a).

Next, the effect of top coating on microhardness is examined by comparing the hardness of processed galvanized and galvannealed steel specimen, Fig. 4.8 (a). In

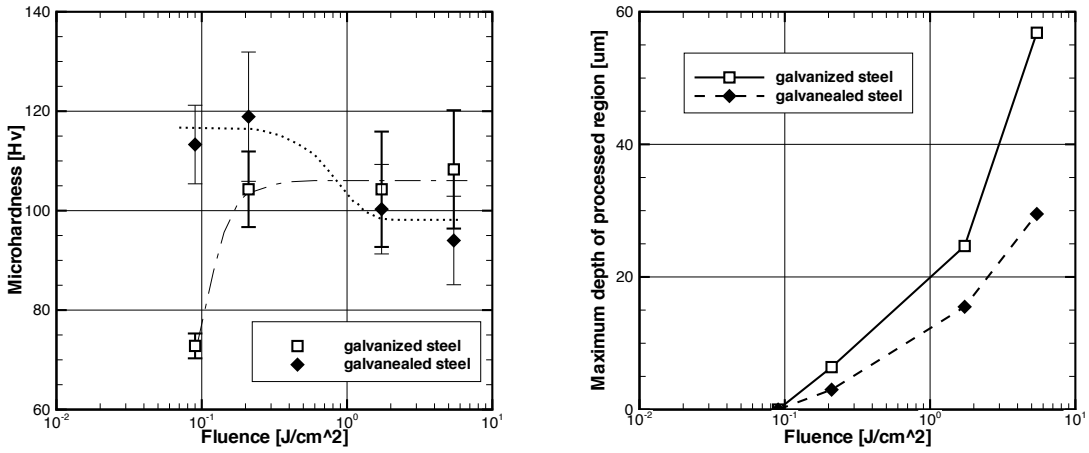

(a) (b)

Fig. 4.8. Experimental data comparison of galvanized and galvannealed steel specimens for feed rate $f = 500$ μm/s, with respect to input fluence: (a) Microhardness. (b) Maximum depth of the processed region. In the figure, "um" represents μm.

the figure, the galvanized steel results for $f = 500$ μm/s of Fig. 4.5 is re-plotted for comparison. The microhardness of galvannealed steel is observed to decrease slightly as fluence increases, which is a different behavior from galvanized steel. It also shows less significant dependence of the hardness on fluence than galvanized steel. Mean difference tests with 1% significance level was conducted on microhardness values for $J = 1.73$ and 5.43 J/cm^2 of galvannealed steel specimen, and resulted in the same values of 97.2 $\pm$ 6.1 Hv. The test was also conduced for $J = 1.73$ J/cm^2 on both materials, and indicated that there is no difference in the values. But the test for $J = 5.43$ J/cm^2 of both materials resulted in higher microhardness for galvanized steel than for galvannealed steel. However, from the uncertainties in microhardness values, it is difficult to conclude whether the results are significantly different. The maximum depth of processed region for galvannealed steel also shows the two logarithmic dependency (Nolte et al., 1997), Fig. 4.8 (b), but a shallower depth than galvanized steel. The depth difference for the two materials is due to the fact that one has zinc as an alloy, while the other has it as a coating, resulting in different absorption characteristics.

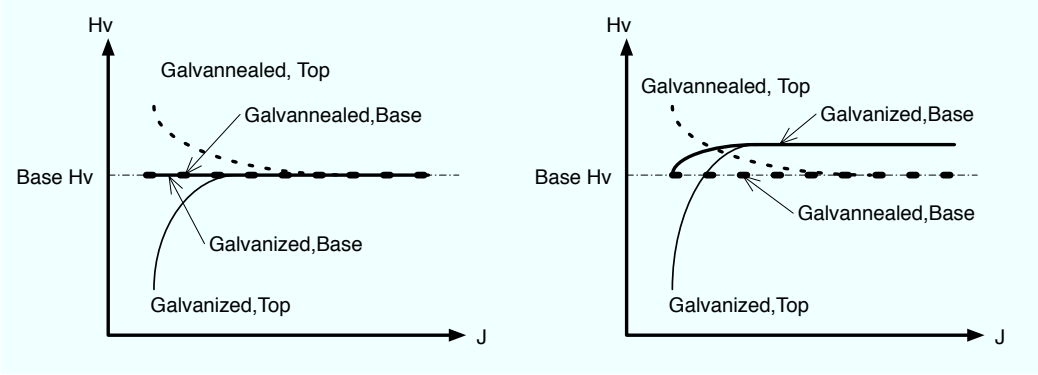

(a) (b)

Fig. 4.9. Two possibilities on a relation between UFL input fluence and hardness at top surface of base material: (a) no change in hardness, and (b) hardening effect. In the figure, "Hv" and "J" represent the microhardness and input fluence, respectively.

Even though the microhardness increment for the galvanized steel has been attributed mainly to the removal of zinc, Fig. 4.5, this does not completely exclude the feasibility of LSP with UFL. The microhardness of the base metal of both galvanized and galvannealed steel used in this experiment was measured to be 97.6 ± 1.8 Hv. The microhardness after LSP was observed to level off at 106.7 ± 8.2 and 97.2 ± 6.1 Hv for galvanized and galvannealed steel, respectively, when high fluence was used with $f = 500$ μm/s. At the higher feed rate of $f = 1000$ μm/s, the microhardness leveled off at 95.5 ± 6.0 Hv for galvanized steel, high fluence. Based on these observations, it can be deduced that the base metal may experience no softening or hardening during the process, Fig. 4.9 (a), since the hardness values after LSP are not significantly different from the original value, considering the uncertainty. This may be an advantage when the UFL is used as a tool for material removal. Depending on the conditions used, some hardening may occur due to LSP using UFL for galvanized specimens, Fig. 4.9 (b), noting that the microhardness value of galvanized specimen is slightly higher than of galvannealed specimen, even within the uncertainties of each other, which are 106.7 ± 8.2 and 97.2 ± 6.1 Hv, respectively. However, for high feed rate and fluence, the hardness (95.5 ± 6.0 Hv) is still expected to be unchanged from the original value, 97.6 ± 1.8 Hv. Thus, LSP using UFL may be feasible, depending on the selection of processing parameters. In this case, the hardness for the low feed

Table 4.5. Hardness increment for laser peening processes on steels. The estimated increment for this study is also listed

type of processed steel	pulse duration	hardness increment [%]	source
high carbon	10 ns	40.9	Yakimets et al. (2004)
low carbon	10 ns	59.1	Peyre et al. (2000)
low carbon	600 ps	37.1	Chu et al. (1999)
low carbon	200 fs	9.3	this study

rate and high fluence increases from 97.6 to 106.7 Hv, about a 9 % maximum increase for low carbon steel. The minima is 0 % for the scenario shown in Fig. 4.9 (a). Results reported in the literature range between 37 and 60 % for low carbon steel using longer pulse duration beams, Table. 4.5. Hence, only limited hardening effect can be expected when using UFL, and thus may not be effective for the setup used in this experiment.

The UFL used in this study demonstrates good performance for material removal, Figs. 4.5 and 4.8, since it has minimal effect on the base material hardness. However, LSP using the UFL needs further investigation. It is known that the depth of the shock peened region increases with the focal diameter since the stress wave is more planar inside the target (Fabbro et al., 1998), and that a focal diameter of the order of a millimeter is frequently used for effective LSP (Montross et al., 2002). However, the focal diameter used in this study was estimated as approximately 120 μm, which is just 10 % of the conventional value. Increasing the focal diameter to the large value for a fluence of $0.09 \leq J \leq 0.21$ J/cm^2 requires more than twice the power level of the current system. An alternate approach is to use a microlens array, which is expected to produce an effect equivalent to a large single focal point. If a single focusing lens is used, a NA greater than 0.5 may be helpful for a more feasible LSP using UFL, which is expected to decrease optical breakdown of water, and thus increase the laser power transmitted to the specimen. As discussed previously in Fig. 4.9 (b), feed rates much lower than 500 μm/s may result in more feasible LSP using UFL. At this point, it should be noted that the lowest feed rate of 50 μm/s used in this study resulted in severe debris generation and no significantly different hardness for the low fluence.

Flowing water may thus be used to remove any debris formed. However, it is not clear whether such modifications will enhance the potential for LSP using UFL more than using a longer pulse duration, Table. 4.5.

Finally, the processed area for different specimen were compared using photomicrographs, Fig. 4.10. Figure 4.10 (a) shows that galvanized steel exhibits significant variation in appearance as fluence increases, from a bright and reflective surface to a dark surface. This may be due to different amounts of zinc being removed. The bright surface is considered to be zinc that remained on top of the base material after the process, due to the low fluence. Consequently, the dark surface is expected to be the base material, steel. The reflective surface may also result from resolidification of molten zinc that remains on top of the base metal, due to confinement of evaporated or plasma zinc by water. In other words, the figure may imply the possibility of laser microwelding, especially for low melting point metals such as zinc and lead. Note that most of the zinc is removed at high fluence, Figs. 4.5 (b) and 4.10 (a). Thus the laser power used in this study is more than adequate for laser microwelding of low melting point metals. However, a pulse repetition rate greater than 1 kHz may be needed to produce deeper penetration. On the other hand, no significant appearance change with respect to input fluence was observed for galvannealed steel, Fig. 4.10 (b).

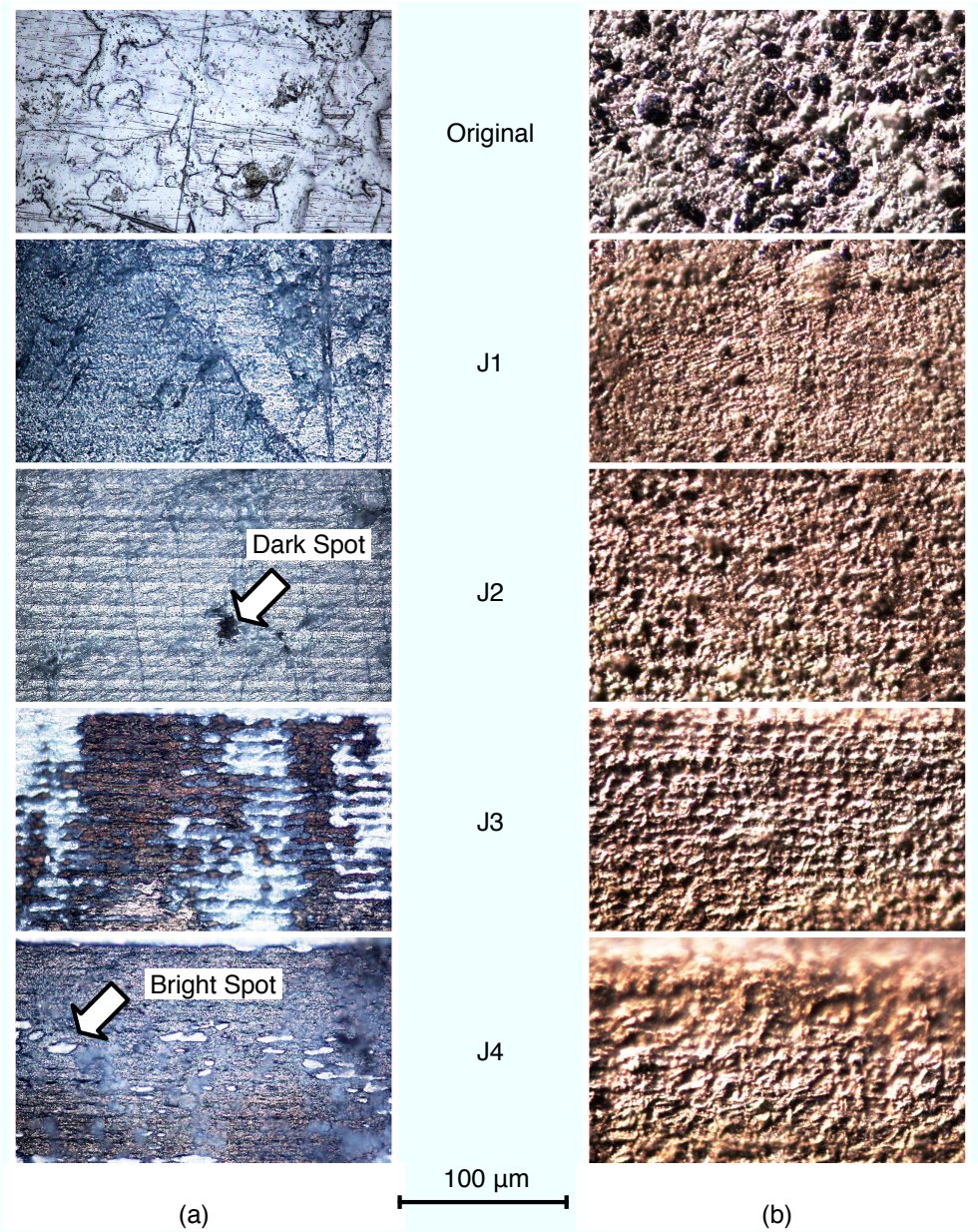

Fig. 4.10. Top surface of shock peened specimens for select fluences for (a) galvanized, and (b) galvannealed steel: In the figure, J1 = 0.09, J2 = 0.21, J3 = 1.73 and J4 = 5.43 J/cm^2. "Original" indicates top surfaces without LSP.

4.5 Summary

The feasibility of laser shock peening using femtosecond laser pulses is experimentally investigated for galvanized steel with a water layer above it. The results indicate that fluence has significant effect on microhardness of galvanized steel measured on the top surface. A comparison between the galvanized and galvannealed steel results shows that the hardness measured on the top surface is mainly due to removal of the top coating. Improvement in microhardness of base steel obtained after laser shock peening with ultrafast laser pulses were slight, compared to results for long pulse lasers in the literature. This indicates that the femtosecond laser is good for material removal, but may not be a good tool for laser shock peening for the conditions used in this study. The results do not completely exclude the potential for improving laser shock peening using femtosecond laser pulses. Optimization of process parameters, including feed rate, may improve laser shock peening using femtosecond laser pulses. However, it is questionable whether such parameter optimization for laser shock peening with femtosecond pulse duration may produce feasible results without increasing the pulse duration.

Chapter V

Conclusions and Future work

The feasibility of laser microwelding and laser shock peening using femtosecond laser pulses is examined numerically and experimentally.

In Chapter 2, the two-temperature model numerical analysis framework is implemented using a general-purpose commercial FEM package, ABAQUS. The framework is validated by comparison with analytical solutions of the linear TTM and also by experimental results. Nonlinear simulations for low and high fluences are also validated using data from the literature. Thus the TTM can generally be analyzed numerically using ABAQUS. For the conditions used, the TTM implementation illustrates the effectiveness of material removal with UFL. The FEM results indicate that the maximum molten pool depth is obtained near the ablation threshold. The analysis depicts that a feasible thickness scale for laser microwelding using UFL is of the order of 10^2 nm. The FEM results also suggest that a pulse repetition rate of the order of 1 GHz will enable thermal interaction between pulses inside a metal, resulting in a reasonably deep molten pool.

In Chapter 3, the feasibility of laser microwelding using femtosecond laser pulses is numerically investigated for select parameters of pulse repetition rate, pulse duration, and focal radius, using the two-temperature model implementation in ABAQUS. The material model from Chapter 2 is improved. The validity of the improved model is investigated by comparison with experimental results from the literature, and both models of Chapters 2 and 3 show similar trend in relation to molten pool generation. For the conditions examined, the results indicate that laser microwelding is feasible for 1) low fluence ultrashort pulses with high repetition rates in the range of $0.1 \sim 10$

GHz, 2) longer pulses from a stable laser generator with high fluence capability, or 3) larger focal radius for a given fluence i.e., high energy per pulse and fluence. On the other hand, the results indicate that lower repetition rate, shorter pulse duration, and smaller focal radius for a given fluence provide favorable conditions for precise material removal such as laser cutting or drilling, as those conditions maximize ablation, and minimize molten pool generation.

In Chapter 4, the feasibility of laser shock peening with femtosecond laser pulses is experimentally investigated for galvanized steel in water confined configuration. The results indicate that fluence has significant effect on microhardness of galvanized steel. A comparison of the results of galvanized and galvannealed steels illustrates the hardening effect of the top coating, since galvannealed steel becomes softer after shock peening. Improvement in microhardness obtained after laser shock peening with ultrafast laser pulses was slight, compared to results in the literature. However, it demonstrates the potential for improving laser shock peening using ultrafast laser pulses, if the process parameters are optimized.

The results of this study indicate that the femtosecond laser pulse is a good tool for material removal. They also show that there should be modification on the system for applications, such as laser microwelding and laser shock peening. Based on the results, future work is proposed as follows:

The ABAQUS implementation for the two temperature model in this study can be improved for more precise results by adding a model for molten metal flow, and also by considering material deposition.

Pulse repetition rate is one of the key parameters to obtaining enough molten pool in metals for laser welding using short duration laser pulses. Currently, available chirped pulse amplification femtosecond laser pulses provide abundantly high power, but too low a pulse repetition rate, of the order of 1 kHz, for laser microwelding. On the other hand, non-chirped pulse amplification lasers provide higher repetition rate but lower power per pulse than the chirped pulse amplification femtosecond lasers. With this limitation, low melting point metals may be investigated for a feasibility study of laser microwelding using femtosecond laser pulse duration. In addition, it will

be interesting to investigate the effect of pulse duration of the order of picoseconds.

Laser shock peening using femtosecond laser pulses may require a careful approach. In the relation, $L_p = t_p \cdot P$, where L_p is the depth of the plastically deformed region, the laser pressure (P) induced by femtosecond laser pulses may be too low to compensate for the short pulse duration (t_p), especially for the conditions considered in this study. The specimen condition may be improved by using black dielectric pigment top coating of thickness of the order of 10 μm. Flowing water confining layer is expected to increase the chance of obtaining feasible laser shock peening results. To confirm the relation of the depth, pulse duration and the laser induced pressure, it will be necessary to compare laser shock peening results of picosecond or nanosecond laser pulses with femtosecond laser pulses.

Appendices

Appendix A

Derivation of the energy term updating equation

The effective volumetric electron internal energy is defined as:

$$U_{e,eff}(T_e, T_l, x, t) \equiv U_e + E - S$$

where T_e, T_l, x and t in parenthesis indicate that those are independent parameters for $U_{e,eff}$. Then, the total derivative, $dU_{e,eff}$, can be written as follows:

$$dU_{e,eff} = \frac{\partial U_{e,eff}}{\partial T_e} dT_e + \frac{\partial U_{e,eff}}{\partial T_l} dT_l + \frac{\partial U_{e,eff}}{\partial x} dx + \frac{\partial U_{e,eff}}{\partial t} dt \tag{A.1}$$

The first partial derivative term on the right hand side of Eq. (A.1) can be written as:

$$\frac{\partial U_{e,eff}}{\partial T_e} = \frac{\partial (U_e + E - S)}{\partial T_e} = \frac{\partial U_e}{\partial T_e} + \frac{\partial E}{\partial T_e} - \frac{\partial S}{\partial T_e}$$

At this point, it must be noted that $\dot{E}$ and $\dot{S}$ are known, but E and S are *unknown*. Thus, with chain rule, the equation can be rewritten as:

$$\frac{\partial U_{e,eff}}{\partial T_e} = \frac{\partial U_e}{\partial T_e} + \left(\frac{\partial t}{\partial T_e} \cdot \frac{\partial E}{\partial t} \right) - \left(\frac{\partial t}{\partial T_e} \cdot \frac{\partial S}{\partial t} \right) = \frac{\partial U_e}{\partial T_e} + \frac{\partial t}{\partial T_e} \cdot \dot{E} - \frac{\partial t}{\partial T_e} \cdot \dot{S}$$

For the above equation, it should also be noticed that both t and T_e are *independent* parameters for $U_{e,eff}$, i.e. $\partial t / \partial T_e = 0$. Hence, we have

$$\frac{\partial U_{e,eff}}{\partial T_e} = \frac{\partial U_e}{\partial T_e} + \cancelto{0}{\frac{\partial t}{\partial T_e}} \cdot \dot{E} - \cancelto{0}{\frac{\partial t}{\partial T_e}} \cdot \dot{S} = \frac{\partial U_e}{\partial T_e} \tag{A.2}$$

In similar manner, noting that U_e is only T_e dependent by definition, other derivatives can also be evaluated as follows:

$$\frac{\partial U_{e,eff}}{\partial T_l} = \cancelto{0}{\frac{\partial U_e}{\partial T_l}} + \cancelto{0}{\frac{\partial t}{\partial T_l}} \cdot \dot{E} - \cancelto{0}{\frac{\partial t}{\partial T_l}} \cdot \dot{S} = 0 \tag{A.3}$$

$$\frac{\partial U_{e,eff}}{\partial x} = \cancelto{0}{\frac{\partial U_e}{\partial x}} + \cancelto{0}{\frac{\partial t}{\partial x}} \cdot \dot{E} - \cancelto{0}{\frac{\partial t}{\partial x}} \cdot \dot{S} = 0 \tag{A.4}$$

$$\frac{\partial U_{e,eff}}{\partial t} = \cancelto{0}{\frac{\partial U_e}{\partial t}} + \cancelto{1}{\frac{\partial t}{\partial t}} \cdot \dot{E} - \cancelto{1}{\frac{\partial t}{\partial t}} \cdot \dot{S} = \dot{E} - \dot{S} \tag{A.5}$$

By plugging equations from (A.2) to (A.5) into Eq. (A.1), we have

$$dU_{e,eff} = \frac{\partial U_e}{\partial T_e} dT_e + \left(\dot{E} - \dot{S}\right) \cdot dt$$

or, in discretized form,

$$\Delta U_{e,eff} = \frac{\partial U_e}{\partial T_e} \Delta T_e + \left(\dot{E} - \dot{S}\right) \cdot \Delta t$$

Appendix B

Derivation of the heat flux term updating equation

To obtain the update relation for $\partial\vec{q}/\partial T$, Eq. (3.3) can be partially differentiated with respect to T_e as follow:

$$\frac{\partial}{\partial T_e}\left(\tau_e\frac{\partial q_{e,x}}{\partial t}+q_{e,x}\right)=\frac{\partial}{\partial T_e}\left(-k_e\cdot\frac{\partial T_e}{\partial x}\right)$$

Noting that k_e and τ_e can be explicitly expressed in terms of T_e, for example Eqs. (2.5) and (3.6) respectively, we have

$$\frac{\partial\tau_e}{\partial T_e}\frac{\partial q_{e,x}}{\partial t}+\tau_e\frac{\partial}{\partial T_e}\left(\frac{\partial q_{e,x}}{\partial t}\right)+\frac{\partial q_{e,x}}{\partial T_e}=-\frac{\partial k_e}{\partial T_e}\frac{\partial T_e}{\partial x}-k_e\frac{\partial}{\partial T_e}\left(\frac{\partial T_e}{\partial x}\right)$$

It is clear that the second term on the right side can be eliminated as follow:

$$k_e\frac{\partial}{\partial T_e}\left(\frac{\partial T_e}{\partial x}\right)=k_e\frac{\partial}{\partial x}\left(\frac{\partial T_e}{\partial T_e}\right)=k_e\frac{\partial}{\partial x}\left(\frac{\partial T_e}{\cancel{\partial T_e}}\right)^{1}=0$$

Hence, by rearrangement and defining $\partial q_{e,x}/\partial T_e\equiv\Psi$, we have a discretized equation as

$$\tau_e\frac{\Psi^{t+\Delta t}-\Psi^t}{\Delta t}+\Psi^{t+\Delta t}=-\left(\frac{\partial k_e}{\partial T_e}\frac{\partial T_e}{\partial x}+\frac{\partial\tau_e}{\partial T_e}\frac{\partial q_{e,x}}{\partial t}\right)$$

By rearrangement and discretizing the $\partial q_{e,x}/\partial t$ term,

$$\Psi^{t+\Delta t}=\frac{1}{\tau_e+\Delta t}\cdot\left(\tau_e\cdot\Psi^t-\frac{\partial\tau_e}{\partial T_e}\cdot\left(q_{e,x}^{t+\Delta t}-q_{e,x}^t\right)-\Delta t\cdot\frac{\partial k_e}{\partial T_e}\frac{\partial T_e}{\partial x}\right)\tag{B.1}$$

Noting that $q_{e,x}^t$ is *known* to the user subroutine, if Eq. (2.15) is substituted into Eq. (B.1), we obtain

$$\Psi^{t+\Delta t}=\frac{1}{\tau_e+\Delta t}\cdot\left(\tau_e\cdot\Psi^t+\frac{\partial\tau_e}{\partial T_e}\frac{\Delta t}{\tau_e+\Delta t}\left(q_{e,x}^t+k_e\frac{\partial T_e}{\partial x}\right)-\Delta t\cdot\frac{\partial k_e}{\partial T_e}\cdot\frac{\partial T_e}{\partial x}\right)\tag{B.2}$$

It is clear that Eq. (B.2) is identical to Eq. (2.16) if $(\partial q/\partial T)^t_{e,x}$ replaces Ψ^t.

Similarly, for $\partial\vec{q}/\partial(\nabla T)$, Eq. (2.4) can be partially differentiated with respect to $\partial T_e/\partial x$ as follow:

$$\frac{\partial}{\partial(\partial T_e/\partial x)}\left(\tau_e\frac{\partial q_{e,x}}{\partial t}+q_{e,x}\right)=\frac{\partial}{\partial(\partial T_e/\partial x)}\left(-k_e\cdot\frac{\partial T_e}{\partial x}\right)$$

Assuming that k_e and τ_e are independent of temperature gradient, it can be written as

$$\tau_e\cdot\frac{\partial}{\partial(\partial T_e/\partial x)}\left(\frac{\partial q_{e,x}}{\partial t}\right)+\frac{\partial q_{e,x}}{\partial(\partial T_e/\partial x)}=-k_e\cdot\frac{\partial(\partial T_e/\partial x)}{\partial(\partial T_e/\partial x)}$$

By rearrangement and defining $\partial q_{e,x}/\partial(\partial T_e/\partial x)\equiv\Xi$, we have

$$\tau_e\cdot\frac{\partial\Xi}{\partial t}+\Xi=-k_e$$

which can be discretized as

$$\tau_e\cdot\frac{\Xi^{t+\Delta t}-\Xi^t}{\Delta t}+\Xi^{t+\Delta t}=-k_e$$

and can be rearranged as

$$\Xi^{t+\Delta t}=\frac{1}{\tau_e+\Delta t}\cdot\left(\tau_e\cdot\Xi^t-\Delta t\cdot k_e\right) \tag{B.3}$$

Again, it is clear that Eq. (B.3) is identical to Eq. (2.17) if $(\partial q/\partial(\nabla T))^t_{e,x}$ replaces Ξ^t.

Appendix C

Source codes of ABAQUS user subroutines

The user subroutine UMATHT codes equations from Eq. (2.12) to Eq. (2.17). In the subroutine, the variables "ztp", "zfln", "zrfl" and "zskd" in lines 13 $\sim$ 16 define pulse duration in ps, input fluence in J/cm^2, reflectivity, and the skin depth in nm, respectively. The source code is listed as follows:

```
1         SUBROUTINE UMATHT(U,DUDT,DUDG,FLUX,DFDT,DFDG,STATEV,TEMP,
2        $        DTEMP,DTEMDX,TIME,DTIME,PREDEF,DPRED,CMNAME,NTGRD,NSTATV,
3        $        PROPS,NPROPS,COORDS,PNEWDT,NOEL,NPT,LAYER,KSPT,KSTEP,KINC)
4   C
5         INCLUDE 'ABA_PARAM.INC'
6   C
7         CHARACTER*80 CMNAME
8   C
9         DIMENSION DUDG(NTGRD),FLUX(NTGRD),DFDT(NTGRD),
10       $        DFDG(NTGRD,NTGRD),STATEV(NSTATV),DTEMDX(NTGRD),TIME(2),
11       $        PREDEF(1),DPRED(1),PROPS(NPROPS),COORDS(3)
12  C
13        ztp = 0.5
14        zfln = 0.400
15        zrfl = 0.332
16        zskd = 14.5
17  C
18        cond = STATEV(1)
19        dkdtemp = STATEV(2)
20        specht = STATEV(3)
21        edot = STATEV(4)
22        taue = STATEV(5)
23        dtaue = STATEV(6)
24  C
25        DUDT = specht
26        taud = DTIME + taue
27  C
```

```
28          if (CMNAME(1:4) .eq. 'MATE') then
29  c
30              tt = TIME(2) + DTIME
31              xx = COORDS(1)
32              zpp = (1-zrfl) * (zfln * (1.0e7)) / ztp
33              sdot = zpp * stg(tt,ztp) * sxe(xx, zskd)
34  c
35              du = DUDT*DTEMP + (edot - sdot)*DTIME
36              U = U + du
37  c
38               do i=1, NTGRD
39                FLUX(i) = (FLUX(i)*taue-DTIME*cond*DTEMDX(i))/taud
40                DFDG(i,i) = (DFDG(i,i)*taue-DTIME*cond)/taud
41                DFDT(i) =(DFDT(i)*taue
42       #                  +dtaue*(DTIME/taud)*(cond*DTEMDX(i)+FLUX(i))
43       #                  -DTIME*dkdtemp*DTEMDX(i))/taud
44               end do
45  c
46             else
47  c
48              du = DUDT*DTEMP - edot*DTIME
49              U = U + du
50  c
51              do i=1, NTGRD
52               FLUX(i) = -cond*DTEMDX(i)
53               DFDG(i,i) = -cond
54              end do
55             end if
56  c
57          RETURN
58          END
```

The user subroutine USDFLD codes material properties and temperature information sharing, Fig. 2.2 (a). These are defined in lines 13 and 14:

```
1           SUBROUTINE USDFLD(FIELD,STATEV,PNEWDT,DIRECT,T,CELENT,
2          1 TIME,DTIME,CMNAME,ORNAME,NFIELD,NSTATV,NOEL,NPT,LAYER,
3          2 KSPT,KSTEP,KINC,NDI,NSHR,COORD,JMAC,JMATYP,MATLAYO,LACCFLA)
4   c
5           INCLUDE 'ABA_PARAM.INC'
6   c
7           CHARACTER*80 CMNAME,ORNAME
8           CHARACTER*3 FLGRAY(15)
9           DIMENSION FIELD(NFIELD),STATEV(NSTATV),DIRECT(3,3),
10         1 T(3,3),TIME(2)
11          DIMENSION ARRAY(15),JARRAY(15),JMAC(*),JMATYP(*),COORD(*)
```

```
12  C
13        DIMENSION ztmpl(350,4), ztmpe(350,4)
14        COMMON /ztl/ ztmpl, ztmpe
15  C
16        CALL GETVRM('TEMP',ARRAY,JARRAY,FLGRAY,JRCD,JMAC,JMATYP,MATLAYO,
17       1                LACCFLA)
18  C
19        if (CMNAME(1:4) .eq. 'MATE') then
20          tmpl = ztmpl(NOEL,NPT)
21          if ((KSTEP .eq. 1) .and. (KINC .eq. 0)) tmpl = 0.3
22          tmpe = ARRAY(1)
23  C
24          STATEV(1) = cne(tmpe,tmpl)
25          STATEV(2) = dcnedt(tmpe,tmpl)
26          STATEV(3) = sphte(tmpe)
27  C
28          ztmpe(NOEL,NPT) = tmpe
29  C
30        else
31  C
32          nel = NOEL - 600
33  C
34          tmpe = ztmpe(nel,NPT)
35          if ((KSTEP .eq. 1) .and. (KINC .eq. 0)) tmpe = 0.3
36          tmpl = ARRAY(1)
37  C
38          STATEV(1) = 0.0
39          STATEV(2) = 0.0
40          STATEV(3) = sphtl(tmpl)
41  C
42          ztmpl(nel,NPT) = tmpl
43  C
44        endif
45  C
46        call cplf(gg,dgdtmp,tmpe,tmpl)
47        STATEV(4) =  gg * (tmpe - tmpl)
48  C
49        call tauc(tu,dtu,tmpe,tmpl)
50        STATEV(5) = tu
51        STATEV(6) = dtu
52  C
53        RETURN
54        END
```

The user subroutine UMESHMOTION calculates domain deformation due to ablation using Eq. (2.19). The results are then converted from normalized coordinates

to actual coordinates, Fig. 2.3, in lines 37 $\sim$ 40, and the value passed to ABAQUS, lines 46 and 47:

```
1         SUBROUTINE UMESHMOTION(UREF,ULOCAL,NODE,NNDOF,
2        * LNODETYPE,ALOCAL,NDIM,TIME,DTIME,PNEWDT,
3        * KSTEP,KINC,KMESHSWEEP,JMATYP,JGVBLOCK,LSMOOTH)
4   C
5         INCLUDE 'aba_param.inc'
6   C
7         parameter (tcrit = 6.903)
8   C
9         DIMENSION ULOCAL(NDIM), JELEMLIST(100)
10        DIMENSION ALOCAL(NDIM,*),TIME(2)
11        DIMENSION JMATYP(*),JGVBLOCK(*)
12  C
13        dimension array(10)
14  C
15        if (NODE .lt. 600) then
16          ndt1 = NODE + 600
17          ndx1 = NODE
18        else
19          ndt1 = NODE
20          ndx1 = NODE
21        end if
22  C
23        ndt2 = ndt1 + 1
24        ndx2 = ndx1 + 1
25        ltrn = 0
26  C
27        call GETVRN(ndt1,'NT',array,jrcd,JGVBLOCK,ltrn)
28        tmp1 = array(1)
29        call GETVRN(ndx1,'COORD',array,jrcd,JGVBLOCK,ltrn)
30        crd1 = array(1)
31        call GETVRN(ndt2,'NT',array,jrcd,JGVBLOCK,ltrn)
32        tmp2 = array(1)
33        call GETVRN(ndx2,'COORD',array,jrcd,JGVBLOCK,ltrn)
34        crd2 = array(1)
35  C
36        if (tmp1 .gt. tcrit) then
37          xxx = (tmp1 + tmp2 - 2 * tcrit)/(tmp1 - tmp2)
38          xx1 = (xxx + 1) * (crd2 - crd1) / 2
39          x2 = 0.0
40          x1 = max(0.0, xx1)
41        else
42          x1 = 0.0
43          x2 = 0.0
```

```
44          end if
45  C
46          ULOCAL(1) = x1 * ALOCAL(1,1) + x2 * ALOCAL(2,1)
47          ULOCAL(2) = x1 * ALOCAL(1,2) + x2 * ALOCAL(2,2)
48  C
49          LSMOOTH = 1
50  C
51          RETURN
52          END
```

Bibliography

Bibliography

Kaganov, M., Lifshitz, I. and Tanatarov, L., 1957, "Relaxation between electrons and the crystalline lattice," Sov Phys-JETP, **4**, pp. 173–178

Gregg, D. and Thomas, S., 1966, "Momentum transfer produced by focused laser giant pulses," J Appl Phys, **37**(7), pp. 2787 – 2788

Anderholm, N., 1970, "Laser-generated stress waves," Appl Phys Lett, **16**(3), pp. 113 – 115

Touloukian, Y.S. and DeWitt, D.P. (eds.), 1970, *Thermophisical Properties of Matter*, IFI/PLENUM, New York, New York

Dabby, F. and Paek, U., 1972, "High-intensity laser-induced vaporization and explosion of solid material," IEEE J Quantum Electron, **QE 8**, pp. 106–111

Fairand, B., Wilcox, B., Gallagher, W. and Williams, D., 1972, "Laser shock-induced microstructural and mechanical property changes in 7075 aluminum," J Appl Phys, **43**(9), pp. 3893 – 3895

Anisimov, S.I., Kapeliovich, B.L. and Perel'man, T.L., 1974, "Electron emission from metal surfaces exposed to ultrashort laser pulses," Sov Phys-JETP, **39**(2), pp. 375 – 377

Ashcroft, N. and Mermin, N., 1976, *Solid state physics*, Thomson learning Inc., USA

Strickland, D. and Mourou, G., 1985, "Compression of amplified chirped optical pulses," Opt Commun, **56**, pp. 219–221

Siegman, A.E., 1986, *LASERS*, University Science Books, Sausalito, Calinfornia

Allen, P., 1987, "Theory of thermal relaxation of electrons in metals," Phys Rev Lett, **59**, pp. 1460–1463

Elsayedali, H., Norris, T., Pessot, M. and Mourou, G., 1987, "Time-resolved observation of electron-phonon relaxation in copper," Phys Rev Lett, **58**, pp. 1212–1215

Korb, L.J. and Olson, D.L. (eds.), 1987, *ASM Handbook*, vol. 13, ASM International, Materials Park, Ohio

Sherman, N., Brunel, F., Corkum, P. and Hegmann, F., 1989, "Transient-response of metals to ultrashort pulse excitation," Opt Eng, **28**, pp. 1114–1121

Banaś, G., Elsayed-Ali, H., Lawrence, F.V., J. and Rigsbee, J., 1990, "Laser shock-induced mechanical and microstructural modification of welded maraging steel," J Appl Phys, **67**(5), pp. 2380 – 2384

Brorson, S., Kazeroonian, A., Moodera, J., Face, D., Cheng, T., Ippen, E., Dresselhaus, M. and Dresselhaus, G., 1990, "Femtosecond room-temperature measurement of the electron-phonon coupling constant λ in metallic superconductors," Phys Rev Lett, **64**, pp. 2172–2175

Forget, P., Strudel, J., Jeandin, M., Lu, J. and Castex, L., 1990, "Laser shock surface treatment of Ni-based superalloys," Mater Manuf Process, **5**(4), pp. 501 – 528

Montgomery, D.C., 1991, *Design and Analysis of Experiments*, 3rd ed., John Wiley & Sons, Inc., Canada

Fann, W., Storz, R., Tom, H. and Bokor, J., 1992, "Direct measurement of nonequilibrium electron-energy distributions in subpicosecond laser-heated gold films," Phys Rev Lett, **68**(18), pp. 2834 – 2837

Mills, A.F., 1992, *Heat Transfer*, Irwin Inc., Boston, Massachusetts

Qiu, T. and Tien, C., 1993, "Heat-transfer mechanisms during short-pulse laser-heating of metals," Trans ASME, J Heat Transf, **115**, pp. 835–841

Hays-Stang, K.J. and Haji-Sheikh, A., 1994, "An analytical solution for heat transfer in thin films," *ASME Heat Transfer Div. Publ. HTD*, vol. 293, Chicago, IL, USA, pp. 1 – 7

Wang, X., Riffe, D., Lee, Y. and Downer, M., 1994, "Time-resolved electron-temperature measurement in a highly excited gold target using femtosecond thermionic emission," Phys Rev B, Condens Matter, **50**, pp. 8016–8019

Preuss, S., Demchuk, A. and Stuke, M., 1995, "Sub-picosecond UV laser ablation of metals," Appl Phys A, Mater Sci Process, **61**(1), pp. 33 –37

Pronko, P., Dutta, S., Du, D. and Singh, R., 1995, "Thermophysical effects in laser processing of materials with picosecond and femtosecond pulses," J Appl Phys, **78**, pp. 6233–6240

Chichkov, B., Momma, C., Nolte, S., vonAlvensleben, F. and Tünnermann, A., 1996, "Femtosecond, picosecond and nanosecond laser ablation of solids," Appl Phys A, Mater Sci Process, **63**, pp. 109–115

Hüttner, B. and Rohr, G., 1996, "On the theory of ps and sub-ps laser pulse interac-

tion with metals .1. surface temperature," Appl Surf Sci, **103**, pp. 269–274

Kelly, R. and Miotello, A., 1996, "Comments on explosive mechanisms of laser sputtering," Appl Surf Sci, **96-8**, pp. 205–215

Peyre, P., Fabbro, R., Merrien, P. and Lieurade, H., 1996, "Laser shock processing of aluminium alloys. application to high cycle fatigue behaviour," Mater Sci Eng A, **A210**(1-2), pp. 102 – 113

Stuart, B., Feit, M., Herman, S., Rubenchik, A., Shore, B. and Perry, M., 1996, "Optical ablation by high-power short-pulse lasers," J Opt Soc Am B, Opt Phys, **13**, pp. 459–468

Anisimov, S. and Rethfeld, B., 1997, "On the theory of ultrashort laser pulse interaction with a metal," *Proc. SPIE*, vol. 3093, pp. 192 – 203

Liu, X., Du, D. and Mourou, G., 1997, "Laser ablation and micromachining with ultrashort laser pulses," IEEE J Quantum Electron, **33**, pp. 1706–1716

Momma, C., Nolte, S., Chichkov, B., vonAlvensleben, F. and Tunnermann, A., 1997, "Precise laser ablation with ultrashort pulses," Appl Surf Sci, **109/110**, pp. 15–19

Nolte, S., Momma, C., Jacobs, H., Tunnermann, A., Chichkov, B., Wellegehausen, B. and Welling, H., 1997, "Ablation of metals by ultrashort laser pulses," J Opt Soc Am B, **14**, pp. 2716–2722

Tzou, D., 1997, *Macro- to Microscale Heat Transfer*, Taylor & Francis, Washington, DC

Craciun, V., Craciun, D., Bunescu, M., Boulmer-Leborgne, C. and Hermann, J., 1998, "Subsurface boiling during pulsed laser ablation of Ge," Phys Rev B, Condens Matter, **58**, pp. 6787–6790

Fabbro, R., Peyre, P., Berthe, L. and Scherpereel, X., 1998, "Physics and applications of laser-shock processing," J Laser Appl, **10**(6), pp. 265 – 279

Hong, Z. and Chengye, Y., 1998, "Laser shock processing of 2024-T62 aluminum alloy," Mater Sci Eng A, **257**(2), pp. 322 – 327

Smith, A. and Norris, M., 1998, "Numerical solution for the diffusion of high intensity, ultrashort laser pulses within metal films," *Proceedings of 11th International Heat Transfer Conference*, vol. 5, Kyongju, Korea, pp. 241–246

Braisted, W. and Brockman, R., 1999, "Finite element simulation of laser shock peening," Int J Fatigue, **21**(7), pp. 719 – 724

Chu, J., Rigsbee, J., Banaś, G. and Elsayed-Ali, H., 1999, "Laser-shock processing

effects on surface microstructure and mechanical properties of low carbon steel," Mater Sci Eng A, **A260**(1-2), pp. 260 – 268

Furusawa, K., Takahashi, K., Kumagai, H., Midorikawa, K. and Obara, M., 1999, "Ablation characteristics of Au, Ag, and Cu metals using a femtosecond Ti:sapphire laser," Appl Phys A, Mater Sci Process, **69** [**Suppl.**], pp. S359–S366

Hostetler, J., Smith, A., Czajkowsky, D. and Norris, P., 1999, "Measurement of the electron-phonon coupling factor dependence on film thickness and grain size in Au, Cr, and Al," Appl Opt, **38**, pp. 3614–3620

Smith, A., Hostetler, J. and Norris, P., 1999, "Nonequilibrium heating in metal films: An analytical and numerical analysis," Numer Heat Transf A, Appl, **35**, pp. 859–873

Wellershoff, S., Hohlfeld, J., Gudde, J. and Matthias, E., 1999, "The role of electron-phonon coupling in femtosecond laser damage of metals," Appl Phys A, Mater Sci Process, **69**, pp. S99–S107

Zhu, X., Naumov, A., Villeneuve, D. and Corkum, P., 1999, "Influence of laser parameters and material properties on micro drilling with femtosecond laser pulses," Appl Phys A, Mater Sci Process, **69** [**Suppl.**], pp. S367–S371

Banks, P.S., Feit, M.D., Perry, M.D., Stuart, B.C., Rubenchik, A.M. and Komashko, A.M., 2000, "Femtosecond laser materials processing," *Proc. SPIE*, vol. 3934, pp. 14 –21

Hammersley, G., Hackel, L. and Harris, F., 2000, "Surface prestressing to improve fatigue strength of components by laser shot peening," Opt Lasers Eng, **34**(4-6), pp. 327 – 337

Hohlfeld, J., Wellershoff, S., Gudde, J., Conrad, U., Jahnke, V. and Matthias, E., 2000, "Electron and lattice dynamics following optical excitation of metals," Chem Phys, **251**, pp. 237–258

Kaspar, J., Luft, A. and Skrotzki, W., 2000, "Deformation modes and structure evolution in laser-shock-loaded molybdenum single crystals of high purity," Cryst Res Technol, **35**(4), pp. 437 – 448

Peyre, P., Scherpereel, X., Berthe, L., Carboni, C., Fabbro, R., Beranger, G. and Lemaitre, C., 2000, "Surface modifications induced in 316L steel by laser peening and shot-peening. influence on pitting corrosion resistance," Mater Sci Eng A, **A280**(2), pp. 294 – 302

Chen, J. and Beraun, J., 2001, "Numerical study of ultrashort laser pulse interactions with metal films," Numer Heat Transf A, Appl, **40**, pp. 1–20

Jou, D., Casas-Vázquez, J. and Lebon, G., 2001, *Extended Irreversible Thermodynamics*, Springer-Verlag, Germany

Kalpakjian, S. and Schmid, S., 2001, *Manufacturing Processes for Engineering Materials*, 4th ed., Pearson Education, Upper Saddle River, New Jersey

Kaspar, J. and Luft, A., 2001, "Microstructure formed in body centred cubic metals by laser shock processing," Surf Eng, **17**(5), pp. 379 – 383

Wild, M., Gillner, A. and Poprawe, R., 2001, "Locally selective bonding of silicon and glass with laser," Sens Actuators A Phys, **93**(1), pp. 63 – 69

Brockmann, R., Honekamp, M., Dickmann, K., Meier, S., Letsch, H. and Matthes, K.J., 2002, "Modern welding processes for microsystems engineering and electronics taking particular account of the laser," Weld Res Abroad, **48**(4), pp. 27 – 32

Chen, J., Latham, W. and Beraun, J., 2002, "Axisymmetric modeling of femtosecond-pulse laser heating on metal films," Numer Heat Transf B, Fundam, **42**, pp. 1–17

Dickinson, J., 2002, "Physical and chemical aspects of laser-materials interactions relevant to laser processing," *Proc. SPIE*, vol. 4637, pp. 453 – 464

Du, J., Longobardi, J., Latham, W. and Kar, A., 2002, "Laser marginal lap microwelding for ultrathin sheet metal," J Laser Appl, **14**(1), pp. 4 – 8

Dumitru, G., Romano, V., Weber, H., Sentis, M. and Marine, W., 2002, "Femtosecond ablation of ultrahard materials," Appl Phys A, Mater Sci Process, **74**, pp. 729–739

Hecht, E., 2002, *Optics*, 4th ed., Addison Wesley, San Francisco, California

Kramer, T., Olowinsky, A. and Durand, F., 2002, "Shadow-a new welding technique," *Proc. SPIE*, vol. 4637, pp. 545 – 554

Montross, C., Wei, T., Ye, L., Clark, G. and Mai, Y.W., 2002, "Laser shock processing and its effects on microstructure and properties of metal alloys: a review," Int J Fatigue, **24**(10), pp. 1021 – 1036

Schmidt, V., Husinsky, W. and Betz, G., 2002, "Ultrashort laser ablation of metals: pump-probe experiments, the role of ballistic electrons and the two-temperature model," Appl Surf Sci, **197**, pp. 145–155

See, D., Dulaney, J., Clauer, A. and Tenaglia, R., 2002, "The air force manufacturing technology laser peening initiative," Surf Eng, **18**(1), pp. 32 – 36

Abe, N., Funada, Y. and Ishide, M., 2003, "Micro-welding of thin foil with direct diode laser," *Proc. SPIE*, vol. 5063, pp. 287 – 291

Chen, J. and Beraun, J., 2003, "Modelling of ultrashort laser ablation of gold films in vacuum," J Opt A:Pure Appl Opt, **5**, pp. 168–173

Deshayes, Y., Bechou, L., Deletage, J., Verdier, F., Danto, Y., Laffitte, D. and Goudard, J., 2003, "Three-dimensional fem simulations of thermomechanical stresses in 1.55 μm laser modules," Microelectron Reliab, **43**(7), pp. 1125 – 1136

Dijken, D., Hoving, W. and De Hosson, J., 2003, "Laser penetration spike welding: a microlaser welding technique enabling novel product designs and constructions," J Laser Appl, **15**(1), pp. 11 – 18

Griffith, M.L., Ensz, M.T. and Reckaway, D.E., 2003, "Femtosecond laser machining of steel," *Proc. SPIE*, vol. 4977, pp. 118 –122

Park, S., Ohmura, E. and Miyamoto, I., 2003, "Micro welding of ultra thin metal foil using yb-fiber laser," *Proc. SPIE*, vol. 4830, pp. 52 – 56

Peyre, P., Sollier, A., Chaieb, I., Berthe, L., Bartnicki, E., Braham, C. and Fabbro, R., 2003, "FEM simulation of residual stresses induced by laser peening," Eur Phys J AP, **23**, pp. 83–88

Semak, V., Knorovsky, G. and MacCallum, D., 2003, "On the possibility of microwelding with laser beams," J Phys D:Appl Phys, **36**(17), pp. 2170 – 2174

Sonntag, R.E., Borgnakke, C. and Wylen, G.J.V., 2003, *Fundamentals of Thermodynamics*, 6th ed., John Wiley & Sons, Inc., Hoboken, New Jersey

Triantafyllidis, D., Schmidt, M. and Li, L., 2003, "Comparison of high power diode laser and Nd:YAG laser microwelding of k-type thermocouples," J Mater Process Technol, **138**, pp. 102–108

Yilbas, B., Shuja, S., Arif, A. and Gondal, M., 2003, "Laser-shock processing of steel," J Mater Process Technol, **135**(1), pp. 6 – 17

Zhang, X. and Xu, X., 2003, "High precision microscale bending by pulsed and cw lasers," Trans ASME, J Manuf Sci Eng, **125**, pp. 512–518

Bulgakova, N., Bulgakov, A. and Babich, L., 2004, "Energy balance of pulsed laser ablation: thermal model revised," Appl Phys A, Mater Sci Process, **79**, pp. 1323–1326

Duley, W., 2004, "Physics, chemistry, and laser microprocessing," J Laser Appl, **16**(1), pp. 52 – 54

Isamu, M., Takeshi, K., Park, S., Hiroaki, U., Koji, W. and Toshihiko, O., 2004, "Applications of single-mode fiber-lasers to novel microwelding," *Proc. SPIE*, vol. 5662, pp. 507 – 514

Rubio-González, C., Ocaña, J., Gomez-Rosas, G., Molpeceres, C., Paredes, M., Banderas, A., Porro, J. and Morales, M., 2004, "Effect of laser shock processing on fatigue crack growth and fracture toughness of 6061-T6 aluminum alloy," Mater Sci Eng A, **A386**(1-2), pp. 291 – 295

Tan, Y., Wu, G., Yang, J. and Pan, T., 2004, "Laser shock peening on fatigue crack growth behaviour of aluminium alloy," Fatigue Fract Eng Mater Struct, **27**, pp. 649–656

Vander Voort, G.F. (ed.), 2004, *ASM Handbook*, vol. 9, ASM International, Materials Park, Ohio

Yakimets, I., Richard, C., Beranger, G. and Perye, P., 2004, "Laser peening processing effect on mechanical and tribological properties of rolling steel 100Cr6," Wear, **256**(3-4), pp. 311 – 320

Zhang, W., Yao, Y. and Noyan, I., 2004, "Microscale laser shock peening of thin films, part 2: High spatial resolution material characterization," Trans ASME, J Manuf Sci Eng, **126**(1), pp. 18 – 24

Aldajah, S., Ajayi, O., Fenske, G. and Xu, Z., 2005, "Effect of laser surface modifications tribological performance of 1080 carbon steel," Trans ASME, J Tribol, **127**(3), pp. 596 – 604

Borrisutthekul, R., Miyashita, Y. and Mutoh, Y., 2005, "Dissimilar material laser welding between magnesium alloy az31b and aluminum alloy a5052-o," Sci Technol Adv Mater, **6**, pp. 199–204

Chen, J., Latham, W. and Beraun, J., 2005, "The role of electron-phonon coupling in ultrafast laser heating," J Laser Appl, **17**, pp. 63–68

Fabbro, R., Slimani, S., Coste, F. and Briand, F., 2005, "Study of keyhole behaviour for full penetration Nd-Yag CW laser welding," J Phys D:Appl Phys, **38**, pp. 1881–1887

Lin, Y., Eichele, C. and Shi, F., 2005, "Effect of welding sequence on welding-induced-alignment-distortion in packaging of butterfly laser diode modules: Simulation and experiment," J Lightwave Technol, **23**, pp. 615–623

Vogel, A., Noack, J., Huttman, G. and Paltauf, G., 2005, "Mechanisms of femtosecond laser nanosurgery of cells and tissues," Appl Phys B, Lasers Opt, **B81**(8), pp. 1015 – 1047

ABAQUS Inc., 2006, *ABAQUS Manual*, Providence, Rhode Island, version 6.6 ed.

Cao, X., Jahazi, M., Immarigeon, J. and Wallace, W., 2006, "A review of laser welding techniques for magnesium alloys," J Mater Process Technol, **171**, pp. 188–204

Dehoux, T., Perton, M., Chigarev, N., Rossignol, C., Rampnoux, J.M. and Audoin, B., 2006, "Effect of laser pulse duration in picosecond ultrasonics," J Appl Phys, **100**(6), pp. 064318–1 – 064318–8

Farrahi, G. and Ghadbeigi, H., 2006, "An investigation into the effect of various surface treatments on fatigue life of a tool steel," J Mater Process Technol, **174**(1-3), pp. 318 – 324

Lin, Z. and Zhigilei, L.V., 2006, "Thermal excitation of d band electrons in au: Implications for laser-induced phase transformations," *Proc. SPIE*, vol. 6261, pp. 62610U–1 – 62610U–14

Mys, I. and Schmidt, M., 2006, "Laser micro welding of copper and aluminum," *Proc. SPIE*, vol. 6107, pp. 610703–1 – 610703–6

Tamaki, T., Watanabe, W. and Itoh, K., 2006, "Laser micro-welding of transparent materials by a localized heat accumulation effect using a femtosecond fiber laser at 1558 nm," Opt Express, **14**, pp. 10460–10468

Zhang, H. and Senkara, J., 2006, *Resistance Welding*, Taylor & Francis, Boca Raton, Florida

Richter, K., Behr, W. and Reisgen, U., 2007, "Low heat welding of titanium materials with a pulsed Nd:YAG laser," Materwis Werkstofftech, **38**, pp. 51–56

Sierra, G., Peyre, P., Deschaux-Beaume, F., Stuart, D. and Fras, G., 2007, "Steel to aluminium key-hole laser welding," Mater Sci Eng A, **447**(1-2), pp. 197 – 208